Controlled Growth and Quantum Emitter Integration in Hexagonal Boron Nitride

A thesis submitted for the degree of Doctor of Philosophy at

University of Technology Sydney

School of Mathematical and Physical Sciences

Faculty of Science

By

RITIKA

Supervisors

Prof. Igor AHARONOVICH

Prof. Milos TOTH

November 2025

CERTIFICATE OF ORIGINAL AUTHORSHIP

I, *Ritika*, declare that this thesis is submitted in fulfilment of the requirements for the award of *Doctor of Philosophy*, in the *School of Mathematical and Physical Sciences* at the University of Technology Sydney.

This thesis is wholly my own work unless otherwise referenced or acknowledged. In addition, I certify that all information sources and literature used are indicated in the thesis.

This document has not been submitted for qualifications at any other academic institution.

This research was supported by an Australian Government Research Training Program (RTP) Scholarship doi.org/10.82133/C42F-K220.

Signature: Production Note:
Signature removed prior to publication.

Date: 20/10/2025

Acknowledgements

I would like to express my deepest gratitude to my supervisors, Professor Igor Aharonovich and Professor Milos Toth, for their guidance and support throughout the entirety of this project and my candidature. Their scientific insight, high expectations, and commitment to research excellence have shaped the way I think about problems, design experiments, and interpret results. I have learned not only scientific skills from them, but also the importance of clarity, precision, and integrity in research. Their influence will continue to guide me long after the submission of this thesis.

I am especially grateful to my mentor, Dr Noah Mendelson. Noah, your support has been fundamental to my progression as a researcher. You were the person I turned to when experiments failed, when results did not make sense, and when I doubted my own ability. Thank you for your patience, for the time you invested in helping me problem-solve, and for your willingness to listen and guide without judgement. Your faith in me, made the difference between giving up and trying again. I could not imagine completing this journey without your mentorship, encouragement, and kindness.

I would also like to acknowledge the research environment and community within the School of Mathematical and Physical Sciences at the University of Technology Sydney. I have been fortunate to work in a group of individuals who are not only talented scientists, but also generous, collaborative, and supportive people. In particular, I extend my sincere thanks to Helen, Minh, and Madeline, with whom I shared much more than a laboratory or office space. Thank you for your constant support and belief in me, for the emotional

encouragement during difficult periods, and for reminding me that setbacks and challenges are part of the journey rather than signs of failure. Your presence helped me endure the days when experiments refused to cooperate and helped me celebrate the days when they finally did. I am grateful to each of you for the friendship, strength, and understanding you offered, especially when I found myself overwhelmed.

I gratefully acknowledge the support of the ARC Centre of Excellence for Transformative Meta-Optical Systems (TMOS). The wider TMOS research community has been an invaluable source of scientific exchange and intellectual growth. Conferences, workshops, and internal discussions broadened my perspective, challenged me to refine my ideas, and connected me to researchers who are working to advance the field that inspired this thesis.

I would also like to thank the Sydney Quantum Academy (SQA) community for their commitment to an excellent student experience. Serving as an SQA student representative gave me a meaningful way to contribute to our academic environment, and I am grateful to staff and fellow representatives for their collaboration and trust.

I would like to extend my heartfelt thanks to my family. Mom and Dad, your unwavering belief in me has been the foundation upon which every achievement in my life has been built. You encouraged my curiosity from a young age and taught me to persist, even when progress was slow and the outcome uncertain. Your support, patience and love carried me through many moments of doubt and exhaustion. To my sister, Bhumi and my brother, Nikhil, thank you for your understanding, humour, and reminders to step back and breathe. Your emotional support throughout the hardest periods of my PhD meant more than I can express, you helped me stay grounded when the work felt overwhelming.

To Abhi, thank you for standing beside me through every phase of this journey. You have seen the stress, frustration, late nights, setbacks, and moments when I questioned whether I would finish. Thank you for your patience during those times, for your reassurance when I was uncertain, and for reminding me of my own strength when I couldn't see it. Your belief in me did not waver, even when mine did. You helped me continue, one day at a time, and for that I am deeply grateful.

The process of completing a PhD is not only an academic challenge but an emotional endurance, one that is rarely done alone. I am fortunate to have been surrounded by people who supported me with kindness, understanding, honesty, and compassion. To everyone who contributed a conversation, encouragement, or moment of shared perspective- thank you! Each gesture helped me continue.

This thesis is, in many ways, a reflection not only of my own efforts, but of the collective support, patience, and belief of those around me. To all of you, I offer my sincere thanks.

Contents

List of Publications

1. **Ritika, R.**[*], Mendelson, N.[*], Kianinia, M., Scott, J., Kim, S., Fröch, J.E., Gazzana, C., Westerhausen, M., Xiao, L., Mohajerani, S.S. and Strauf, S., 2022. Coupling spin defects in a layered material to nanoscale plasmonic cavities. *Advanced Materials*, *34*(1), p.2106046.

2. Tang, T.W. [*], **Ritika, R.** [*], Tamtaji, M., Liu, H., Hu, Y., Liu, Z., Galligan, P.R., Xu, M., Shen, J., Wang, J. and You, J., 2025. Structured-Defect Engineering of Hexagonal Boron Nitride for Identified Visible Single-Photon Emitters. ACS nano, 19(9), pp.8509-8519.

3. Li, C., Mendelson, N., **Ritika, R.**, Chen, Y., Xu, Z.Q., Toth, M. and Aharonovich, I., 2021. Scalable and deterministic fabrication of quantum emitter arrays from hexagonal boron nitride. *Nano Letters*, *21*(8), pp.3626-3632.

4. Mendelson, N., Morales-Inostroza, L., Li, C., **Ritika, R.**, Nguyen, M.A.P., Loyola-Echeverria, J., Kim, S., Götzinger, S., Toth, M. and Aharonovich, I., 2021. Grain dependent growth of bright quantum emitters in hexagonal boron nitride. *Advanced Optical Materials*, *9*(1), p.2001271.

5. Glushkov, E., Mendelson, N., Chernev, A., **Ritika, R**., Lihter, M., Zamani, R.R., Comtet, J., Navikas, V., Aharonovich, I. and Radenovic, A., 2021. Direct growth of hexagonal boron nitride on photonic chips for high-throughput characterization. *Acs Photonics*, *8*(7), pp.2033-2040.

Paper Information

Paper Title:

Structured-Defect Engineering of Hexagonal Boron Nitride for Identified Visible Single-Photon Emitters

Authors (in order of appearance):
Tsz Wing Tang, Ritika Ritika, Mohsen Tamtaji, Hongwei Liu, Yunxia Hu, Zhenjing Liu, Patrick Ryan Galligan, Mengyang Xu, Jinghan Shen, Jun Wang, Jiawen You, Yuyin Li, GuanHua Chen, Igor Aharonovich, Zhengtang Luo

Publication Outlet: ACS nano

Publication Status: Published

Contribution Statement

I confirm that the description below of each author's contribution to this paper is accurate, and that the graduate research student's contribution is correctly represented.

Author	Contribution(s) (Credit)	Signature
Tsz Wing Tang	Conceptualisation, methodology, investigation, formal analysis, validation, visualisation, writing - original draft, writing -review and editing	Production Note: Signature removed prior to publication.
Ritika Ritika	Methodology, investigation, formal analysis, validation, writing - original draft, writing - review and editing	Production Note: Signature removed prior to publication.
Mohsen Tamtaji	Simulation, investigation, formal analysis, validation, writing - original draft	Production Note: Signature removed prior to publication.
Hongwei Liu	Methodology, investigation	
Yunxia Hu	Methodology, writing - review and editing,	Production Note: Signature removed prior to publication.
Zhenjing Liu	Formal analysis, writing - review and editing	
Patrick Ryan Galligan	Methodology, writing - review and editing	Production Note: Signature removed prior to publication.
Mengyang Xu	Writing - review and editing	Production Note: Signature removed prior to publication.
Jinghan Shen	Writing - review and editing	Production Note: Signature removed prior to publication.
Jun Wang	Writing - review and editing	Production Note: Signature removed prior to publication.
Jiawen You	Writing - review and editing	
Yuyin Li	Writing - review and editing	
GuanHua Chen	methodology, investigation, formal analysis, validation, writing -review and editing, supervision	
Igor Aharonovich	Methodology, investigation, formal analysis, validation, visualisation, writing - review and editing, supervision	Production Note: Signature removed prior to publication.
Zhengtang Luo	Conceptualisation, methodology, investigation, formal analysis, validation, visualisation, writing - original draft, writing -review and editing, Supervision	Production Note: Signature removed prior to publication.

Paper Information

Paper Title:

Coupling spin defects in a layered material to nanoscale plasmonic cavities

Authors (in order of appearance):

Noah Mendelson, Ritika Ritika, Mehran Kianinia, John Scott, Sejeong Kim, Johannes E Fröch, Camilla Gazzana, Mika Westerhausen, Licheng Xiao, Seyed Sepehr Mohajerani, Stefan Strauf, Milos Toth, Igor Aharonovich, Zai-Quan Xu

Publication Outlet: Advanced Materials

Publication Status: Published

Contribution Statement

I confirm that the description below of each author's contribution to this paper is accurate, and that the graduate research student's contribution is correctly represented.

Author	Contribution(s) (CRediT)	Signature
Noah Mendelson	Conceptualisation, methodology, investigation, formal analysis, validation, visualisation, writing - original draft, writing - review and editing	
Ritika Ritika	Conceptualisation, methodology, investigation, formal analysis, validation, writing - original draft, writing - review and editing	Production Note: Signature removed prior to publication.
Mehran Kianinia	Methodology, software, investigation, formal analysis, validation, writing - original draft	Production Note: Signature removed prior to publication.
John Scott	Methodology, software, investigation, formal analysis, validation, writing - original draft	Production Note: Signature removed prior to publication.
Sejeong Kim	Methodology, Simulation, writing - review and editing, supervision	
Johannes E Fröch,	Methodology, writing- original draft, writing - review and editing, supervision	Production Note: Signature removed prior to publication.
Camilla Gazzana	Writing - review and editing, supervision	Production Note: Signature removed prior to publication.
Mika Westerhausen	Writing - review and editing, supervision	Production Note: Signature removed prior to publication.
Licheng Xiao	Conceptualisation, methodology, supervision, writing - review and editing	
Seyed Sepehr Mohajerani	Conceptualisation, methodology, supervision, writing - review and editing	
Stefan Strauf	Conceptualisation, methodology, supervision, writing - review and editing, funding acquisition	Production Note: Signature removed prior to publication.
Milos Toth	Conceptualisation, methodology, supervision, writing - review and editing, funding acquisition	Production Note: Signature removed prior to publication.
Igor Aharonovich	Conceptualisation, methodology, supervision, writing - review and editing, funding acquisition	Production Note: Signature removed prior to publication.
Zai-Quan Xu	Conceptualisation, methodology, investigation, formal analysis, validation, visualisation, writing - original draft, writing - review and editing	Production Note: Signature removed prior to publication.

List of Figures

Abbreviation

hBN	Hexagonal Boron Nitride
LPCVD	Low Pressure Chemical Vapor Deposition
SPE	Single Photon Emitter
QKD	Quantum Key Distribution
PL	Photoluminescence
APD	Avalanche Photodiodes
HBT	Hanbury Brown-Twiss
TCSPC	Time-Correlated Single Photon Counting

Abstract

Quantum technologies face significant challenges despite years of research and development. To leverage the exceptional capabilities of these technologies, that enable faster computing and encrypted communication, a reliable single photon source is crucial. As discussed later in this thesis, defects in solid-state materials are among the most promising single photon sources. From colour centers in diamond to quantum dots, extensive studies have been conducted over the past decade to discover and utilize these emissions. Among the vast array of available sources, 2D materials are considered most favourable for quantum applications as they offer easy integration with photonic chips, localized and controlled creation of defects, high efficiency and spin-active properties.

Diamond and silicon carbide have been intensely studied due to their bright and photostable emission. However, efficient integration remains a critical challenge. In contrast, atomically thin (2D) materials such as hexagonal boron nitride (hBN) lack dangling bonds, allowing for efficient integration with nanophotonic devices. hBN defects have demonstrated high efficiency in light-matter interactions and allow stacking into van der Waals heterostructures. Specifically, hBN can host ultra-bright single photon emission arising from point defects in the lattice. Despite these advantages, ongoing research is needed to fully understand and optimize the material, as it struggles with emitter blinking and stability issues that needs to be addressed for practical quantum applications.

Abstract

In this thesis, I develop and demonstrate scalable approaches for creating and controlling quantum emitters in hexagonal boron nitride. I optimized low-pressure chemical vapor deposition (LPCVD) growth to produce uniform, crystalline hBN films capable of hosting single-photon emitters. I investigated homoepitaxial growth to understand how lattice coherence influences defect incorporation and emission quality. Through structured-defect engineering, I activated bright, stable visible emitters and systematically correlated their optical properties with synthesis conditions. I performed comprehensive optical characterization, including wide-field and confocal photoluminescence and lifetime analyses. Finally, I explored plasmonic coupling of spin-active boron vacancy defects to enhance light–matter interactions and advance integration with quantum photonic devices.

1

Introduction

1.1 Motivation

Over the past century, science and technology have rapidly advanced due to major breakthroughs in information processing and transmission. These innovations have driven much of the progress in modern society. However, the accelerating demands for security and computational power are exceeding the capabilities of classical technologies. Modern fibre optics communication is effective yet vulnerable to eavesdropping and attacks, as both the encryption methods and the light signals used are susceptible to interception. As Moore's law approaches its limits, the continued reduction in transistor size and the evolution of traditional computing architectures are slowing down. This has led to the emergence of a demand for alternative approaches to computation and information security.

Quantum communication and computing represent the next frontier in addressing these challenges, offering unprecedented possibilities in secure data transmission and

complex problem-solving through quantum supremacy. Photonic quantum communication relies on light-based quantum states, it's a particularly promising field, as light can serve as both the medium of information transport and computation. Significant progress has already been made by leading researchers in this field, including breakthroughs in photonic quantum cryptography. Additionally, the demonstration of quantum computational advantage has further highlighted the progress made in this field.

A critical catalyst of these technologies is the development of single-photon source (SPS) devices that emit individual photons on demand. SPS are essential for quantum cryptography, quantum key distribution (QKD) and quantum computing, they ensure integrity and reliability of quantum information systems. One of the most promising materials for this purpose is hexagonal boron nitride (hBN), which hosts optically active defects that can act as room-temperature single-photon emitters. Unlike other materials that require cryogenic environments to function, hBN offers a robust platform for quantum light generation under ambient conditions.

The versatility of hexagonal boron nitride (hBN) as a two-dimensional material offers far beyond its application in SPS systems. With its wide bandgap, robust chemical stability, and seamless compatibility with other 2D materials, it stands out as a strong candidate for integration into quantum technologies. Despite its traditional role as a supporting layer in 2D heterostructures, recent discoveries have shown that defects within hBN can produce stable, bright single-photon emission, positioning it as a leading candidate for next-generation quantum photonic technologies.

In this thesis, I will explore the synthesis, optical properties, and engineering of hBN to optimize its performance as a quantum light source. Particular attention will be given to

the growth of high-quality hBN films via chemical vapor deposition (CVD) and the engineering of defect structures to enhance single-photon emission. Additionally, advanced microscopy techniques will be employed to study the properties of hBN and its interaction with plasmonic systems, with the goal of developing scalable, reliable quantum emitters for photonic quantum technologies.

1.2 Thesis Outline

In Chapter 2, I present the fundamental concepts and a brief history of quantum physics as it has evolved over the years. This background information is crucial for understanding the results discussed in the following chapters. I will introduce quantum light and its history, followed by a detailed explanation of photon statistics and measurement techniques, including the Hanbury Brown-Twiss experiment. I then explore different quantum light sources and delve into the material and optical properties of hexagonal boron nitride (hBN) in particular. Finally, I will introduce various techniques used to grow and characterize hBN films.

The remaining chapters of the thesis showcase the research conducted throughout the duration of my PhD. Chapter 3 and 4 consists of multiple experiments conducted to study and improve SPE creation. Chapter 5 presents published work achieved in collaboration with other researchers that master in the field. I am the first author or equal first author of any publications included in this thesis.

In Chapter 3, I present the experimental results gathered and analysed after the LPCVD growth of hBN. In the first section of the chapter, a parameter sweep was conducted to optimize the film growth, aiming to achieve single-photon emitters (SPEs) within a high-

quality and uniform film. This section outlines the optimal conditions required to incorporate stable and brighter SPEs in the film. The following part of the chapter focuses on another crucial aspect of growth i.e., studying the effect of growth chamber and corresponding environment on the quality of hBN growth.

Chapter 4 investigates the overgrowth of hexagonal boron nitride (hBN) on mechanically exfoliated hBN flakes via chemical vapor deposition (CVD). The aim is to assess the potential for homoepitaxial growth and interface continuity. Detailed analysis of surface morphology and thickness evolution is presented. Raman spectroscopy, Atomic Force Microscopy (AFM), and SEM were used to evaluate growth quality. Further optical measurements included photoluminescence (PL) and second-order autocorrelation measurements to test the SPE incorporation. The findings demonstrate conditions under which layered epitaxy is maintained, providing insights into scalable fabrication of high-quality hBN films.

Chapter 5 demonstrates successful integration of hBN defect with plasmonic gap cavity. In this publication we show successful boron-vacancy (V_B^-) defect creation using Focused ion beam (FIB). I am an equal first author of this publication with Noah Mendelson.

Chapter 6 includes the conclusion of the thesis and a summary of the work done so far. It also includes ideas for future work that could be conducted to further research and understanding of hBN film and SPEs.

In the appendix, I present the effects of carbon incorporation in hBN films during growth. This work was completed in collaboration, with the films grown overseas, while I characterized the properties of the films and incorporated single-photon emitters (SPEs) using confocal microscopy, including second-order autocorrelation measurements. The goal

of the paper is to demonstrate the precise control of defect structures in hexagonal boron nitride (hBN) to achieve tailored emission properties in single-photon emitters (SPEs) for integration into on-chip quantum devices.

2

Background

This chapter lays the conceptual foundations for understanding quantum light sources that arise from defects in two-dimensional (2D) materials, with particular emphasis on hexagonal boron nitride (hBN). The ability to generate single photons reliably and on demand is central to the development of quantum technologies, where precise control over the properties of light is indispensable. In emerging fields such as quantum computing and quantum key distribution (QKD), single-photon emitters serve as the building blocks for secure communication and scalable quantum architectures.

The discussion begins by outlining the physical principles of single-photon emission and the distinction between classical and quantum light sources. It then introduces hBN, describing its atomic structure and intrinsic material properties before reviewing the main approaches to its synthesis, ranging from high-pressure methods to chemical vapor deposition and molecular beam epitaxy. Following this, the chapter explores the role of

defects in hBN as hosts for single-photon emission, focusing on how their optical properties enable new

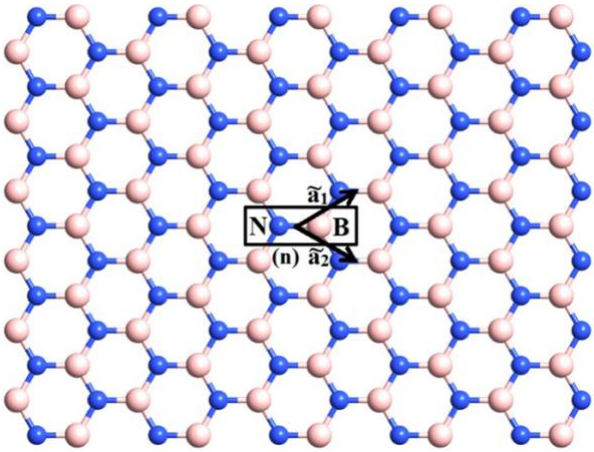

Figure 2.1: Atomic Structure of Hexagonal Boron Nitride (hBN). *Atomic structure of monolayer hBN showing the hexagonal arrangement of alternating boron (B) and nitrogen (N) atoms. The two-dimensional honeycomb lattice is defined by the primitive lattice vectors* $\hat{\mathbf{a}}_1$ *and* $\hat{\mathbf{a}}_2$*, with a single B–N pair forming the basis of the unit cell. The structure is isomorphic to graphene but with broken inversion symmetry due to the distinct atomic species. Reproduced from [1].*

avenues in quantum photonics. Finally, attention turns to the experimental techniques—microscopy and spectroscopy—that make it possible to visualise, characterise, and manipulate such emitters at the nanoscale. Together, these elements establish the framework required to interpret the results and discussions presented in later chapters.

2.1 Quantum Light

The move from classical to quantum light sources represents more than an incremental advance in optics; it has altered how photons are studied and applied. Classical sources such as lamps, LEDs and lasers produce light with statistical fluctuations that, while useful impose

limits on precision.[2–4] Quantum sources, by contrast, allow control at the single-photon level, where emission events can be timed and measured one by one.

This capability matters in practice. Quantum illumination has been tested in environmental sensing and biomedical imaging, often showing stronger sensitivity than classical beams because correlations between photons carry extra information.[5–8] Perhaps the most publicised application lies in communication. Quantum key distribution (QKD) encodes information into single photons, relying on entanglement and uncertainty: any interception disturbs the signal and is immediately apparent.[9–12] For encryption of sensitive data, this physical guarantee is stronger than conventional mathematical ciphers.

At the heart of these developments is the single-photon emitter. Such emitters differ from ordinary light sources by exhibiting antibunching which proves that photons emerge one at a time. The challenge is not only to produce them but to ensure brightness, spectral stability and indistinguishability. These demands drive ongoing work with quantum dots, diamond colour centres, and two-dimensional materials such as hBN.[13–20]

2.1.1 History

One of the most significant shifts in modern physics was the recognition that light is quantized. This idea first appeared in 1900, when Max Planck investigated blackbody radiation and proposed that electromagnetic energy is not continuous but emitted in discrete packets, later termed quanta. His model was designed to resolve inconsistencies in the classical thermal radiation theory, it laid the foundation of quantum mechanics and challenged long-standing views of light as a purely wave-like phenomenon.

Einstein advanced this concept in 1905 through his explanation of the photoelectric effect. He showed that light interacts with matter as discrete particles, now understood as

photons, rather than as a smooth electromagnetic wave. This provided strong experimental evidence that energy is delivered in finite units, initiating what became the quantum revolution. The dual wave–particle description of light emerged directly from these results.

The term "photon" was introduced in 1926 by Gilbert Lewis, giving formal identity to these quanta of the electromagnetic field. Each photon carries energy that scales with its frequency, described by the relation:

$$E = h\,v \qquad (2.1)$$

where, h (6.62607015×10^{-34} J s) is Planck's constant.[15,21-22]

This principle now underpins modern quantum electrodynamics, photonics, and quantum information science, linking foundational physics to applied technologies.

2.1.2 Photon Statistics

Photon statistics provide a rigorous framework for distinguishing between different kinds of light sources by analysing how photons are distributed over time. Instead of focusing solely on average intensity, this approach considers fluctuations and correlations in photon arrival, which reveal whether a source is governed by classical physics or exhibits fundamentally quantum behaviour. This classification into thermal, coherent, and single-photon emission regimes has become foundational for modern optics and quantum photonics.

Thermal Light generated by incandescent lamps, discharge tubes, or sunlight, is governed by a *super-Poissonian* distribution. In such cases, emission events are correlated, producing **photon bunching**, where photons arrive in bursts rather than independently. The variance of photon counts greatly exceeds the mean, leading to significant noise in intensity.

This arises from the random fluctuations of phase and amplitude that characterise thermal radiation. Although thermal light lacks quantum utility, its statistical description is vital in understanding classical emission sources.

Coherent Light: produced by lasers, exhibits a *Poissonian* distribution. Here, photon arrivals are independent, and the variance equals the mean photon number. This means that while photons are not anti-bunched, they retain a stable phase relationship, providing coherence across long distances and timescales. This property underlies the extraordinary usefulness of lasers in applications ranging from fibre-optic communication to high-precision metrology. Nevertheless, the Poissonian character means there remains a finite chance of multiphoton events, limiting their use for strictly quantum-secure applications.

Single Photon Sources: display *sub-Poissonian* statistics, where photons are emitted one at a time, separated by well-defined intervals. This antibunching effect has no classical analogue and arises directly from quantum mechanical principles. Such behaviour makes single-photon sources indispensable for quantum key distribution, quantum logic operations, and advanced sensing. Recent developments have demonstrated single-photon emission from quantum dots, colour centres in diamond, and defects in layered materials such as hexagonal boron nitride.

The Poisson function describes the probability *P(X)* of a given number of events occurring within a fixed time interval.

$$P(X = n) = \frac{e^{-\lambda}\lambda^{n}}{n!} \qquad (2.2)$$

In *equation 2.2,* λ is the expected number of photons, e is Euler's constant, and n is the detected photon count. For thermal sources, variance greatly exceeds the mean, confirming bunching behaviour.

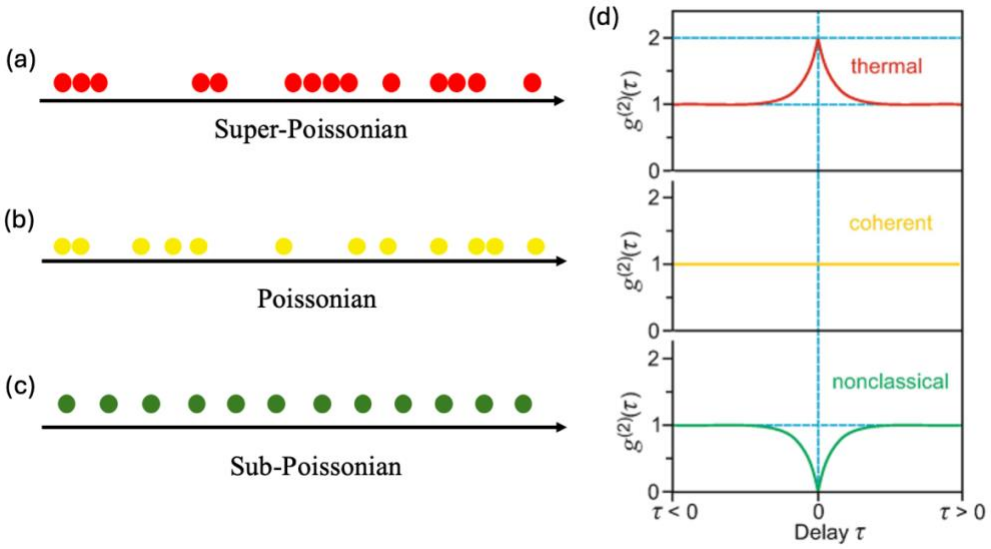

Figure 2.2: Schematic of three types of light sources. *(a) Photon bunching in a thermal source with a super-Poissonian distribution. (b) Random photon spacing in coherent light. (c) Photon antibunching in a single-photon source. (d) Corresponding second-order intensity correlation functions. Reproduced from [25].*

For coherent sources, variance equals the mean, consistent with independent arrivals. For single-photon emitters, variance falls below the mean, providing evidence of antibunching.

These statistical signatures are not merely abstract concepts but can be measured directly through correlation experiments. The second-order autocorrelation function, $g^{(2)}(\tau)$, serves as the primary diagnostic tool. At zero-time delay, distinct values are observed:

- Thermal light: $g^{(2)}(0) > 1$, indicating bunching.
- Coherent light: $g^{(2)}(0) = 1$, corresponding to independent events.
- Single-photon sources: $g^{(2)}(0) < 0.5$, unambiguously indicating antibunching.

and quantum emission. Such measurements have become standard in verifying new quantum emitters, including those in hexagonal boron nitride and other two-dimensional materials.

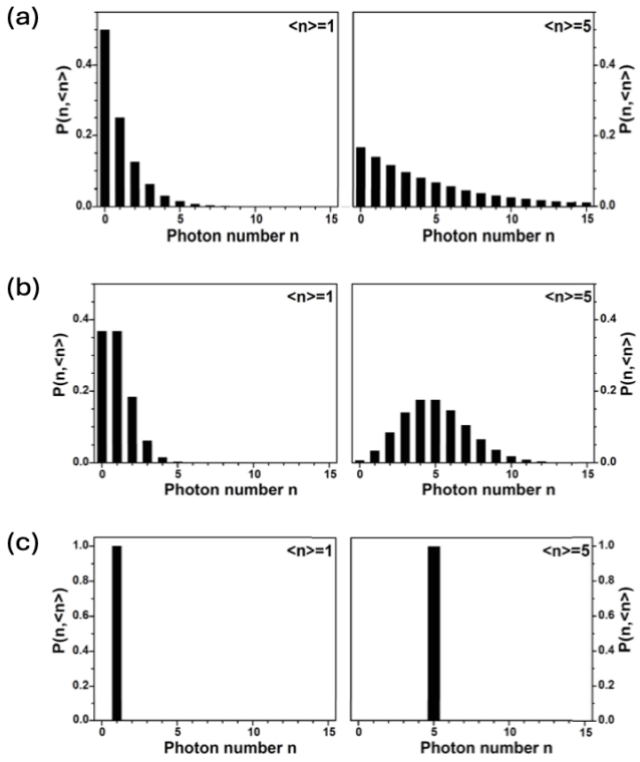

Figure 2.3: Photon number distributions for three regimes of light*. (a) Thermal state with average photon number of 1 (left) and 5 (right), showing high variance and photon bunching. (b) Coherent state with averages of 1 and 5, displaying a Poisson distribution. (c) Single-photon state with averages of 1 and 5, showing strong suppression of multiphoton events. Reproduced from [26].*

In thermal light sources *fig 2.3 (a)*, the distribution is broad, with high likelihood for multiple photons, consistent with noisy intensity fluctuations. For coherent light *fig 2.3 (b*), the probability is peaked at one photon but remains finite for higher counts. For single-photon sources *fig 2.3 (c*), the probability distribution is sharply narrowed, confirming suppression

of multiphoton events. Together, these statistical and experimental signatures provide a robust framework for identifying new quantum emitters and assessing their suitability for integration into quantum photonic devices.

2.1.2.1 Photoluminescence emission

Photoluminescence (PL) spectroscopy has become one of the most widely used techniques for probing quantum emitters because it allows researchers to study light–matter interactions in a direct and relatively simple way. The basic process involves three steps: absorption of an incoming photon, excitation of an electron into a higher energy state, and subsequent relaxation back to the ground state with the release of another photon. When such emission originates from a localised defect site, the transition can occur one photon at a time, which makes PL particularly effective for identifying single-photon emitters (SPEs).

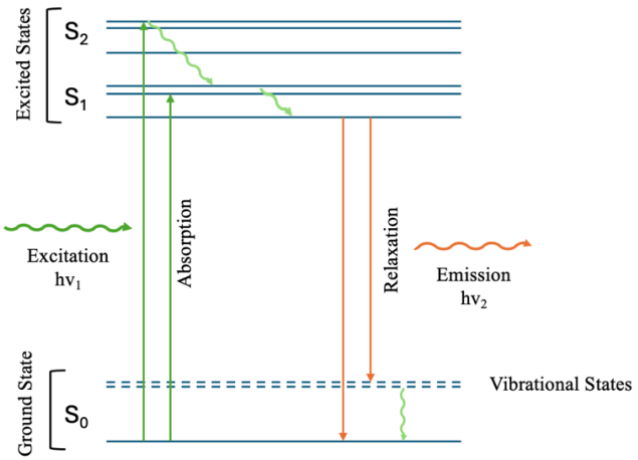

Figure 2.4: *Photoluminescence (PL) spectroscopy schematic of a Two-level system.*

PL spectroscopy offers significant advantages for 2D materials, as their planar structure allows for easy integration with photonic and electronic systems. The reduced

dielectric screening enhances light-matter interactions, improving the efficiency and brightness of single-photon emission. By engineering defects in various 2D materials, the emission wavelength can be tailored for specific applications, making them ideal for quantum photonics and emerging technologies.

In practice, PL measurements can be carried out in continuous-wave or pulsed excitation modes. Each approach provides different insights: steady-state spectra give information on emission energy and linewidth, while time-resolved PL can reveal fluorescence lifetimes and coherence properties. Mapping emission intensity across a flake further makes it possible to locate individual quantum emitters and study how they are distributed within a sample. Taken together, these capabilities explain why PL remains central in the study of defect-based emitters.

2.1.2.2 Hanbury Brown-Twiss Experiment

While PL reveals emission characteristics, it does not on its own prove that photons are emitted individually. For that purpose, the Hanbury Brown–Twiss (HBT) experiment is indispensable. Originally developed for measuring stellar light, it is now the standard tool for identifying single-photon behaviour.

In a typical HBT setup *fig. (2.5*), light from the emitter is divided by a 50:50 beamsplitter and directed to two detectors usually avalanche photodiodes (APDs). The detection events are then processed using time-correlated single-photon counting (TCSPC), which records arrival times with picosecond precision. From these data, the second-order autocorrelation function, $g^{(2)}(\tau)$ is calculated.

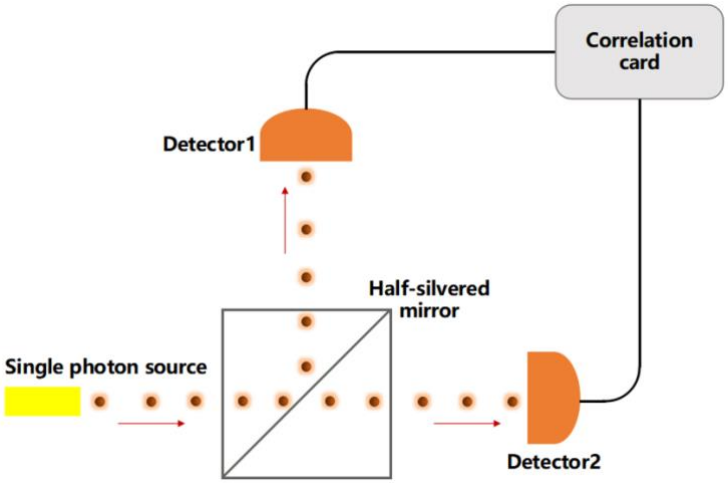

Figure 2.5: *Schematic of Hanbury Brown and Twiss interferometer.*

The diagnostic power of this method is clear: thermal sources show $g^{(2)}(0) > 1$, coherent sources yield $g^{(2)}(0) = 1$, and single-photon emitters fall below 0.5, providing evidence of antibunching. In practice, experimental imperfections, detector noise, and background signals can push values away from these theoretical limits, but measurements consistently below unity are taken as proof of quantum emission.

APDs though fast, suffer from dead time i.e., the period after a detection event when the detector is temporarily unresponsive. This would be a serious limitation if only one detector were used. By splitting the incoming photons across two detectors, the HBT design effectively removes this problem, allowing accurate coincidence measurements.

Taken together, PL spectroscopy and HBT correlation form a complementary toolkit. PL establishes the spectral and spatial features of an emitter, while HBT confirms its quantum character. These techniques underpin almost all experimental studies of defect-based single-

photon sources and continue to provide the benchmarks for evaluating their performance in emerging quantum technologies.

2.1.3 Quantum Light Sources

The nitrogen–vacancy (NV) centre in diamond is one of the most extensively studied quantum defects. Structurally, it is a point defect with *C3v* symmetry, composed of a substitutional nitrogen atom adjacent to a lattice vacancy aligned along the [111] crystallographic axis. NV centres are distinguished by their sharp zero-phonon lines (ZPLs), appearing at 637 nm for the negatively charged state (NV^-) and 575 nm for the neutral state (NV0). Considerable progress has been made in enhancing photon collection from NV centres through the use of solid immersion lenses, micro-fabricated structures, and optical resonators.[27] Other important diamond defects include the silicon-vacancy (SiV^-) centre, first identified in the early 1980s, which emits at 738 nm with a narrow ZPL but suffers from limited quantum efficiency and short spin coherence times. More recent work has uncovered additional group-IV defects such as the germanium-vacancy (GeV), tin-vacancy (SnV), and lead-vacancy (PbV) centres.

Group-IV defects present several advantages over NV centres. Their inversion symmetry suppresses sensitivity to local electric field fluctuations, which reduces spectral diffusion and allows for nearly lifetime-limited optical emission. This symmetry also ensures more reproducible emitter properties, supporting the scalability of quantum devices. In practice, their sharp ZPLs provide enhanced optical coherence and make them easier to integrate with photonic structures. However, these centres still face limitations, notably their relatively low quantum efficiency.[28]

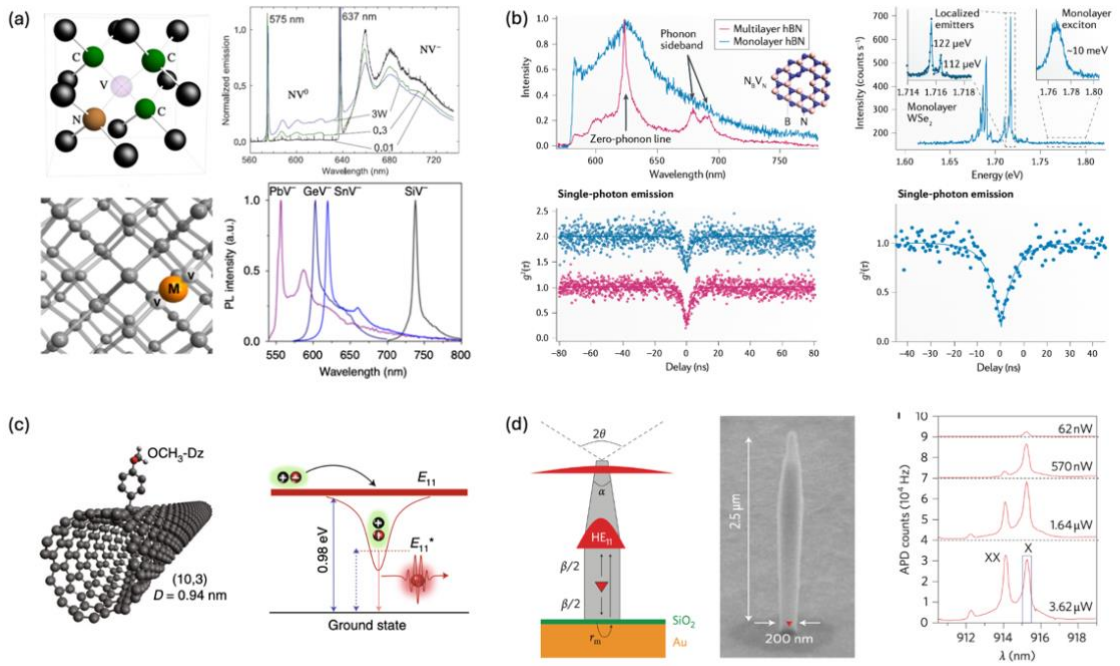

Figure 2.6: Quantum Light sources *(a) NV defect structure (top-left) and corresponding optical emission (top-right) Group IV colour centre structure and the corresponding PL emission. (b) PL spectra from monolayer and multilayer hBN (top-left), the defects act as SPE, evident by the antibunching curves (bottom). PL spectra from monolayer* WSe_2 *(top-right) and the* $g^{(2)}$ *curve from the corresponding defect (bottom). (c) Schematic of Single Walled Carbon Nanotubes (SWCNTs) demonstrating creation of controlled defects. (d) GaAs nanowire with embedded InAs QD (left), SEM image of the structure (middle). PL spectra of the photonic nanowire QD with increasing power (right). Reproduced from [27,28,29,30,31]*

Over the past two decades, two-dimensional (2D) materials have emerged as an alternative host platform for single-photon emitters (SPEs). Transition metal dichalcogenides (TMDCs) and hexagonal boron nitride (hBN) are of particular interest. While TMDCs can host quantum emitters, their operation is generally restricted to cryogenic temperatures. In contrast, hBN defects exhibit stable emission at room temperature owing to deep defect states within the bandgap. These emitters combine high brightness with efficient light extraction and straightforward integration into photonic devices. Among reported 2D emitters, hBN

stands out as one of the brightest, achieving high photon flux with low excitation power. Nevertheless, further work is required to fully resolve their electronic structures, in contrast to diamond colour centres, which have been studied in depth.[17,29]

Semiconducting carbon nanotubes (CNTs) have also been demonstrated to host SPEs. Their combination of electronic and mechanical properties makes them attractive for use in optomechanical circuits, and their emission wavelengths overlap with the telecom band, supporting integration with fibre-optic systems. However, CNT based emitters typically require cryogenic cooling, as they are prone to spectral instability, including blinking, bleaching, and dephasing. Efforts continue to improve their brightness and stability.[30]

Semiconductor quantum dots, such as InAs/GaAs, are regarded as excellent single-photon sources because of their strong optical characteristics and their ability to deliver photons on demand, sometimes even at room temperature. Yet, much like carbon nanotubes, maintaining quantum coherence generally requires cryogenic cooling. Quantum dots remain highly promising for future applications in quantum communication and computing. By contrast, colour centres in materials such as hexagonal boron nitride (hBN) and transition metal dichalcogenides (TMDs) can emit single photons efficiently at room temperature. Their defect states generate localized electronic levels within the bandgap, providing stable and well-controlled photon emission.[31]

2.2 Hexagonal Boron Nitride (hBN)

Hexagonal boron nitride (hBN) was first prepared in 1842 by the English chemist W.H. Balmain.[32] At that stage its significance was not at all obvious, and for much of the nineteenth century it attracted limited attention. Only in the middle of the twentieth century

did its structure begin to be clarified. Researchers then recognised that it shares a layered architecture very similar to graphite, though with quite distinct electronic behaviour. From that point onwards hBN was examined both as a useful ceramic, valued for its high thermal stability, chemical inertness, role as a lubricant and more recently as a material with unusual quantum optical properties. A key reason for this renewed interest is its ability to host atomic-scale defects that can function as single-photon emitters.

Structurally, hBN is crystalline and has a two-dimensional honeycomb network of alternating boron and nitrogen atoms.[33] The bonds are partly ionic because of the electronegativity contrast, which makes them different from the purely covalent bonds in graphene. Its wide indirect bandgap, near 5.9 eV, explains why it behaves as an excellent insulator and why it is stable under high temperatures. Mechanically it is extremely strong: the Young's modulus is close to 0.865 TPa and the fracture strength around 70 GPa. Importantly, these mechanical values do not vary much with layer thickness, showing that the interlayer coupling remains robust across different forms of the crystal.

2.2.1 Material Properties

Hexagonal boron nitride (hBN) features a honeycomb lattice structure, much like graphene, with alternating boron and nitrogen atoms bonded together. Within each layer, boron and nitrogen atoms form bonds that are mostly covalent with a degree of ionic character. Weak van der Waals forces dominate between the layers of hBN (interlayer), with a minor ionic contribution.[34–40] This difference between strong in-plane and weak out-of-plane bonding gives hBN both rigidity and flexibility. Unlike graphene, which usually shows AB stacking, hBN follows an AA′ sequence where boron in one layer lies above nitrogen in the next.[41] This stacking reinforces registry between layers and contributes to its stability.

Stacking also changes other behaviours. As more layers are added, dielectric strength increases, making hBN an attractive choice for insulating layers in advanced electronics.[42–44] On the other hand, thicker crystals experience more phonon scattering, which tends to reduce thermal conductivity, and the material remains effective at dissipating heat. Because of its strong bonding within the planes and insulating nature, hBN is widely used as a protective coating or encapsulant in van der Waals heterostructures, preserving the qualities of materials like graphene without degrading them.[45,46]

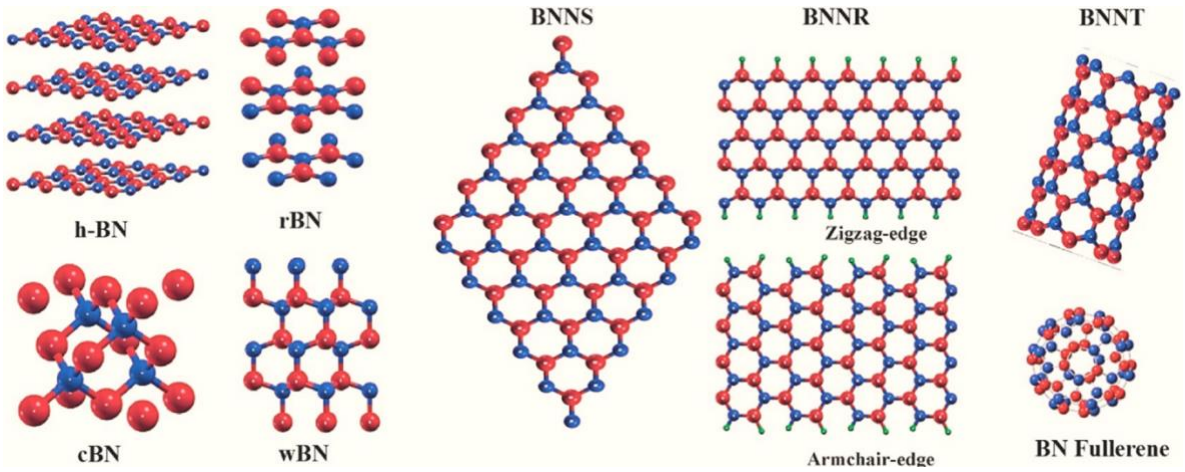

Figure 2.7: Schematic representation of the structural diversity of boron nitride (BN) materials, showing various crystalline phases*. hexagonal (h-BN), cubic (c-BN), rhombohedral (r-BN), and wurtzite (w-BN)—as well as nanostructured forms including BN nanosheets (BNNS), nanoribbons (BNNR, with zigzag and armchair edges), nanotubes (BNNT), and fullerenes. Adapted and modified from Ref. [55].*

The lattice parameters of hexagonal boron nitride are approximately 0.25 nm in the basal plane and 0.333 nm along the c-axis. These dimensions permit, though not without considerable difficulty, the isolation of monolayer and few-layer flakes by mechanical exfoliation, high-energy ball milling, or chemical solvent–assisted techniques. In comparison with graphene, the stronger interlayer adhesion of hBN introduces additional challenges to exfoliation; nevertheless, high-quality thin layers have been reliably produced.[47]

Because of its wide bandgap of ~5.9 eV, bulk hBN exhibits negligible absorption across the visible and near-infrared spectrum, giving it a characteristically white appearance in powdered or crystalline form. This electronic structure, coupled with its intrinsically low defect density, makes hBN a highly suitable substrate for other two-dimensional materials such as graphene and transition-metal dichalcogenides, where it improves carrier mobility by reducing charge scattering at the interface.[47,48] In addition, its moderate dielectric constant allows it to act as an atomically thin tunnelling barrier, supporting precise electron transport while effectively suppressing leakage currents. In few-layer form, hBN retains strong insulating behaviour, thereby enhancing the performance and stability of transistors, photodetectors, and other layered optoelectronic systems.[49]

The thermal transport properties of hBN are equally remarkable. Depending on crystalline alignment, thickness, and purity, the in-plane thermal conductivity has been reported to vary between approximately 300 and 2000 $W \cdot m^{-1} \cdot K^{-1}$.[50] This high conductivity is generally attributed to the light atomic masses of boron and nitrogen in combination with the rigidity of the B–N bonds, which promote efficient phonon transport pathways. In monolayer form, the absence of interlayer phonon scattering further enhances conductivity, frequently surpassing that of multilayer specimens.

hBN monolayer has an in-plane stiffness of roughly 267 $N \cdot m^{-1}$. This value is a little lower than the ~335 $N \cdot m^{-1}$ recorded for graphene, the value is still very high compared with the majority of other layered or bulk crystalline materials.[231] In practice, this means that hBN sheets can withstand considerable stress without structural failure, while also keeping their form across different thicknesses. Together with its unusual thermal conductivity and its resistance to chemical degradation, these mechanical properties make hBN a material that

can be pushed into a variety of advanced applications. Current research already points to roles in nanoscale heat spreading, transistor stabilisation, and more recently in experimental quantum electronic devices, where both strength and stability are required alongside insulating behaviour.

2.2.2 Optical Properties

In addition to its more established industrial uses, such as lubricants and thermal insulators, hexagonal boron nitride (hBN) has become increasingly significant within photonics and quantum optics. The turning point was the observation of ultraviolet (UV) emission and lasing from bulk crystals, which at the time appeared to support a direct-bandgap interpretation.[48] Subsequent studies, however, argued instead for an indirect bandgap,[52–54] which has complicated the picture and left aspects of its optical behaviour under debate. Much of the uncertainty stems from the strong role of excitons, phonons, and defect-related states, all of which influence the observed spectra in ways that are not always straightforward to separate experimentally. For example, impurity-bound excitons are often found to dominate lower-energy emission features, yet their microscopic origin is not yet universally agreed upon.

Beyond these band-structure considerations, hBN displays another remarkable property i.e., natural hyperbolicity.[37] This arises from the pronounced anisotropy in its refractive indices. When driven in the mid-infrared or terahertz range, the material sustains surface phonon–polaritons (SPPs), which can confine light well below the diffraction limit. Such behaviour enables applications ranging from sub-diffraction imaging to nanoscale waveguiding, areas where conventional dielectrics are far less effective. The capacity to control and manipulate light at this scale has placed hBN among the leading candidates for advanced nanophotonic systems.

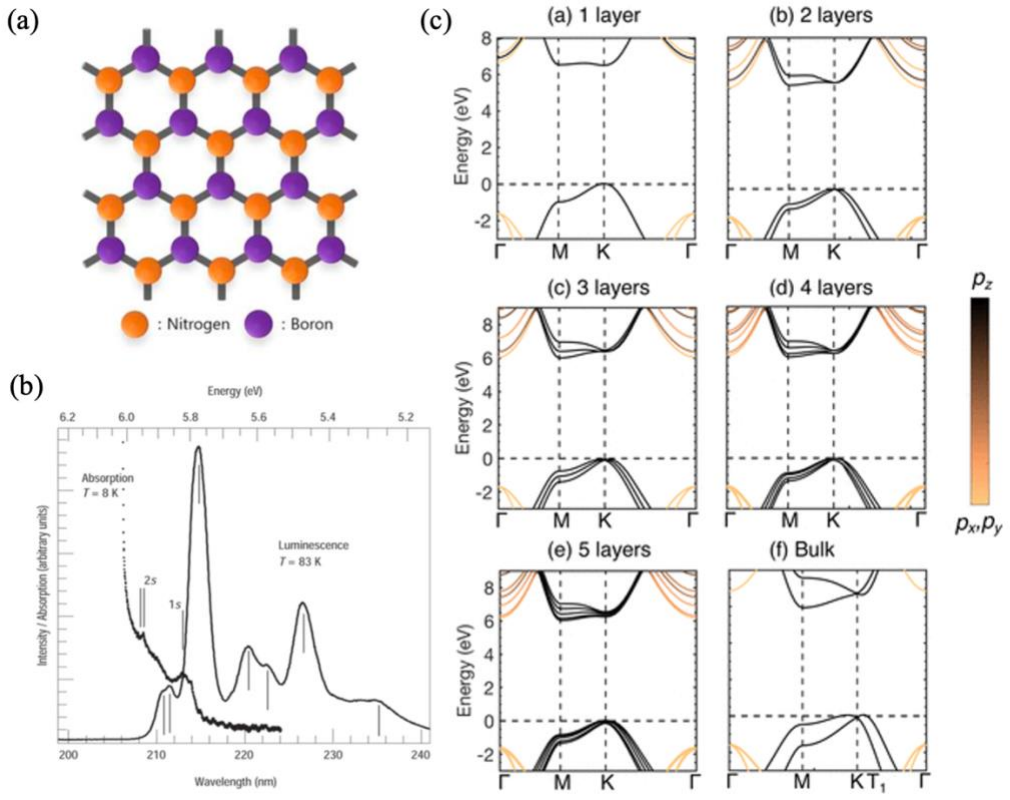

Figure 2.8: hBN Lattice, Excitonic Spectra, and Thickness-Dependent Band Structure*. (a) Schematic of the hexagonal boron nitride (hBN) lattice with* ***N*** *(orange) and* ***B*** *(purple) atoms. (b) Fundamental absorption (8 K) and photoluminescence (83 K) spectra of bulk hBN showing pronounced excitonic features; weak Fabry–Pérot fringes from ~213–224 nm visible in the absorption trace. Vertical bars mark the peak positions (labels indicate the 1s and 2s excitons). (c) Layer-dependent electronic band structures for 1–5 layers and bulk along M–K–Γ (bulk includes* T_1*), with the colour scale denoting orbital character from out-of-plane* p_z *(dark) to in-plane* p_x/p_y*(light). With increasing thickness, hBN evolves from a direct-gap monolayer to an indirect-gap bulk crystal. Adapted and modified from Ref. [48,51,67].*

Equally important is the discovery that hBN can host highly stable single-photon emitters (SPEs). Since the first reports, it has been shown that a wide spectral range from the ultraviolet through the visible and into the near-infrared can be covered by defect-related emission. These SPEs stand out for their exceptional brightness and stability: emission rates often exceed one million photons per second, and plasmonic coupling can increase output

further.[56,57] The thin, layered geometry of hBN is also advantageous, as emitters sit close to the surface and light extraction is more efficient compared to bulk hosts such as diamond.

Within the growing catalogue of hBN defects, ultraviolet emitters and the negatively charged boron vacancy (V_B^-) have drawn particular interest. The V_B^- defect is notable not only for its near-infrared emission but also for its triplet ground state, which offers potential for spin–photon interfacing at room temperature.[58,59] Additionally, hBN-based emitters are strongly tunable. Both local strain and external electric fields have been used to shift emission wavelengths and modulate intensity, a feature that is highly desirable when integrating SPEs into scalable quantum photonic circuits.

Taken together, these studies emphasise that the optical behaviour of hBN cannot be described by a single phenomenon. Instead, it reflects a combination of excitonic recombination, hyperbolic polaritonic modes, and defect-mediated single-photon emission. The field continues to evolve quickly, with ongoing work in defect identification and control likely to determine how far hBN can be pushed as a foundation for quantum photonics and related technologies.

2.2.2.1 Defects in hBN

Hexagonal boron nitride (hBN) has gained substantial interest owing to its unique optical and electronic characteristics, particularly its capacity to host optically active defects. These colour centres are localised disruptions in the hBN lattice that can emit single photons at room temperature, making them highly valuable for quantum information technologies. [56,

[60] The wide bandgap of hBN (~ 6 eV) enables these defects to act as stable emission centres, typically detected across the visible to near-infrared spectrum. [61]

Identifying and characterising various defects in hBN is vital for understanding their roles in light emission and for engineering tailored quantum light sources. [62–63] Such defects may occur naturally during crystal growth or be deliberately introduced through approaches such as ion implantation, chemical vapour deposition (CVD), or electron beam irradiation. [64] Each defect type produces a distinct zero-phonon line (ZPL) in photoluminescence spectra, making spectroscopy a primary tool for defect identification. [65]

The most widely studied point defects in hBN include the boron vacancy (V_B^-), nitrogen vacancy (V_N), antisite complexes, and carbon or oxygen-based impurities. [66] The negatively charged boron vacancy is a spin-active defect with a triplet ground state, accessible via optically detected magnetic resonance (ODMR). Unlike other visible centres, V_B^- consistently shows a photoluminescence peak near ~ 850 nm when excited with a green laser. [67] Although many reports describe bright single-photon emission in hBN, there is no conclusive experimental evidence attributing this emission to isolated V_N defects, with most claims resting on indirect comparisons between PL spectra and density functional theory (DFT) simulations. [68] This remains an emerging research area, requiring further advances in combined spectroscopy, atomic-resolution microscopy, and spin-resolved methods to clarify the microscopic role of VN in hBN luminescence. [69]

Antisite defects, where boron and nitrogen atoms exchange lattice positions, generate more complex spectral features owing to their varied atomic configurations.[70] Carbon-related centres, formed from substitutional or interstitial carbon, add to the defect diversity and are

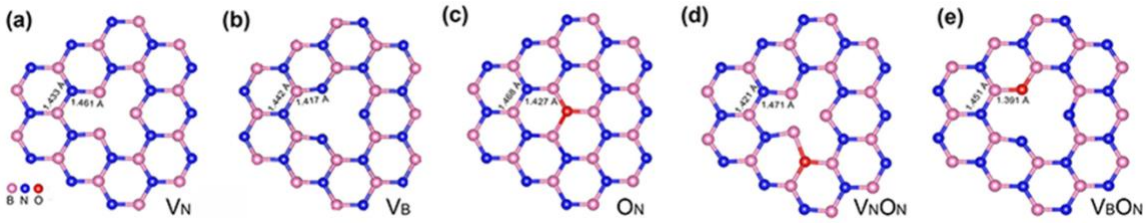

Figure 2.9: Monolayer hBN Point Defects and Local Bond Distortions (V_N, V_B, O-related complexes). *(a) Schematic of a single nitrogen vacancy in monolayer hBN (V_N). (b) Single boron vacancy (V_B). (c) Oxygen substituting a nitrogen site (O_N). (d) V_NO_N complex (oxygen at a neighbouring N site adjacent to a nitrogen vacancy). (e) V_BO_N complex (oxygen at a neighbouring N site adjacent to a boron vacancy). Blue, pink and red spheres denote B, N and O atoms, respectively. The dashed segment marks a representative nearest neighbour B–N bond length in each relaxed structure (a–e: 1.469, 1.417, 1.427, 1.471 and 1.391 Å), highlighting defect-induced bond contraction/elongation around the defect core. Adapted and modified from Ref. [83].*

frequently linked to visible single-photon emission. In addition, more complex defects such as vacancy clusters or foreign impurities (oxygen or carbon incorporated into the lattice) introduce further electronic levels and local disorder. This expanding defect complexity makes precise identification and analysis increasingly challenging. [71–74]

Recent research has connected specific spectral emissions with atomic defect types. For instance, ultraviolet (UV) and deep-UV (DUV) emission has been attributed to boron-related defects, whereas near-infrared (NIR) emission is often correlated with carbon impurities in the lattice. [71, 75] Understanding such links is crucial for tuning hBN's optical response in quantum photonic systems.

***Table 2.1**: Summary of common defect types in hBN and their optical signatures.*

Defect Type	**ZPL**	**Origin**	**Identification**
Boron Vacancy V_B^-	850 nm	Ion implantation e- irradiation CVD [66-67]	PL ODMR RAMAN
Nitrogen Vacancy	Visible - NIR	CVD/ MBE Irradiation [68-69]	PL DFT
Antisite (B ↔N)	Broad Visible range	Growth Irradiation [70]	PL RAMAN
C- defects	Visible - NIR	Substitutional CVD [71, 75]	PL STEM
O impurities	UV - Visible	Incorporation during-(CVD or Annealing) [71-74]	PL STEM EPR
Blue Centres	~ 436 nm UV link (~ 305 nm)	e- beam Irradiation [76-82]	PL Stark Tuning

One particularly studied class is the "blue" colour centres in hBN, which show sharp single-photon emission with a ZPL around 436 nm. These blue emitters were first identified in high-quality hBN by Shevitski et al., who demonstrated electron-beam activation and reversible switching behaviour consistent with atomic colour centres. [76] Later work achieved deterministic and site-controlled fabrication of the 436 nm centres using focused electron-beam irradiation and confirmed their association with a UV defect at ~305 nm. [77] Follow-up investigations examined coherence, resonant behaviour, and Stark-shift properties under cryogenic conditions, revealing narrow homogeneous linewidths, resilience to moderate electric-field noise, and identifying phonon-driven dephasing and spectral diffusion as key coherence-limiting mechanisms.[78–80] Studies on robustness and post-processing (e.g.,

annealing, carbon-doping) refined fabrication protocols and emphasised the role of carbon precursors in improving emitter yield. [81] Quantitative optical analysis (quantum efficiency and lifetime measurements) showed promising brightness and moderate quantum yield for these so-called B-centres.[82] Recent theoretical work employing hybrid-DFT and many-body approaches has proposed possible atomic models, including the negatively charged nitrogen split-interstitial, as the microscopic origin of the 436 nm emitter, though definitive experimental proof at the atomic scale is still pending. [74]

A rapidly developing area involves engineered defect creation to produce on-demand quantum emitters. Strategies such as focused ion irradiation and laser-based writing allow precise spatial control of defect density and positioning.[83] Moreover, the emission properties of these centres can be tuned by external strain or electric fields, offering dynamic control for quantum devices.[84]

Advanced characterisation techniques including cathodoluminescence (CL), Raman spectroscopy, and electron paramagnetic resonance (EPR) are routinely combined with PL studies to probe the structure and electronic states of hBN defects.[72, 85–86] Additionally, scanning transmission electron microscopy (STEM) enables direct imaging of defect sites, providing atomically resolved insights into their structure and distribution.[87–88]

In conclusion, the identification and manipulation of specific defect types are crucial to unlocking hBN's potential as a quantum light source. Through advanced spectroscopic and microscopic analysis, researchers are moving towards deterministic design of single-photon emitters with optimised performance, strengthening hBN's position as a leading platform for emerging quantum technologies.[71–74, 89]

2.3 Synthesis of hBN film

The synthesis of hexagonal boron nitride (hBN) films has seen significant advancements due to their unique properties and broad application potential in various technological fields, including optoelectronics and quantum computing. Different growth techniques have been explored, each with its own advantages and limitations.

2.3.1 High Pressure High Temperature (HPHT)

The high-pressure high-temperature (HPHT) remains the definitive method for producing benchmark quality hexagonal boron nitride (hBN) crystals. By recreating the thermodynamic window in which sp^2 bonded BN is stable at GPa pressures and temperatures exceeding ~1500 °C, HPHT growth yields colourless, low defect platelets whose deep UV optical response has underpinned both the fundamental physics of excitons in hBN and most relevant device demonstrations in the hBN history [90, 91, 96, 100]. Although wafer scale films are not achievable by HPHT and the process is capital and expertise intensive, it establishes the quality benchmark against which more scalable thin-film routes (CVD & MOVPE) are judged. The central trade-off is therefore clear, unmatched crystal quality and optical purity versus intrinsic constraints on lateral size and throughput [90–93].

In a canonical HPHT run, carefully purified boron and nitrogen charges are combined with a nitride flux inside a hexagonal BN (hBN) crucible, the assembly is loaded into a multi-anvil (cubic-anvil, belt, or toroidal) press, pressure is raised into the 3–6 GPa range and temperature is driven to roughly 1500–1950 °C. After the charge dissolves in the molten flux, hBN crystal nucleates and re-precipitates under a mild axial thermal gradient that maintains

solute transport during an isothermal or slightly undercooled dwell, typically of order 1–12 hr. Controlled cooling promotes domain coarsening and reduces defect incorporation. The assembly is then quenched, depressurized and the crystals are recovered by dissolving the flux (often via acid/base cleaning) before any optional post-growth anneal.

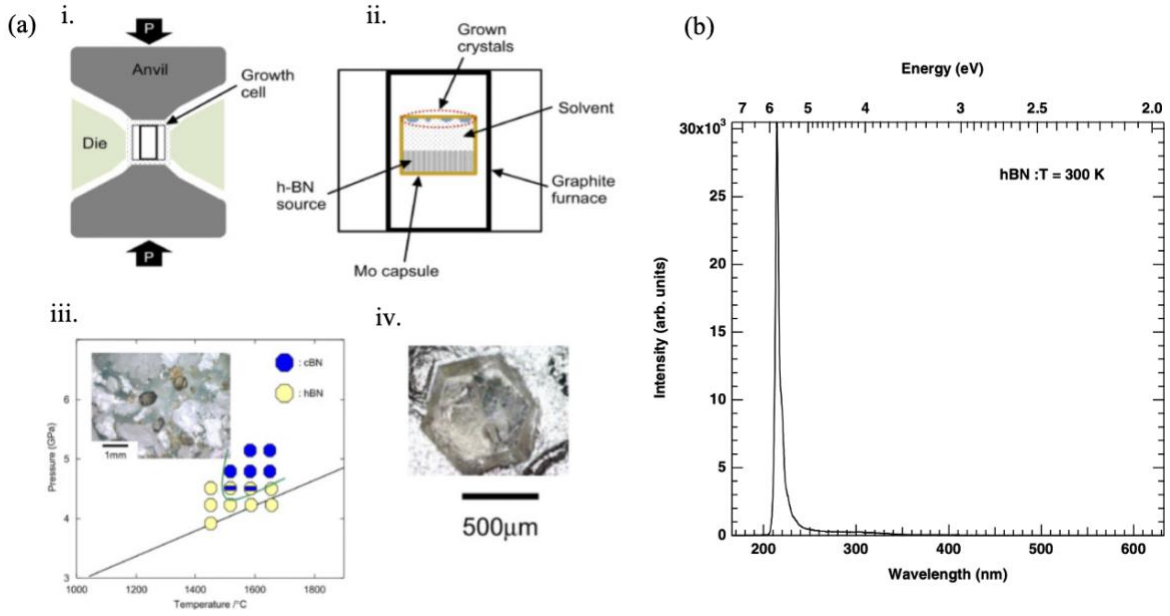

Figure 2.10: HPHT Growth of hBN and Room-Temperature Optical Response. *(a) High-pressure, high-temperature (HPHT) crystal growth process. (i) Schematic of the cubic-anvil high-pressure apparatus containing the growth cell. (ii) Cross-sectional illustration of the Mo capsule assembly showing the h-BN source, molten solvent, and graphite furnace used to promote crystal growth. (iii) Pressure–temperature phase region for crystal formation, with experimental data points indicating h-BN and c-BN domains (inset: recovered crystal batch). (iv) Optical micrograph of a representative hexagonal BN crystal (~500 µm lateral dimension). (b) UV absorption spectrum of h-BN at 300 K, showing a sharp absorption edge near ~6 eV corresponding to the wide bandgap of the material. Reproduced from [85,90].*

While the precise window depends on the solvent chemistry, Ba–BN solutions are usually operated near 4.5– 5.5 GPa and 1500–1650 °C. Mg–B–N routes reach higher temperatures and involve a well-documented $MgNB_9$ intermediate, the overall sequence of dissolution,

transport under gradient, and re-precipitation is consistent across reports and is now considered standard practice for HPHT hBN [91–93].

Flux chemistry dictates much of the materials outcome. Barium boron nitride solvents (often summarized as Ba–BN or $Ba_3B_2N_4$ families) have long been associated with ultra-low contamination, routinely producing hBN with oxygen and carbon concent rations below ~10^{18} cm^{-3} and sharp deep-UV band edge signatures. Such Ba flux crystals are the ones historically used to establish excitonic luminescence near ~215–225 nm and to demonstrate lasing-like behaviour at cryogenic temperatures, results that catalysed the modern wave of deep-UV hBN optoelectronics [90–91, 100]. Magnesium-based solvent routes (Mg–B–N) have clarified the mechanistic pathway through the $MgNB_9$ phase and offer higher-temperature operation with vigorous mass transport but require care to avoid parasitic phases and to maintain stoichiometry. Most recently, strontium-based nitride solvents (e.g., $Sr_3B_2N_4$) have emerged as a credible alternative, yielding transparent single crystals with lateral sizes approaching ~1.2 mm at ~4.5 GPa/1500 °C this development underscores that solvent design remains an active and fruitful lever for quality and size, even within the size constraints imposed by the press capsule [92–94].

Capsule thermal gradients and transport kinetics imprint directly on crystal morphology and output. With minimized thermal inhomogeneity and good solvent wetting, single growth cycles routinely produce platelets 0.5 – 3 mm across and tens to hundreds of micrometres thick. Consistently, the Sr-flux variant reports ~1.2 mm platelets at 4.5 GPa/1500 °C, reflecting efficient mass transport and clean interfacial kinetics. Larger sizes are predominantly capped by crucible dimensions, solvent volume and the stability of the thermal gradient over multi-hour dwells. Thus, HPHT is not a wafer-film technique. Its

practical role is to supply high-quality bulk hBN from which flakes are mechanically exfoliated and then transferred onto target substrates.[92–94]

Quality metrics recorded on HPHT hBN are widely considered the gold standard for bulk material. Raman spectroscopy exhibits the archetypal E_2g phonon near 1366 cm^{-1} with narrow full-width at half-maximum, reflecting low disorder and minimal strain in the grown crystals. Electron and x-ray diffraction reveal sharp hexagonal symmetry with strong (002) texture and minimal mosaic spread.

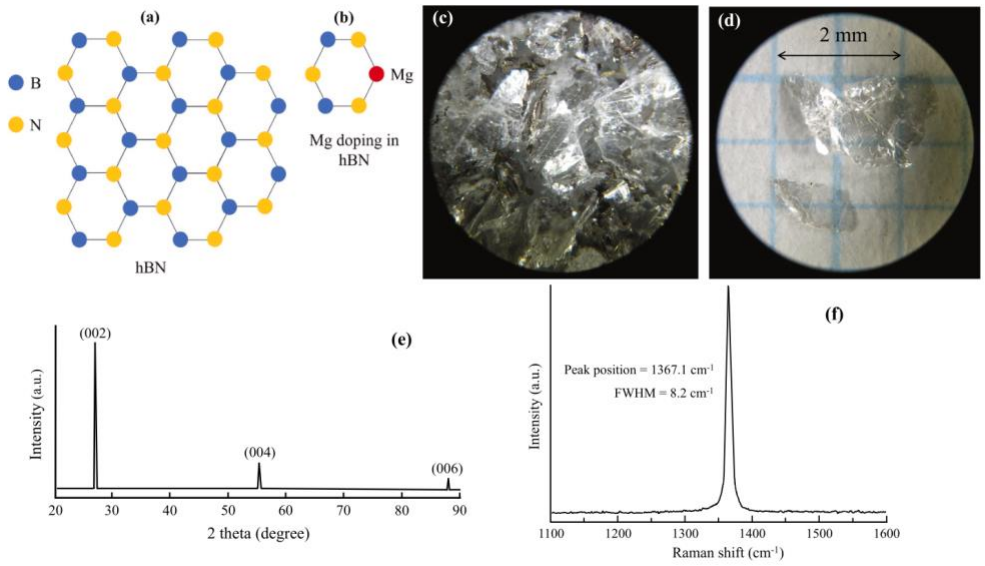

Figure 2.11: Mg-Doped hBN Crystal Structure and Characterization. *(a) Atomic lattice model of pristine hexagonal boron nitride (hBN). (b) Schematic representation of Mg incorporation into the hBN lattice. (c–d) Optical microscope images of synthesized Mg-doped hBN crystal fragments, showing transparent platelet morphology with lateral dimensions of up to ~2 mm. (e) X-ray diffraction (XRD) pattern confirming the characteristic (002), (004), and (006) reflections of layered hBN. (f) Raman spectrum displaying the E_2g phonon mode centered at 1367.1 cm^{-1} with a full width at half maximum (FWHM) of 8.2 cm^{-1}, indicative of high crystallinity. Reproduced from [93].*

Most distinctively, deep-UV photoluminescence and cathodoluminescence measurements show bright near-band-edge emission with pronounced excitonic character in the ~ 5.7–6.1 eV range (≈ 215–220 nm), including fine structure whose intensity and linewidths evolve with temperature. The absolute quantum yield of the near band edge emission at low temperature can approach that of classic direct-gap semiconductors, emphasizing both the strength of the exciton and the low nonradiative recombination landscape in HPHT grade crystals. Although the direct versus indirect band gap for bulk hBN has been debated in the literature, the consensus in high-quality HPHT material is of exceptionally bright excitonic luminescence in the deep UV, with defect-related series (often labelled S and D) that can be disentangled by excitation energy and temperature. Defined initially in pioneering single-crystal work, these optical features continue to serve as the practical standards for assessing material quality today [90, 95–101].

Impurity and defect mapping techniques have advanced to the point where intra-crystal homogeneity can be assessed directly. Secondary ion mass spectrometry (SIMS) on Ba-flux crystal shows oxygen and carbon frequently below ~10^{18} cm^{-3}, far-UV photoluminescence microscopy can visualize impurity domains and spatial variations in near-band-edge emission at micrometre scales, offering a way to screen crystals for regions with the most intrinsic response. These tools, most notably the far-UV PL microscope developed for HPHT crystals by Watanabe and Taniguchi, provide a powerful link between growth conditions, solvent purity and device-relevant optical homogeneity [91, 96].

The HPHT parameter space is now sufficiently mature that practical operating windows can be summarized with reasonable confidence. Ba–BN growth near 4.5–5.5 GPa and 1500–1650 °C balances transport against impurity control and remains a favoured route for benchmark crystals. Mg–B–N growth at ~3 GPa with temperatures up to ~1900 °C

accesses the $MgNB_9$ intermediate and tends to produce fast transport and larger thickness per run, albeit with a tighter tolerance to phase competition. Sr-based fluxes combine the low-impurity character associated with Ba–BN solvents with favourable growth kinetics, yielding millimetre scale, optically transparent crystals at ~1500 °C and 4.5 GPa. Continued refinements in thermal engineering, crucible design and pre-growth outgassing of consumables incrementally improve yield and uniformity, but they do not alter the fundamental constraint that press volume, and controllable thermal gradients preclude wafer-scale growth. [91–94]

For applications, HPHT crystals function in two complementary roles. First, they are the reference dielectric or encapsulation layers in van der Waals heterostructures, where their low roughness, chemical inertness, and wide gap improve the mobility and stability of proximate 2D semiconductors. Second, they enable deep-UV photonics testbeds, from electroluminescence and photocurrent generation demonstrations to single photon emitter studies that benefit from a well-controlled and low background host. The most persuasive argument for HPHT is thus not scale but quality, when a study requires the cleanest possible host lattice and the brightest possible deep-UV excitonic response, HPHT hBN is still the starting point. This fact also motivates the more scalable thin film methods to emulate HPHT's impurity budget and excitonic metrics, a theme that bridges naturally into the CVD family sections that follow [90, 96–101].

For clarity and reproducibility, we distil prior reports into a concise overview of representative HPHT process conditions and resulting materials. While details vary with press configuration and flux formulation, the table collates the operative ranges, characteristic sizes, and quality metrics that will anchor subsequent comparisons between HPHT benchmarks and thin-film objectives.

Table 2.2: *HPHT and Flux Routes for hBN Single-Crystal Growth.*

Solvent	**Pressure**	**Temperature**	**Dwell**	**Typical Size**
BA – BN ($Ba_3B_2N_4$)	4.5 – 5.5	1500 - 1650	2-12 hr	~0.5 – 3 mm [90-91]
Mg-B-N ($MgNB_9$)	~3	Up to 1900	1-2 hr	mm class [92-93]
Sr based nitride ($Sr_3B_2N_4$)	4.5	1500	-	~1.2 mm [94]
Atmospheric Pressure (Fe/Ni) High-T flux	~0	1400	-	Sub mm to mm [95-96]

Finally, it's important to note that purification of consumables shapes the defect landscape in HPHT growth. BN crucibles and nitride solvents should be pre-baked and handled under rigorously dry conditions so that oxygen and water remain below detection limits. Equally decisive is thermal field uniformity within the press: even modest gradients bias nucleation fronts and broaden the crystal size distribution. For reproducibility, reports should include the full thermodynamic path (pressure, temperature, dwell time, and cooling rate), solvent stoichiometry, seed use (present/absent), crystal yield, and post-growth cleaning/anneal protocols. Such reporting practices both enable replication and permit the thin-film sections that follow to make meaningful, comparisons to the HPHT benchmark [91–93, 96].

2.3.2 Chemical Vapor Deposition (CVD)

Whereas HPHT grows hBN by dissolving boron and nitrogen into a molten nitride flux and re-precipitating crystals at several-GPa conditions, CVD forms sp^2-BN in situ on a substrate from vapour precursors at elevated temperature and sub atmospheric to atmospheric pressure. Within the CVD family, metal-organic CVD (MOCVD is often termed MOVPE when epitaxial growth on crystalline templates is emphasised. It uses identical reactors and chemistries. In this thesis we treat MOCVD and MOVPE as a single sub-class of CVD rather than a distinct growth method. This distinction in the thermodynamic pathway of the two methods define the strengths and limitations of CVD relative to HPHT. HPHT delivers hBN with highest purity and deep-UV excitonic quality but only at millimetre scales. CVD sacrifices some of that perfection to reach wafer-scale continuity with reactor designs compatible with semiconductor manufacturing. CVD performance depends on total pressure, substrate temperature, precursor choice, partial pressures and growth time. In plasma or metal-organic variants, the activation scheme and gas-phase chemistry also govern nucleation density, domain orientation, layer number, and impurity uptake, and thus the optical figures of merit relative to HPHT [103–109,128–130].

In the low-pressure thermal regime typically used to maximise uniformity, CVD is run at ~ 0.1–2 Torr in hot wall quartz tubes with a stable isothermal zone of ~ 900–1100 °C. Copper and nickel foils remain the standard substrates because they reduce the effective barrier to BN formation. On Cu substrate, the very low bulk solubility of B and N suppresses through thickness growth, so deposition is mainly surface mediated and tends toward mono or few layer self-limited hBN film growth. Borazine ($B_3N_3H_6$) is preferred where carbon suppression is critical because it decomposes cleanly, ammonia borane (NH_3BH_3) is popular

for its practicality but must be dosed carefully to avoid polymeric residues, diborane with ammonia is the most reactive combination but requires stricter safety and flow control.

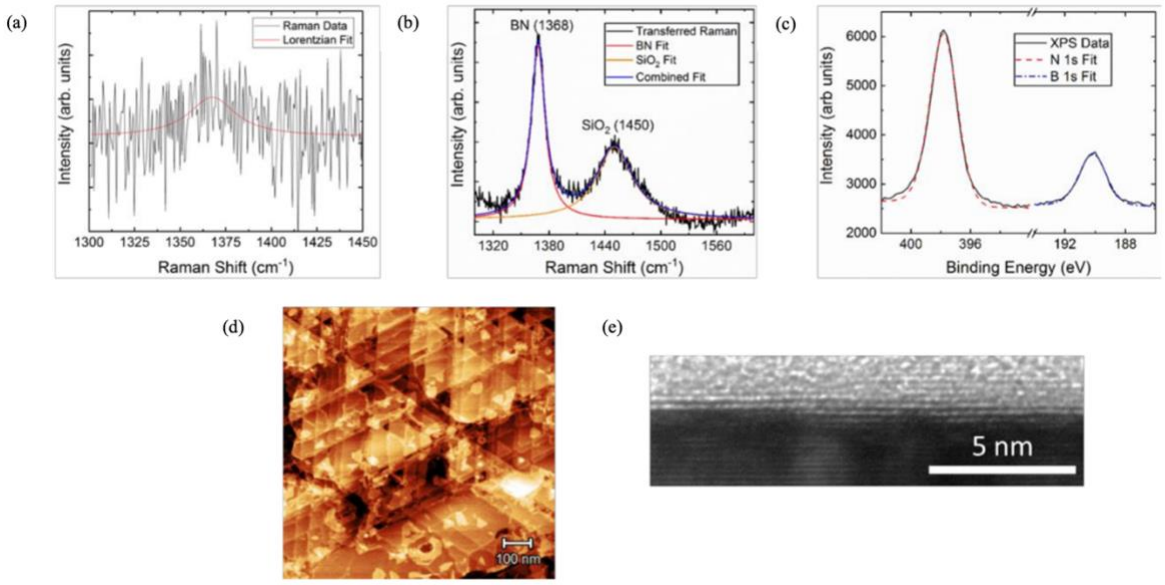

Figure 2.12: Structural and Chemical Characterization of CVD-Grown hBN Films. *(a) Raman spectrum of hBN (E_2g mode, Lorentzian fit) from films grown via CVD. (b) Raman of CVD-grown hBN after transfer to SiO_2, showing the BN peak (~1368 cm^{-1}) and SiO_2 contribution. (c) XPS confirming B–N bonding in CVD-grown films from fitted N 1s and B 1s peaks. (d) AFM image revealing layered morphology and terrace steps of the CVD-grown hBN. (e) Cross-sectional HRTEM showing a uniform few nm thick CVD-grown hBN layer. Reproduced by [197].*

Copper and nickel routinely deliver centimetre to wafer-scale coverage. Quality metrics are consistent with E_2g Raman mode sitting near 1366–1370 cm^{-1}, AFM reveals sub-nanometre terrace roughness, and dielectric breakdown fields are typically ~ 0.7–1.0 V nm^{-1}. Taken together, these numbers of bracket HPHT benchmarks when deep-UV excitonic PL and tunnelling-dielectric strength are used as comparators.

The main limiter is nucleation density. Lowering pressure suppresses gas-phase polymerisation that would otherwise create stray islands. Hydrogen co flow removes

polymeric intermediates before they foul terraces. On Cu(111) and Ni(111), staging the precursor dose biases step edge attachment and lateral growth, so single orientation domains become accessible rather than popping up spontaneously.

Once nucleation is tamed, wafer-scale uniformity follows reactor physics. A flat hot zone and a stable near surface boundary layer are decisive. Isothermal zones reduce thermal drift. Laminar flow steadies external mass transfer. Gentle, staged cool-downs limit wrinkle formation and intergranular contamination. In combination, these controls preserve monolayer continuity across the wafer and keep optical and electrical figures of merit within the target window [103–109,129,130].

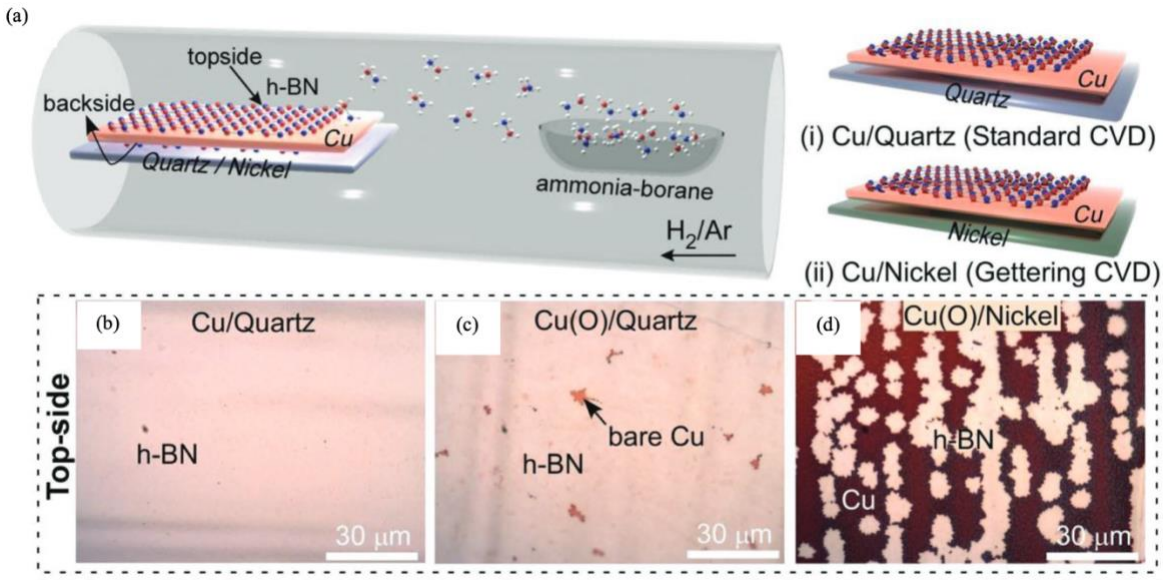

Figure 2.13: Comparison of Standard and Gettering MOCVD Growth of hBN on Cu. *(a) Schematic of hBN chemical vapor deposition (CVD) from ammonia–borane precursors on Cu films supported by either quartz or nickel substrates. (i) Standard CVD growth on Cu/quartz. (ii) Gettering-assisted CVD growth on Cu/nickel, where Ni beneath the Cu film acts as a B sink to promote more uniform hBN formation. (b–d) Optical microscopy images of hBN grown on (b) Cu/quartz, (c) oxidized Cu/quartz, and (d) Cu/nickel, demonstrating improved hBN coverage and reduced bare Cu regions under gettering conditions. Reproduced by [198].*

Unlike HPHT, where the output is a freestanding crystal, most thermal CVD films grown on metals must be integrated onto dielectric platforms. This makes transfer chemistry a first-order determinant of the final optical and electrical properties. Conventional polymer assisted wet transfer is robust but leaves organic residues and trapped oxides that elevate loss and quench near band edge excitons. Electrochemical delamination reduces surface oxides on the metal and limits incorporation of etchant by-products, dry or quasi dry transfer and oxygen assisted delamination further cut residual contamination and roll to roll handling enables large area stacks with less mechanical damage. The strongest reports now retain near band edge deep UV emission and keep leakage currents close to HPHT benchmarks after transfer. The practical takeaway is that for CVD, the benchmarked unit operation is growth plus transfer rather than growth in isolation [112–114,131–133]. Because transfer is still a liability for the most demanding optical and quantum devices, direct growth on dielectrics has moved from proof of concept to a practical alternative. The kinetic strategy is straightforward, depress supersaturation so that heterogeneous nucleation is rare. Activate the surface with oxygen plasma or with functional monolayers so adsorption and reaction proceed without a catalytic metal. In some recipes, insert a very thin catalytic interlayer to assist early nucleation and then remove it in situ so the final interface is all dielectric. On SiO_2, sapphire, and nitride substrates, direct CVD now reproduces the same Raman E_2g positions and linewidth trends seen after transfer, together with sub nanometre AFM roughness and ellipsometry control of thickness. These outcomes hold provided carbon and oxygen are suppressed throughout growth and cooldown, and any post growth anneal stays below the temperature at which point defect backgrounds proliferate [110,111,128,129].

When the substrate or device stack imposes a thermal budget below roughly 500–700 °C, plasma assistance allows hBN to be deposited at temperatures that thermal CVD cannot

reach without sacrificing continuity or stoichiometry. Microwave or inductively coupled plasmas activate borazine or ammonia borane at 300–500 °C. They create radical rich boundary layers that lower the apparent barrier for surface reactions. The advantages for back end of line integration and for flexible substrates are clear. The main risks are ion damage, formation of amorphous BN, and hydrogen driven amorphization. In practice, you can tune plasma density, ion energy, hydrogen fraction, and pressure to achieve continuous films. With the right window, the near band edge photoluminescence remains visible, and the Raman response falls at the values expected for crystalline hBN rather than amorphous BN. There are now credible demonstrations of on chip devices built with directly grown hBN at a few hundred degrees. This is a temperature regime that HPHT crystals and high temperature LPCVD cannot reach without putting the rest of the stack at risk [115–119,116–118].

At the high-temperature end of the CVD family, metal-organic CVD (MOCVD, also referred to as MOVPE in epitaxial contexts) replaces simple boron hydrides or cyclic precursors with TEB (triethyl-boron) or TMB (trimethyl-boron) and relies on NH_3 at ~1000–1200 °C and tens to hundreds of Torr. These reactors inherit decades of uniformity, metrology and safety discipline from GaN and AlN manufacturing and make it straightforward to insert hBN into the same process lines and even the same runs as III-nitride device layers. The dominant issues are carbon incorporation and stoichiometry across the wafer.

Both respond to higher hydrogen fractions in the carrier gas, tuning of the V/III ratio, pulsed delivery or growth interruptions that allow desorption of carbon-bearing fragments, and to flow-modulation epitaxy designed to encourage 2D completion. This yields wafer scale and selective area films on sapphire, Ni(111), and nitride substrates with smooth surfaces, lower carbon content relative to the baseline TEB or TMB recipes and deep UV

transparency consistent with the HPHT anchored optical benchmarks. Importantly, hBN can also be co grown with GaN/AlN when that simplifies an optoelectronic or high frequency device flow [120–125].

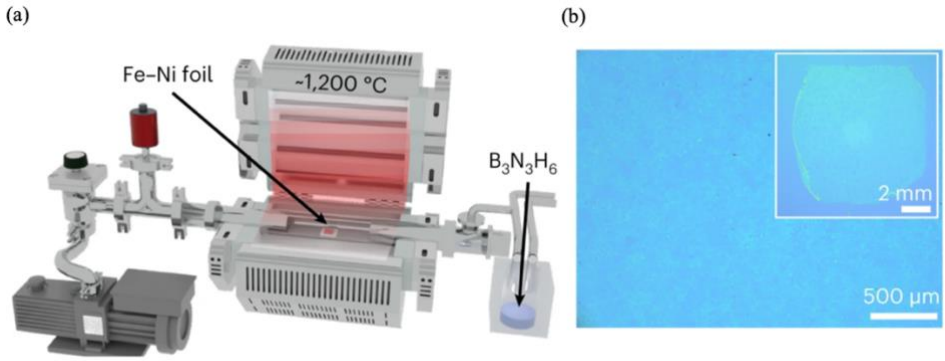

Figure 2.14: LPCVD Growth of Large-Area hBN Crystals on Fe–Ni Alloy Foils. *(a) Schematic of the high-temperature (~1200 °C) CVD setup using ammonia–borane ($B_3N_3H_6$) as the precursor and Fe–Ni alloy foil as the catalytic growth substrate. The precursor vapor is transported through the heated zone to promote hBN nucleation and layer growth. (b) Optical image of the resulting CVD-grown hBN, showing mm- scale single-crystal domains (inset: enlarged view displaying a ~2 mm hBN crystal). Reproduced by [199].*

A set of niche CVD methods rounds out the landscape and fills gaps that neither LPCVD nor metal-organic routes address efficiently. Atmospheric-pressure CVD is inexpensive and simple to implement but tends to sacrifice crystalline order unless the boundary layer and residence time are tuned with unusual care. Hot-wire CVD activates precursors catalytically at heated filaments and can lower the substrate temperature at the cost of filament management. On the other hand, Photo-CVD uses UV photons to drive dissociation in the boundary layer and enables localised or substrate-sparing activation, aerosol-assisted CVD introduces solution-borne precursors that would be hard to deliver in gas lines. Furthermore, microwave or laser-assisted CVD injects energy locally to nudge

kinetics without heating the entire wafer. These routes are particularly useful when you need patterned or local growth, unusual substrates such as Ge or steel and with tight local thermal budgets that standard hot-wall tubes cannot accommodate. They have not displaced LPCVD or MOCVD for wafer scale electronics, but they broaden the substrate palette and unlock growth windows that make specific device layouts feasible [108,128,129].

With all of the above on the table, the comparison to HPHT becomes straightforward and genuinely quantitative. If the target is the cleanest possible excitonic response in the 5.7–6.1 eV range and the lowest non-radiative background for quantum optics, HPHT remains the benchmark because it delivers single-crystal hBN with impurity levels at or below ~10^{18} cm^{-3} for oxygen and carbon and Raman E_2g peaks with the narrowest linewidths your instruments will measure. CVD can approach those optical signatures, especially when borazine is

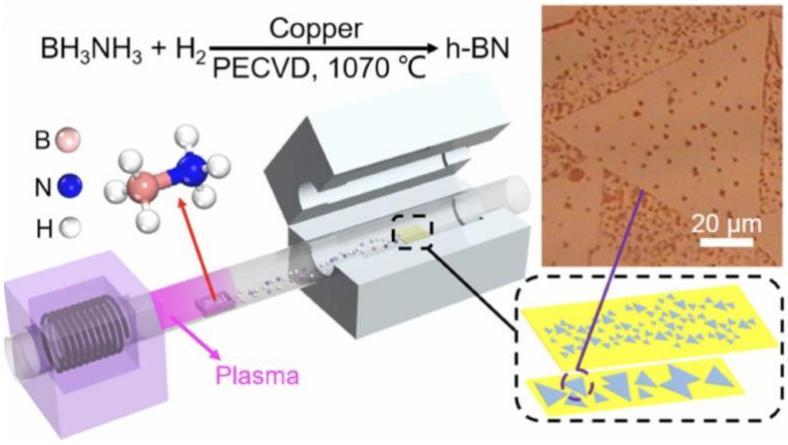

Figure 2.15: Plasma-Enhanced CVD (PECVD) Growth of Triangular hBN Domains on Copper. *Schematic of PECVD growth using ammonia–borane (BH_3NH_3) and H_2 precursors at ~1070 °C, where a plasma source assists precursor activation and promotes hBN nucleation on copper foil. The optical micrograph (right) shows triangular hBN domains with lateral dimensions on the order of tens of micrometres. Reproduced by [200].*

used, nucleation density is suppressed, cooling rates are gentle, and transfer is clean or avoided entirely by direct growth. What CVD adds that HPHT cannot is, lateral scale and process compatibility. CVD allows continuous coverage over centimetres to wafers, control over layer number in the 0.33–3 nm regime and direct placement on device dielectrics or on III-nitride platforms at temperatures compatible with the rest of a process flow.

Framed correctly, route selection is not a contest of superiority rather a process–device matching. When purity ceilings and excitonic coherence dominate, HPHT single crystals define the optical and dielectric reference. They minimise point-defect and impurity backgrounds. They also deliver the narrowest E_2g Raman linewidths and the cleanest excitonic emission. Size limits remain, but for van der Waals encapsulation and deep-UV emitters the material quality is decisive. For integrated photonics, surface passivation and back-end stacks, LPCVD and PECVD provide deterministic placement on dielectric wafers. LPCVD exploits diffusion limited, low supersaturation kinetics at 900–1100 °C.

PECVD introduces activated nitrogen and boron radicals at a few hundred degrees. Both routes accept controlled trade-offs in defect density, excitonic linewidth, and leakage current to achieve in situ integration. For nitride optoelectronics and high-frequency electronics, MOCVD or MOVPE embed hBN within existing GaN/AlN unit processes. They leverage V/III ratio control, hydrogen scavenging, and flow-modulated epitaxy. They also avoid ex situ transfer and thus resulting polymer residues, thereby lowering interface trap density and integration friction [103–125,128–133].

A single principle unifies the comparison. Every incremental improvement in nucleation control, precursor cleanliness, hydrogen management and thermal field uniformity in CVD must be benchmarked to HPHT optical and dielectric yardsticks. Use the E_2g position and FWHM as a crystallinity gauge. Use deep-UV excitonic PL as a measure of radiative

quality. Track leakage current density, breakdown field, and interface state density as device relevant metrics. Report domain orientation, layer-number dispersion, and carbon or oxygen incorporation to close the loop.

Table 2.3. *Summary of CVD variants for hBN showing operating windows, activation, precursors, substrates, film and layer control, transfer needs, recurrent issues, and indicative use cases, with key references.*

Defect Type	**LPCVD**	**PCVD**	**MOCVD/ MOVPE**
Pressure (Torr)	0.2 – 2	0.5 – 5	50 – 760
Temperature (°C)	900 – 1100	300 – 500	1000 – 1200
Activation	Thermal surface reaction, suppressed gas phase polymerisation	Plasma radicals & ions	Thermal decomposition with NH_3
Precursor	Borazine NH_3+ BH_3	Borazine NH_3+ BH_3	TEB or TMB NH_3
Substrate	Cu(111) Ni(111)	Si, SiO_2, Nitrides, Metals, Sapphire	Sapphire, SiC Ni(111)
Film Size	cm to wafer scale monolayer to few layers self-limited	Large area, layer control via plasma density	Wafer scale selective area films layer control
Transfer to Dielectric	Required for metal grown films	Not required when grown on dielectrics	Not required when grown on dielectrics
Limitations	C/ O contamination, wrinkles, grain boundaries	Ion damage Amorphous BN Non uniformity	C- incorporation Stoichiometry drift
Application	High crystallinity at wafer scale [103-109, 128-130]	Low – T integration flexible substrates [115-119]	Co- integration UV photonic stack [120-125]

These criteria allow a direct, quantitative assessment of how closely each growth route approaches the HPHT reference under realistic device constraints [103–125,128–133].

Table 2.3 summarises CVD variants for hBN by listing the operative ranges in pressure and temperature, the activation route, representative precursors, common substrates, film size and layer control, transfer requirements, recurrent issues, and indicative use cases. It is designed as a single-page reference to align process choice with device constraints and to benchmark each route against HPHT targets [103–125,128–133].

2.3.3 Molecular Beam Epitaxy (MBE)

Molecular beam epitaxy prioritises atomic scale control, growing hBN from elemental boron plus activated nitrogen under ultra-high vacuum so fluxes, stoichiometry, and interface abruptness can be tuned with high precision. In the clearest studies on c plane sapphire, high crystalline quality only appeared once the substrate temperature exceeded about 1600 °C. The boron beams equivalent pressure stayed very low, about 10^{-8} Torr. Under these high temperature, low flux conditions, in situ RHEED showed streaky patterns with 60° rotational symmetry and a fixed epitaxial relation $[11\bar{2}0]_{hBN} \parallel [1\bar{1}00]_{sapphire}$, ex-situ AFM revealed atomically terraced surfaces. At lower temperature or higher boron flux, films quickly became rough and polycrystalline, which establishes the high temperature, low flux corner as the practical growth window for epitaxial hBN on sapphire [134].

Because molecular nitrogen is inert at these temperatures on oxide surfaces, a radio frequency nitrogen plasma source is routinely used to supply activated nitrogen, which enables plasma assisted MBE at somewhat lower substrate temperature while preserving UHV cleanliness. In this configuration on graphitic templates or oxides, crystalline monolayer and few layer hBN has been reported at roughly 1380–1420 °C. AFM confirms

atomically flat terraces with coverage control and RHEED provides complementary verification. The mechanistic picture is consistent across tools. The boron flux must stay deliberately low to avoid amorphous BN. Active nitrogen must be sufficient to favour sp^2 bonding. If either condition is missed, disorder rises, and the Raman E_2g line broadens. Plasma assisted studies enlarge the usable kinetic window relative to the ultra-high temperature sapphire work, while retaining the core MBE advantages of clean interfaces and very low contamination [135–136].

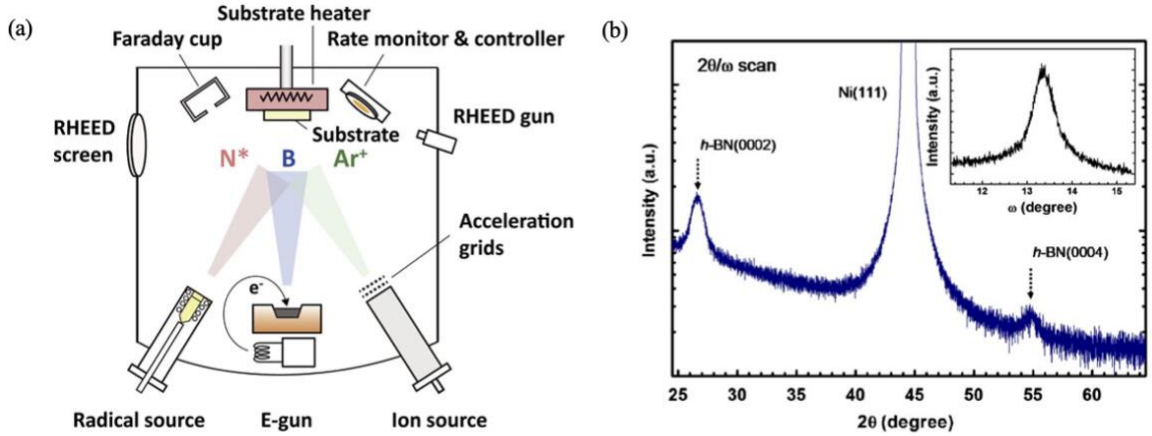

Figure 2.16: Molecular Beam Epitaxy (MBE) Growth and Structural Characterization of hBN. *(a) Schematic of the MBE growth chamber showing separate sources for B, activated N radicals, and Ar^+ ion assistance, along with substrate heating and in-situ RHEED monitoring used to control film growth. (b) XRD scan of MBE-grown hBN on Ni(111), showing the h-BN(0002) and hBN(0004) reflections consistent with layered crystallinity. Inset: ω-rocking curve of the h-BN(0002) peak indicating crystalline film quality. Reproduced by [201- 202].*

Researchers have mapped the growth window by varying substrate temperature and boron flux while keeping the nitrogen plasma power fixed. When the temperature climbs above about 1600 °C at a low boron flux, the in situ RHEED pattern changes from spotty to streaky. The in-plane alignment then locks to the sapphire lattice and post transfer AFM confirms atomically terraced surfaces. Raising the boron flux at a fixed temperature pushes

the film into a parasitic amorphous regime. BN clusters form near the surface faster than they crystallises on terraces. This split explains the early record. Lower temperature runs produced rough, turbostratic films. Later work at higher temperature recovered rotational alignment, van der Waals epitaxy, and deep ultraviolet transparency. The same studies show that deposition rates are slow. Lateral area is limited by the thermal design of UHV sources that operate above 1500 °C. As a result, the highest quality MBE hBN remains an academic platform for clean heterostructures rather than a wafer production route [134, 137].

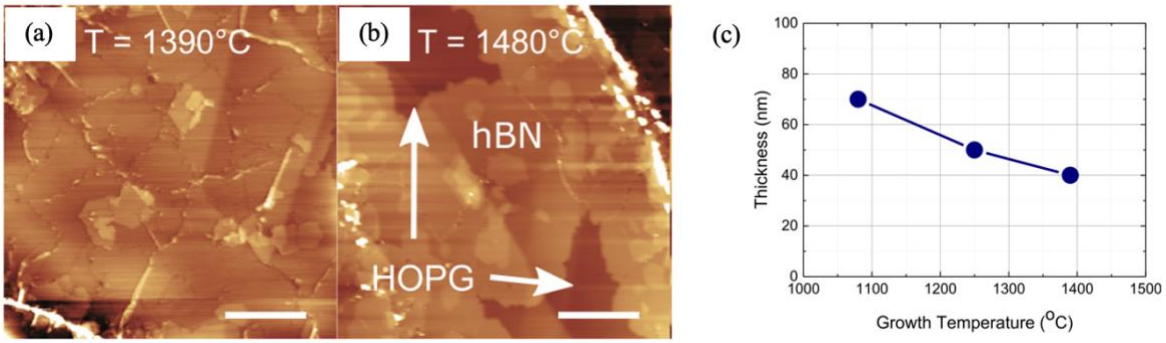

Figure 2.17: High-Temperature MBE Growth of hBN on HOPG and Thickness Control. *(a–b) AFM images of hBN films grown on highly oriented pyrolytic graphite (HOPG) at (a) 1390 °C and (b) 1480 °C, showing layered terrace morphology and step-flow growth behaviour at elevated temperature (scale bars: 500 nm). (c) Thickness of MBE-grown hBN as a function of growth temperature, demonstrating a decrease in film thickness with increasing substrate temperature due to enhanced surface re-evaporation and reduced sticking coefficient. Reproduced by [203- 204].*

Post growth thermal budgets and substrate choice further shape outcomes. On sapphire, a high temperature anneal after growth sharpens crystallinity and reduces mosaic spread. The Raman E_2g linewidth then narrows toward the crystalline benchmark near 1366 cm^{-1}. AFM shows hillocks that smooth into broader terraces. With 2D substrates, van der Waals epitaxy under plasma assistance relaxes lattice constraints, enabling growth at lower

temperature. The in-plane texture then mirrors the domain mosaic of the underlying graphite. Across both families, the UHV environment holds carbon and oxygen backgrounds to source purity and base pressure. As a result, MBE and plasma assisted MBE produce especially clean interfaces for stacks with TMDCs and nitrides [136, 138].

Device relevant metrics track these growth levers. High quality MBE films place the Raman E_2g mode near 1366 cm^{-1} with a reduced linewidth and AFM shows sub nm roughness on terraces. Deep UV response preserves the near band edge exciton when the high temperature, low flux window is respected. Because carrier gases are absent, interfacial contamination is minimal. This is valuable in van der Waals heterostructures where trapped residues often dominate scattering and non-radiative loss. On sapphire, characterisation shows fewer wrinkles with reduced hillock density. Both drop as growth temperature rises during deposition or during the post growth anneal. High resolution transmission electron microscopy (HRTEM) reveals ordered stacking. Spectroscopic signatures converge toward HPHT like benchmarks as the process approaches the ultra-high temperature limit [136].

From an integration view, the precision and cleanliness of MBE suit studies of interlayer coupling, single photon emitter formation, and low dimensional transport in encapsulated stacks. Costs include slow deposition, small substrates, and specialised thermal hardware. The method serves as the precision end member in this chapter. Choose MBE when the experiment needs UHV clean interfaces or atomic layer control. Choose a CVD class route when wafer level throughput or metal catalysed monolayers are the priority [136, 139].

2.3.4 Precipitation Growth

Precipitation growth yields large area hBN by dissolving boron and nitrogen into a catalytic metal at high temperature, then returning them to the surface during a controlled cooldown. Nickel and iron are the standard substrates because B and N are soluble at the growth temperature. Exposure to borazine or to ammonia borane loads the metal lattice. The subsequent cooldown drives surface supersaturation, nucleation, then coalescence. The clearest demonstration of this dissolve and segregate picture is on Fe foils. Slow cooling after borazine exposure produces centimetre scale multi-layer hBN.

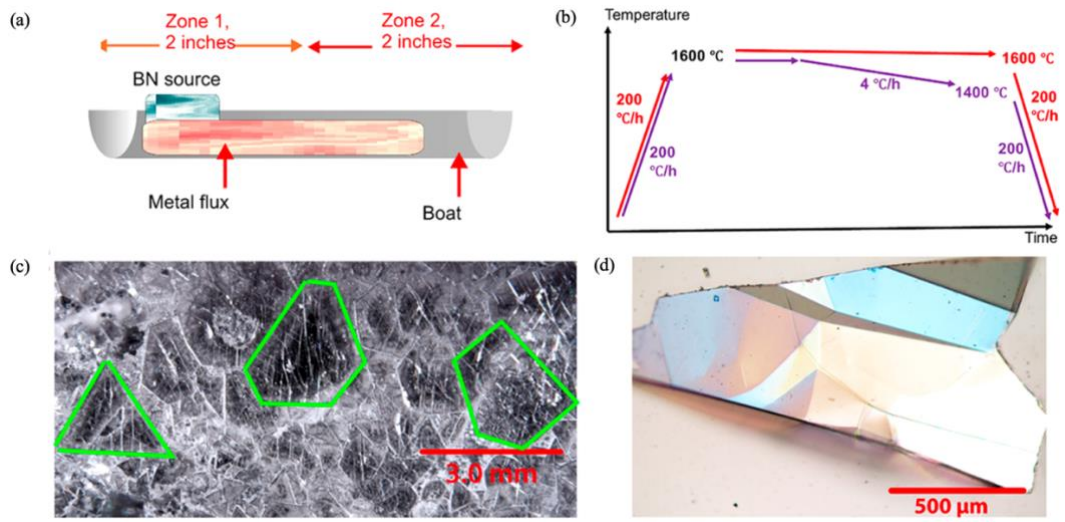

Figure 2.18: Atmospheric-Pressure High-Temperature Flux Growth of hBN Crystals. *(a) Schematic of the flux growth setup in a two-zone tube furnace, where a BN source reacts with a molten metal flux within a ceramic boat. (b) Temperature profile used for crystal growth, involving heating to 1600°C followed by controlled cooling to 1400 °C before re-heating and final cooldown. (c) Optical micrograph of flux-grown hBN platelets with lateral sizes on the mm scale (outlined in green). (d) High-magnification image showing smooth, faceted hBN crystal surfaces characteristic of layered growth. Reproduced by [205].*

Cathodoluminescence and Raman mapping show uniform optical quality across large areas. Mechanical testing reports a high Young's modulus consistent with well-ordered sp^2

BN. In these runs, precise monolayer control is difficult because the thick Fe reservoir feeds continued segregation during the ramp, so the natural outcome is few to many layers [141].

On nickel the behaviour is more tunable. The balance of boron to nitrogen solubilities, diffusion kinetics, and surface symmetry, especially on Ni(111), controls orientation as well as domain growth. Epitaxial alignment on Ni(111) yields larger single orientation domains and faster coalescence than polycrystalline foils. Selective area growth or enclosure geometries can localise nucleation to bias the outcome.

The same segregation mechanism that sets thickness can harm uniformity. If uptake of boron versus nitrogen differs across grains, precipitation becomes spatially non uniform during cooldown. The film then thickens unevenly unless the thermal ramp and the pre-exposure are tuned.

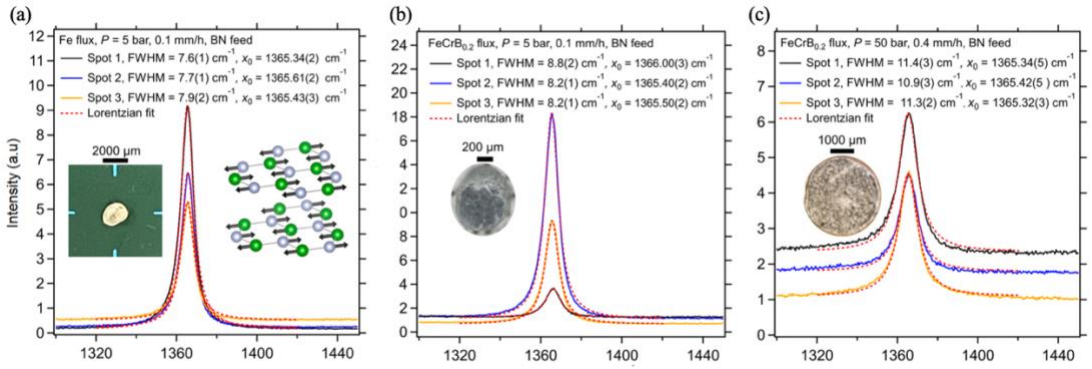

Figure 2.19: Raman Spectroscopy of Flux-Grown hBN Crystals Under Different Metal Flux Conditions. *(a) Raman spectra of hBN grown using Fe flux at 5 bar, showing a sharp E_2g mode near ~1365 cm^{-1} with FWHM values ~7.6–7.9 cm^{-1}, indicating high crystalline quality (inset: optical image of a mm-scale crystal). (b) Raman spectra of hBN grown using Fe–Cr–B_2O_3 flux at 5 bars, showing slightly broader E_2g peaks (FWHM ~8.2–8.8 cm^{-1}) and smaller crystal domain size (inset: optical image). (c) Raman spectra of hBN grown using Fe–Cr–B_2O_3 flux at 50 bar and higher BN feed rate, yielding further broadened peaks (FWHM ~11–12 cm^{-1}), consistent with increased disorder or stacking variations (inset: optical image of the corresponding crystal). Reproduced by [208].*

Recent mechanistic studies identify these pitfalls with clear causes, including solubility contrast, strong dependence on cooling rate, plus grain orientation effects. They also show that pre nitridation, Ni-Fe alloying, and staged cooldowns mitigate these issues [140, 142].

Theory and reactive molecular dynamics now visualise the atomic steps of segregation from molten nickel, offering a microscopic narrative that matches experiment. ReaxFF simulations show that nuclei form at the liquid metal to gas interface when activated nitrogen reacts with solvated boron at the surface. Boron nitrogen containing intermediates such as N-N-B or B-N-B then evolve toward stable sp^2 rings. Incorporation of small BN motifs into growing sheets is the rate limiting step. When the temperature rises above about ~1900 K, nascent sheets break more readily. Operation near the nickel melting point maximises net sheet formation. This atomic picture explains the macroscopic levers observed in the laboratory. Control the boron inventory during the high temperature exposure. Manage the cooldown to steer the supersaturation path. Use the microstructure, in particular grain size and orientation, to guide domain registry and coalescence. These points align with reported outcomes [143].

A natural question is whether segregation can deliver wafer scale single crystals rather than polycrystalline or highly textured films. A compelling pathway comes from liquid metal strategies, especially liquid copper. Cu has very low bulk solubility for boron and for nitrogen, and it is better known as a surface mediated CVD catalyst. Running Cu in the liquid state creates an atomically flat, defect poor template. It also enables precise control of local precursor delivery, with controlled step flow during cooldown. Recent reports show wafer scale single crystalline hBN with tunable thickness on liquid Cu. This captures the idea of oriented precipitation without deep bulk dissolution. In parallel, process reviews map routes to single crystals. They emphasise enclosure geometries, Cu(111) orientation control, and confined space flux throttling to suppress random nucleation. They also enforce

unidirectional domain stitching to move from laboratory foils to industrial scale single crystals [144–145].

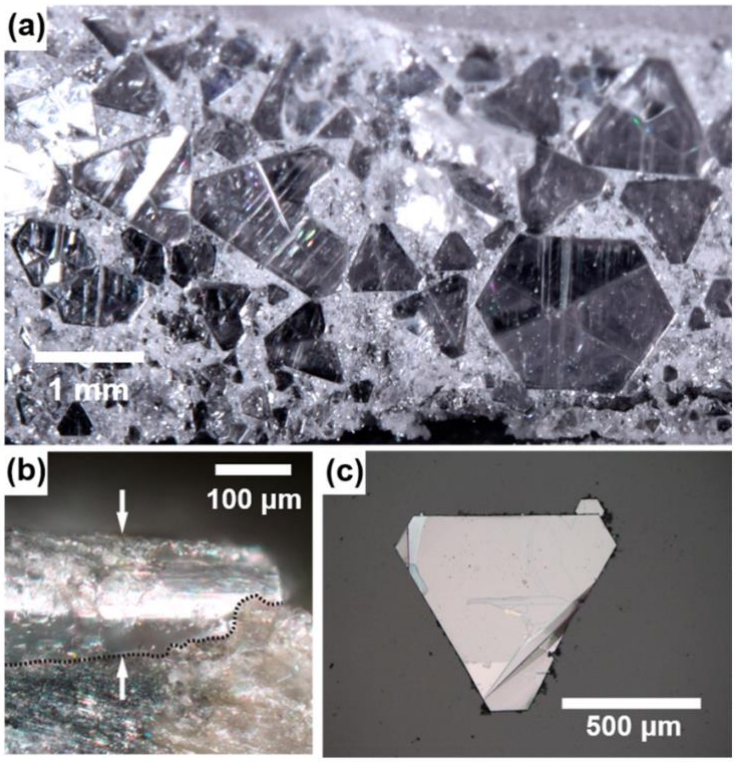

Figure 2.20: Morphology and Crystal Habit of Flux-Grown hBN. *(a) Optical image of a bulk flux-grown hBN batch, showing a distribution of faceted platelet crystals with lateral dimensions from sub-mm to mm scale. (b) Cross-section view of a crystal embedded in the flux matrix, with the layered structure visible along the cleavage direction (dotted line). (c) Isolated single hBN platelet exhibiting characteristic triangular/hexagonal morphology and smooth basal surfaces (lateral size ~500 µm). Reproduced by [207].*

Quality metrics and integration constraints follow from this growth physics. Raman spectroscopy remains the fast structural yardstick. High quality segregation grown films place the E_2g mode near 1366 cm^{-1}. The linewidth narrows as stacking faults fall, while turbostratic admixture declines. Cathodoluminescence maps highlight near band edge uniformity over centimetre scales, with impurity domains resolved. AFM confirms terrace

level flatness once wrinkles from thermal contraction are minimised. The chief integration challenge is the transfer step, which is shared with LPCVD on metals. Polymer residues or trapped oxides can spoil dielectric performance if wet transfer is not controlled. Electrochemical delamination lowers residue. Dry stamps or quasi dry lamination do the same and preserve deep UV optical signatures. Treat these steps as part of the precipitation process flow when optical loss or breakdown field matters. Recent reviews compare vapour phase routes with segregation routes. They find that segregation excels when thickness beyond a monolayer is needed over large areas. They also show that direct growth on dielectrics is preferred when transfer risk dominates [139–141].

2.3.5 Pulsed Laser Deposition (PLD)

PLD uses short laser pulses to ablate a dense BN target. Each pulse lifts a thin layer of material into a hot plume. The plume carries B, N and BN fragments to a heated substrate where they recombine and crystallise. The main controls are laser fluence around 1–3 J cm^{-2}, repetition rate between 1 and 50 Hz, background gas at 10^{-6} ×10^{-2} Torr of nitrogen with or without a small fraction of hydrogen, and substrate temperature near 600–1000 °C. Together these settings tune the energy of arriving species, surface diffusion, and the final film stoichiometry. The appeal is simple. Composition transfers well from the target to the film. Switching materials is as easy as rotating to a new target. Masks or simple shadow plates give you direct patterning. The costs are also well known. Particles can be ejected from the target and land as “droplets.” The plume is directional and can give non-uniform coverage on large wafers. Energetic species can build stress if cooling and pulse timing are not controlled.[146–148]

For hBN the target is usually a dense hexagonal BN ceramic. Nitrogen is used as the ambient to replenish N and to scatter the plume so it spreads more evenly. Adding a small fraction of hydrogen can help remove carbon-bearing fragments when present, but too much hydrogen will start to etch weakly bound BN from the growing surface.[149] Substrates run hotter when crystallinity is the priority. Temperatures at or above 800–900 °C, combined with a modest nitrogen pressure near 10^{-3}–10^{-2} Torr, raise adatom mobility and suppress amorphous BN. After deposition, a short anneal in nitrogen or ammonia tightens the Raman line and smooths the near-band-edge optical response. [149, 151, 152] Laser fluence is kept only slightly above the ablation threshold. That keeps the plume stable while limiting the shock that throws micron-scale fragments from the target. Driving the fluence higher does not improve crystallinity for hBN. It raises roughness and defect counts and it increases droplet density.[146–148]

Substrates matter. On sapphire and on Ni(111) the films can grow with in-plane texture when the surface is hot, and the nitrogen pressure is tuned. The Raman E_2g then sits near 1366 cm^{-1} with a narrower FWHM than room-temperature growth. On SiO_2/Si at 700 °C or below, the films often turn turbostratic or amorphous because the surface diffusion length is too short for ordered sp^2 bonding.[149, 151, 152] These trends track what you would expect from simple diffusion arguments: higher temperature and a small amount of scattering in the boundary layer give atoms enough time to find low-energy sites before the next pulse arrives. There are also reports of room-temperature PLD producing ordered h-BN nanosheets under special conditions.

These emphasise very clean targets, tight fluence control, and post-treatments to heal disorder.[150] They are useful to note, but the most reproducible route to crystalline hBN remains hot-substrate growth. Thickness control is one of the strengths of PLD. The growth

per pulse can be calibrated once by ellipsometry, X-ray reflectivity, or AFM step measurements. After that you count pulses to set thickness. Few-layer films through tens of nanometres are routine. Uniformity on chips and small coupons is very good because the plume is

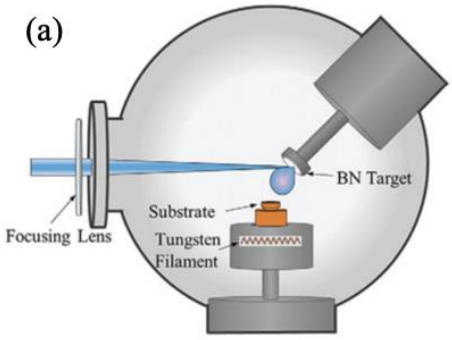

Figure 2.21: Thin-Film hBN Growth via PLD and Plasma-Assisted CVD. *(a) Schematic of pulsed laser deposition (PLD) of hBN, where a focused laser beam ablates a BN target and deposits material onto a heated substrate. Reproduced from [209].*

intense and well defined over a few centimetres. Scaling to 2 to 6-inch wafers is harder. The angular spread of the plume and shadowing from fixtures create radial gradients. Substrate rotation helps. So does moving the substrate slightly off the plume axis so the steep intensity peak is averaged out across the wafer. Increasing the target-to-substrate distance and adding a little background nitrogen introduce scattering that softens the profile at the cost of a small drop-in rate. [146–148, 154] The familiar particulate problem can be pushed down with several simple practices. Keep the fluence near threshold. Use a longer target-to-substrate distance. Add moderate nitrogen so heavy fragments slow and settle. Use off-axis geometries so any droplets travel past the wafer rather than straight into it. Raster and rotate the target so the beam never digs a deep crater that would spit debris.[146–148] Taken together these measures shift the defect mode from visible droplets to sub-100 nm particles that are sparse enough to be irrelevant for most dielectric uses.

The time structure of PLD can be used to your advantage. The off-time between pulses is a built-in “interrupt” that lets the surface relax. When the repetition rate is moderate, weakly bound fragments can desorb before the next burst of material lands. This is close in spirit to what hydrogen interrupts do in metal-organic CVD. Here it happens naturally from the pulsed supply. If the goal is a very smooth interface for tunnelling or for passivation, you can lengthen the off-time slightly or raise the substrate temperature a few degrees so step edges smooth before the next plume arrives. If stress is building, you can insert short cooling dwells every few thousand pulses. The result is a flatter stress-thickness curve and fewer wrinkles in the final film.

Gas handling and base vacuum deserve a short note. Oxygen and water in the chamber will react with hot BN fragments and with the target surface between pulses. That dulls the target and introduces B–O and N–O bonds that broaden the Raman response. A clean base pressure before back-filling with nitrogen is therefore important. Pre-ablation is also standard practice. You fire a few hundred pulses onto a stationary shutter. This cleans the target face and stabilises the plume before you expose the substrate. During the run, keep the target moving. A slow spiral raster with rotation spreads heat and wear. That holds the ablation threshold steady, which holds the plume composition steady.

Film composition and bonding are best checked with a small, fixed set of measurements. The Raman E_2g position and its FWHM give a quick readout of crystallinity. XPS with C1s, B1s and N1s shows stoichiometry and whether any carbonaceous fragments have been trapped. AFM provides terrace roughness and a sense of particulate density. For dielectric uses, a simple leakage-field sweep on metal–insulator–metal stacks give a first filter for defects and pinholes. Deep-UV photoluminescence completes the picture by tracking the near-band-edge exciton and the most common defect bands. These metrics make

it easy to compare PLD outcomes to HPHT single crystals and to CVD films and to decide whether the film belongs in the device flow. [146, 149, 151–154]

The practical recipe that emerges from published work is consistent. Keep the fluence just above the ablation threshold. Use nitrogen at 10^{-3}–10^{-2} Torr so the plume spreads without quenching. Hold the substrate between about 850 and 1000 °C when the substrate allows it. Rotate the substrate and, if the tool permits, add a gentle wobble to average out the plume. Place the wafer slightly off axis to smooth the profile.

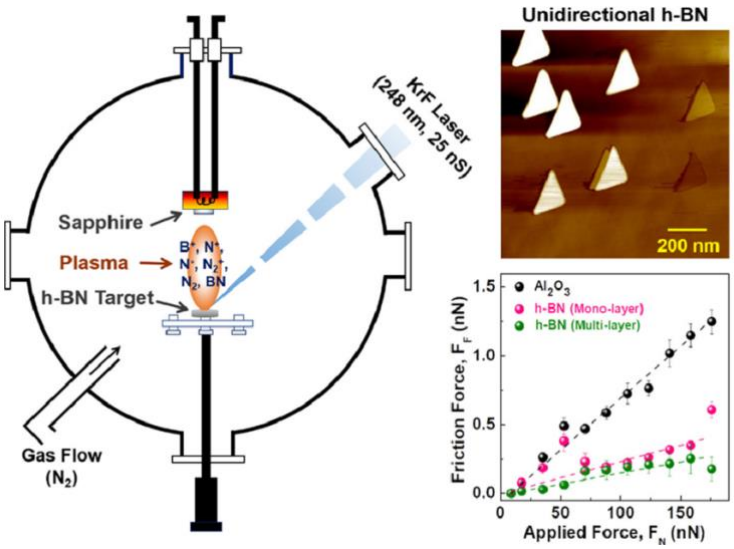

Figure 2.22: Pulsed Laser Deposition (PLD) Growth of Unidirectional hBN. *Schematic of PLD growth of hBN using a KrF excimer laser (248 nm, ~25 ns pulses) ablating an hBN target in a nitrogen environment, forming epitaxially aligned hBN domains on sapphire substrates. AFM image (top right) shows triangular, unidirectionally oriented mono- and few-layer hBN flakes (scale bar: 200 nm). The friction–force measurements (bottom right) demonstrate reduced friction for monolayer and multilayer hBN compared to Al_2O_3, highlighting hBN's lubricating and low-shear characteristics at the nanoscale. Reproduced from [210].*

After growth, anneal in nitrogen or in a small flow of ammonia to sharpen the Raman line and reduce shallow defects. For few-layer control, calibrate growth per pulse on the same

day and at the same nitrogen pressure you will use for the device run. Then add short cooling dwells between blocks of pulses to reduce stress and to avoid wrinkling during cooldown.

Integration cases show where PLD is most useful. On sapphire, direct PLD of hBN has produced optoelectronic-grade layers and deep-UV detectors without any transfer step. On diamond, PLD has been used to add BN dielectrics to ultra-wide-bandgap stacks, which opens routes to high-power and high-temperature devices. In nitride lines the trade-off is more subtle. If uniformity across 4–6 inch wafers and co-growth with GaN or AlN in the same run are mandatory, MOCVD or MOVPE is the simpler choice. If a transfer-free dielectric or barrier is needed on a crystalline dielectric at intermediate temperature, PLD fits well. It is also attractive when you need to switch compositions quickly for a heterostructure, for example BN/AlN/oxide stacks for passivation or for tunnelling. [149, 151, 154]

HPHT remains the quality ceiling for deep-UV excitonic response and for the narrowest Raman linewidths. LPCVD and PECVD give you large-area coverage on dielectrics with tight control over layer count and transfer-free integration at lower temperature, at the cost of somewhat broader optical lines. MOCVD or MOVPE give you wafer-scale uniformity, timing control, and direct insertion into III-nitride production. PLD fills the gap between these. It is clean, tunable, and fast to iterate. It delivers stoichiometric sp^2-BN without polymers or wet transfer. The main risks are particles and large-area uniformity, both of which can be managed to acceptable levels for many dielectric and passivation roles.[146–154]

Putting that all together, a short, workable starting point for most hBN PLD runs is: dense BN target; base vacuum, then nitrogen at about 10^{-3}–10^{-2} Torr; fluence near threshold with a well-focused spot; target rotation and raster; substrate at 850–1000 °C where the stack allows; off-axis placement with rotation; a brief nitrogen or ammonia anneal; and routine

checks of Raman, XPS, AFM, and simple leakage tests. If carbon shows up in XPS, add a little hydrogen to the nitrogen. If droplets appear, lower fluence and increase distance. If the film is under-dense or amorphous on SiO_2/Si, raise the temperature or accept a slightly thicker film where the extra thickness buys better order. With these levers in place, PLD provides a reliable, transfer-free route to clean hBN films that sit comfortably in the wider process map built around HPHT and CVD.[146, 149, 151–154]

2.4 Microscopy

2.4.1 Confocal Microscopy

Confocal microscopy is widely regarded as a critical technique in nanophotonics, particularly for analysing and characterising the emission features of hexagonal boron nitride (hBN) and its associated single-photon emitters (SPEs).

Unlike standard optical microscopes, which illuminate an entire sample region, the confocal setup directs a focused laser beam onto a single point of the surface through high-precision optics. This selective illumination allows specific regions of interest to be probed with significantly enhanced spatial resolution .[157]

In practice, one of the most important aspects of confocal microscopy is the ability to distinguish between the emission signal and the excitation source. This is typically achieved using dichroic mirrors in combination with optical filters, which transmit the emitted photons while blocking the excitation wavelength. In this way, background signals such as scattered light or noise are effectively suppressed, improving both the clarity and the specificity of the collected data.[158] A further defining feature of the confocal approach is the use of a pinhole aperture in the detection path, which may be incorporated through optical fibres or free-space optics. The pinhole operates as a spatial filter, ensuring that only light originating directly

from the focal spot is passed to the detector. This markedly enhances image sharpness and the overall signal-to-noise ratio.[159]

The resolution achievable with a confocal microscope depends on several parameters, primarily the numerical aperture (NA) of the objective lens and the wavelength of the excitation source. High-NA optics together with shorter excitation wavelengths yield finer resolution, making it possible to resolve very small details across the surface of interest. [160] For imaging and mapping, two scanning approaches are typically employed. The first is sample-stage scanning, where the specimen is moved in precise x, y, and sometimes z directions with piezoelectric stages while the optical system is kept fixed. The second is beam-scanning, where the laser beam is moved across the sample surface using rapidly driven scanning mirrors, often in a 4f optical configuration. These methods provide the ability to construct high-quality photoluminescence maps and to pinpoint the precise locations of emission centres within the sample. [161] In summary, confocal microscopy combines advanced optical filtering, precision scanning, and diffraction-limited resolution to deliver detailed spatial analysis of hBN SPEs, thereby playing an essential role in current nanophotonics and quantum technology research. [162]

2.4.2 Scanning Electron Microscopy

Scanning electron microscopy (SEM) is another widely used and powerful imaging technique, employed to produce highly magnified views of a material's surface structure by scanning it with a finely focused beam of electrons. Unlike conventional optical microscopy, where photons are used for imaging, SEM relies on the generation of signals produced when incident electrons interact with atoms at the surface of the specimen. These signals include

secondary electrons, backscattered electrons, and characteristic X-rays, each providing complementary information about surface morphology, composition, and microstructural features. With magnifications that can extend up to 300,000 X, SEM is particularly well suited to analysing materials such as hBN at the nanoscale.[163]

The general principle of SEM involves rastering a tightly focused electron beam across the sample surface. As the beam strikes the material, electrons from the sample are emitted and detected, generating a signal which is converted into image intensity. Secondary electron detection is used to produce detailed images of surface topography with high spatial resolution.[164] Through adjustments of the beam conditions, the accelerating voltage, and the choice of detectors, SEM can also be configured to produce three-dimensional reconstructions and highlight compositional differences across the specimen.

SEM systems can be operated in several different modes to suit a wide range of materials. For instance, variable-pressure or environmental SEM allows imaging of non-conductive or hydrated specimens that would otherwise be challenging under standard vacuum conditions. Nonetheless, SEM does have limitations: non-conducting samples are prone to surface charging effects, which distort the image, and therefore conductive coatings are often required. Despite these challenges, SEM remains a core tool in materials science, engineering, and nanotechnology, as it delivers high-resolution and versatile imaging that is essential for structural investigations.[165]

2.4.3 Atomic Force Microscopy

Atomic force microscopy (AFM) provides another pathway to nanoscale imaging, offering topographical information with resolution down to the atomic level. Unlike electron-

or photon-based microscopy, AFM employs a sharp probe tip mounted on a flexible cantilever to physically scan the surface of the material. As the tip moves across the surface, short-range atomic forces cause deflections of the cantilever. These deflections are recorded and converted into data that can be rendered into highly detailed three-dimensional maps of the surface. [166]

The technique works based on maintaining a consistent interaction force between the tip and the surface during scanning. This is achieved using a feedback loop that constantly adjusts the cantilever height to keep the interaction force steady. A laser beam reflected from the rear side of the cantilever onto a photodetector tracks these movements, with positional changes of the reflected spot translating directly into height data. [167] AFM can be operated in multiple modes. Contact mode involves continuous physical contact with the surface, tapping mode introduces periodic contact through oscillation of the cantilever, and non-contact mode measures the forces without touching the surface at all. Each configuration has advantages depending on whether delicate, hard, or soft samples are being analysed. [168]

AFM offers several notable advantages over electron-based techniques. It can be applied directly to non-conductive samples without requiring coatings, and it can operate in a variety of environments, including ambient air, liquid solutions, or vacuum chambers. In addition to simple topography, AFM can measure local material properties such as stiffness, adhesion, and electrical conductivity, offering a richer dataset than imaging alone. Its drawbacks include slower scanning speeds compared to SEM and gradual tip wear, which can degrade resolution. Nevertheless, AFM continues to be one of the most versatile and reliable nanoscale characterisation techniques, and for materials such as hBN it provides valuable insights into both structure and functional behaviour. [169]

2.4.4 Raman Spectroscopy

Raman Spectroscopy has become one of the most widely applied tools for investigating the vibrational and structural properties of hexagonal boron nitride (hBN). The method is based on the inelastic scattering of monochromatic light, usually from a laser, where the incident photons interact with the lattice vibrations (phonons) of the material and are re-emitted with a characteristic energy shift. This shift provides a fingerprint of the vibrational modes present in the crystal, allowing information to be extracted about structure, composition, and the presence of disorder. [170]

For hBN, the Raman spectrum is dominated by a strong E_2g phonon mode located at approximately 1366 cm^{-1}. The position, intensity, and linewidth of this mode are widely used as indicators of the film's crystallinity and strain. A narrow, sharp peak generally corresponds to highly ordered, defect-free material, whereas broadening of the peak or a measurable shift in its position can suggest strain, disorder, or variations in the stacking arrangement. [171] In few-layer and monolayer hBN, subtle differences in the Raman features can also provide useful information about layer number and interlayer coupling, making Raman a convenient method for thickness verification, particularly when compared with complementary techniques such as atomic force microscopy or transmission electron microscopy. [172]

Another strength of Raman spectroscopy lies in its ability to be performed in mapping mode. By collecting spectra across an extended region of a sample, spatially resolved maps can be generated that reveal local variations in strain, grain boundaries, or defect concentrations. This is especially relevant for large-area films grown by chemical vapour deposition or precipitation methods, where film uniformity is critical for device applications.

[173] More advanced configurations such as polarisation-resolved Raman or tip-enhanced Raman spectroscopy (TERS) provide even higher sensitivity, enabling nanoscale investigations of anisotropy and local vibrational behaviour. [174]

Raman is also non-destructive and can be carried out under ambient conditions, which makes it suitable for repeated measurements or even in situ monitoring of growth processes. For example, researchers have used in situ Raman to track crystallisation during CVD growth, gaining insight into kinetics and defect formation. However, the technique is not without its limitations. Raman is relatively insensitive to very low defect concentrations, and fluorescence background signals from substrates or impurities can obscure weak features of interest. Even so, the ability to provide fast, contactless feedback on material quality means it remains an indispensable characterisation tool for hBN. [175]

In recent years, Raman spectroscopy has continued to evolve, with improvements in instrumentation, laser stability, and detector sensitivity broadening its usefulness. When combined with other characterisation methods such as confocal microscopy, AFM, or electron microscopy, Raman adds an essential spectroscopic dimension that supports comprehensive analysis of hBN films. Taken together, these advances ensure Raman will remain at the forefront of hBN characterisation, particularly in applications where crystallinity, thickness, and strain uniformity are critical to device performance. [176]

3

Hexagonal Boron Nitride (hBN) growth via LPCVD

Hexagonal boron nitride (hBN) is a two-dimensional layered crystal that has been studied for well over a century, but only more recently has its broader potential been recognised. It differs markedly from graphene, its more famous structural cousin, in that hBN is an electrical insulator with a wide bandgap of around 6 eV. The crystal is built from sheets of boron and nitrogen atoms arranged in a hexagonal lattice, where each layer is held together by strong covalent bonds in-plane but connected to neighbouring layers only through weak van der Waals forces. This combination allows individual layers, or a few stacked layers, to be isolated without sacrificing stability. Early interest in hBN was linked to its unusual resilience: the material is chemically inert, withstands very high temperatures and pressures, and under extreme conditions can transform into cubic (c-BN) or wurtzite (w-BN) phases. These high-pressure phases approach diamond in hardness and thermal resistance, which has long made boron nitride a practical substitute for diamond in coatings and industrial tools.

More recently, the layered form of hBN has drawn attention in electronics and quantum photonics, where its insulating behaviour and defect-related optical properties make it an attractive platform for new device technologies. [32, 33, 40, 43]

This chapter explores the controlled synthesis of hBN films using Low Pressure Chemical Vapor Deposition (LPCVD), with an emphasis on how growth conditions influence both the structural quality of the films and the incorporation of optically active defects that function as single-photon emitters (SPEs). The experimental program was designed to systematically vary individual growth parameters to establish a more reliable understanding of their role in defect incorporation. Specifically, three sets of experiments were performed: growth temperature variation, growth duration studies, and controlled modification of heating and cooling rates within the furnace. Each experiment successfully incorporated SPEs into the hBN lattice, but the quality, stability, and density of the emitters differed under each condition .

The second part of the chapter investigates spatial variations in growth within the LPCVD furnace. Because the adsorption of precursor gases and the local microenvironment differ along the furnace length, spatial dependence was expected to affect both film quality and defect incorporation. By transferring and characterising hBN films from different furnace positions, this study highlights how variations in local growth kinetics directly influenced the spectral properties and emission stability of SPEs. Such a spatial analysis provides essential insights into the growth process, offering guidance for developing methodologies that enable uniform SPE incorporation across large-area films .

3.1 Abstract

Hexagonal boron nitride (hBN) grown by low-pressure chemical vapour deposition (LPCVD) is a promising host for room-temperature single-photon emitters (SPEs), but the relationships between growth conditions, lattice quality and emitter properties remain incompletely mapped. This chapter presents a systematic study that (i) varies growth temperature, duration and thermal ramp rates, (ii) quantifies position-dependent growth within the tube furnace, and (iii) explores homoepitaxial deposition on exfoliated hBN. Raman/FTIR spectroscopy, AFM, SEM and wide-field/confocal photoluminescence (PL) with second-order correlation were used to correlate crystalline quality with emitter statistics.

We identify a narrow thermal window around 1060 °C that minimises Raman E_2g linewidths and yields high-purity emission; growth durations of 20–30 min maximises Debye–Waller factors while avoiding spectral crowding; and faster ramps (8–10 °C min^{-1}) induce a blue-shift in both Raman and ZPL distributions consistent with compressive strain that stabilises emission. Spatial mapping across the furnace shows that upstream positions—balanced precursor flux and H_2 chemistry—produce sharper Raman peaks, higher emitter densities and lower $g^2(0)$, whereas downstream depletion degrades both crystallinity and emission quality. Finally, preliminary homoepitaxy suggests that ordered templates can host new layers with optically active defects under tuned conditions. Together, these results convert qualitative growth "rules of thumb" into quantitative guidance for scalable, wafer-compatible hBN with reproducible, bright single-photon emission suitable for integrated quantum photonics.

3.2 hBN Growth- via LPCVD under varying conditions

3.2.1 Introduction

This chapter examines the synthesis of hexagonal boron nitride (hBN) thin films grown using low-pressure chemical vapour deposition (LPCVD). The central objective of this study is to identify growth conditions that simultaneously produce high-quality crystalline films and allow for the controlled incorporation of single-photon emitters (SPEs). By carefully varying growth parameters and assessing their impact on both the host film and the resulting emission centres, the work aims to establish a reproducible pathway for generating stable and bright quantum emitters within hBN. [32, 33, 40, 43, 94, 177]

To achieve this, a series of systematic "parameter sweep" experiments were carried out, in which one growth condition was adjusted at a time while all others were kept constant. The parameters considered included growth temperature, duration, and the heating and cooling rates of the furnace. After growth, the hBN films were transferred to SiO_2 substrates, enabling structural and optical characterisation of both the films themselves and the incorporated SPEs. [178, 179]

Temperature proved to be a particularly critical factor. The growth window explored ranged from 1000 °C up to 1080 °C, chosen with reference to the melting point of the copper substrate (1083 °C). Within this narrow range, subtle differences in temperature strongly influenced both film crystallinity and the density of defect-related emitters. While higher temperatures generally improved long-range order, they also altered the likelihood of generating optically active point defects. One of the challenges addressed here was therefore

to balance improved crystal quality with the deliberate introduction of quantum emitters. [94, 177–179]

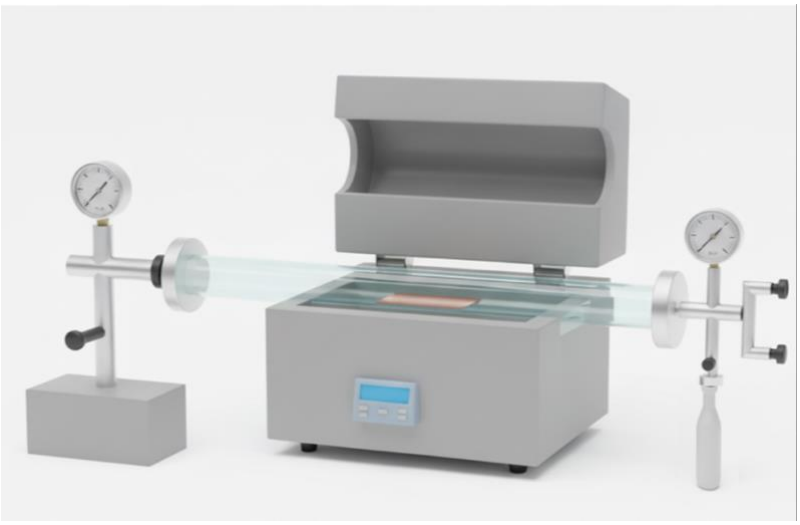

Figure 3.1: Schematic of the LPCVD horizontal tube furnace used for hBN growth. *A quartz tube runs through a clamshell resistive heater; a Cu foil/substrate on a quartz boat is positioned at the centre of hot-zone.* ***Right:*** *upstream gas inlet with flow control and pressure gauge.* ***Left:*** *downstream throttle/pressure gauge leading to the vacuum line. During growth, precursor vapour is transported by carrier gas through the tube at low pressure.*

Growth time was also investigated as a means of controlling film thickness. Previous studies suggest that hBN tends to favour lateral, in-plane growth on copper rather than vertical layer-by-layer extension. [180] As a result, once the initial nucleation stage is complete, the rate of thickness increase declines markedly. In this work, the duration of growth was varied from 10 to 40 minutes to explore its impact on film thickness and the corresponding optical behaviour of the defects. Although pressure is known to affect the number of hBN layers, equipment limitations restricted this study to time-dependent variations. [179, 181]

In addition to temperature and time, the rates of heating and cooling were found to significantly influence the microstructure of the films. Rapid temperature ramps often led to

local stress and non-equilibrium conditions, which increased the likelihood of non-uniform defect formation and degraded overall crystal quality. By contrast, slower cooling rates provided a more controlled environment, favouring uniform defect incorporation while reducing the appearance of unwanted structural irregularities. [178, 140, 141]

In summary, this chapter presents a systematic exploration of LPCVD growth conditions for hBN, focusing on (i) parameter sweeps (temperature, duration, thermal ramps) and (ii) positional dependence inside the tube furnace. The findings define growth strategies that improve the reproducibility and optical quality of single-photon emitter generation in hBN, supporting its use as a scalable platform for quantum photonic devices. [32, 33, 43, 94, 137–141]

3.2.2 Methodology

Copper foils with a thickness of 0.25 mm (99.8% purity, Sigma-Aldrich) were employed as the growth substrates for all LPCVD experiments. Prior to growth, the foils were mechanically polished using a commercially available Brasso polish to ensure surface smoothness and remove any native oxide layers. Residual polish was immediately removed with sequential rinses in acetone and isopropanol (IPA). To further clean the surface, the foils were sonicated in a dilute hydrochloric acid solution (2 M) and subsequently rinsed and sonicated in acetone and IPA for 20 minutes each. The substrates were then blow-dried with nitrogen gas and placed on quartz boats within the central hot zone of the tube furnace.

Ammonia borane (25–30 mg) was used as the growth precursor, loaded into a crucible positioned approximately 50 cm upstream from the heating zone to control vapour transport. Before initiating the growth, the crucible chamber was backfilled with argon to a pressure of

2 Torr and then sealed. The furnace tube was subsequently evacuated and purged with argon (500 sccm) for 10 minutes to eliminate residual gases. Once a stable pressure below 10 mTorr was confirmed—indicating the absence of leaks—the system underwent an extended argon purge for 30 minutes. Heating was then initiated under a continuous flow of Ar/H_2 (5% H_2 in Ar, 300 sccm), with the furnace ramped at a rate of 10 °C/min until it reached 1040 °C. At this stage, the copper foils were annealed for two hours. During annealing, the precursor crucible was gradually heated at a similar rate (10 °C/min) so that precursor sublimation coincided with the end of the annealing stage.

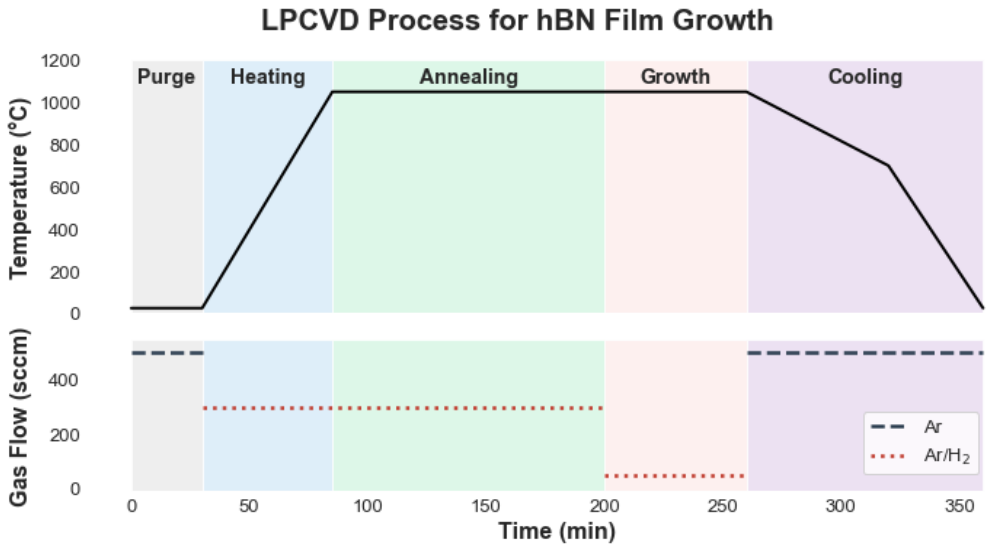

Figure 3.2: Process schematic of LPCVD growth cycle for hBN films. *The top panel shows the temperature profile through each stage: initial Ar purge, controlled heating to ~1040 °C, extended annealing, precursor-assisted growth, and gradual cooling. The lower panel indicates corresponding carrier gas conditions, with argon and dilute hydrogen/argon mixtures used to stabilize the furnace environment and regulate precursor delivery. Together, these profiles highlight the interplay between thermal ramps and gas flow in governing crystalline quality and defect incorporation.*

Following annealing, the carrier gas flow was reduced to 50 sccm Ar/H_2, and the system pressure was stabilised at 2 Torr. The crucible valve was then opened to release the

precursor vapour, initiating hBN growth. The chamber pressure was monitored throughout the process, with a characteristic pressure spike observed approximately 20 minutes into growth across all experimental runs, corresponding to the decomposition of ammonia borane. Film growth proceeded for approximately 45 minutes before the crucible was sealed. At this point, the carrier gas composition was returned to 500 sccm Ar and 50 sccm Ar/H_2, with the system pressure maintained at 2 Torr. Controlled furnace cooling was initiated at the same ramp rate until the temperature dropped below 600 °C, after which the carrier gas was switched to pure argon (50 sccm) until the system returned to room temperature.

Table 3.1: *Growth parameters systematically varied during LPCVD synthesis of hBN.*

Sample Number	**Temperature (**°C)	**Time** (min**)**	**Heat/Cool Rate (**°C/min**)**
1	1040	40	8
2	1000	40	8
3	1020	40	8
4	1060	40	8
8	1040	10	8
9	1040	20	8
10	1040	30	8
11	1040	40	4
12	1040	40	6
13	1040	40	10

To move ahead with these experiments the standard growth was repeated three times to confirm reproducibility. Each of the listed parameters in the ***Table 3.1*** were then varied to test their effect on the film and the incorporated SPEs. To ensure reproducibility, the standard growth procedure was repeated three times prior to parameter variation experiments. Subsequently, individual growth parameters—including temperature, duration, and heating/cooling rates—were systematically varied to evaluate their influence on film quality and single-photon emitter (SPE) incorporation.

For post-growth analysis, the hBN films were transferred onto SiO_2 substrates (90 nm oxide) using a PMMA-assisted wet transfer method. The copper foils supporting the as-grown films were spin-coated with PMMA at 3600 rpm for 60 seconds and briefly heated on a hotplate (1 minute) to enhance adhesion between PMMA and hBN. The foils were then floated on a 0.5 M ammonium persulfate solution to etch away the copper. Once etching was complete, the hBN/PMMA stacks were rinsed three times in Milli-Q water before being scooped onto target SiO_2 substrates. To remove trapped bubbles and minimise cracking, the samples were heated sequentially at 30 °C (20 minutes) and 150 °C (20 minutes). The PMMA layer was then dissolved by immersing the samples in N-methyl-2-pyrrolidone (NMP) for two hours. Finally, the transferred films were annealed at 500 °C in ambient air to remove residual polymer contamination and improve surface cleanliness.

3.2.2.1 Materials Characterization

Raman spectroscopy**:** The vibrational modes of hBN were examined using a Renishaw inVia confocal Raman system. [177,178] A 633 nm laser served as the excitation source. Prior to analysis, the spectrometer was calibrated with a silicon reference substrate,

fixing the primary Si peak at 520 cm^{-1}. The acquired spectra of hBN, particularly the characteristic E_2g phonon mode, were fitted with a Lorentzian function to determine peak position and full width at half maximum (FWHM). These parameters provided insight into the crystalline quality of the films after transfer onto SiO_2 substrates. [177,179]

Fourier Transform Infrared Spectroscopy (FTIR). measurements were carried out to further probe the vibrational properties of hBN using a Thermo Scientific Nicolet 6700 instrument equipped with an attenuated total reflectance (ATR) setup. Importantly, the spectra were collected after the hBN films were transferred onto SiO_2 substrates, enabling evaluation of the material without artefacts from the copper growth substrate.[180–182]

Atomic Force Microscopy (AFM). Nanoscale surface features of the hBN films were characterised using a Veeco Dimension 3100 AFM operating in tapping mode. [183–185] The system employed a silicon cantilever with a nominal tip radius of 8 nm (MikroMasch, CSC17/Ti-Pt). High-resolution topographical images were obtained with a scan resolution of 512 × 512 pixels. The data were analysed using Nanoscope Analysis 1.5 software to extract key surface parameters, including step height and surface roughness. Roughness was expressed in terms of average deviation (Ra) and root-mean-square average (Rq) of surface height variations. [183]

Scanning Electron Microscopy (SEM). The morphology of transferred hBN films on Si/SiO_2 substrates was studied using SEM. [186] Imaging was conducted on a Zeiss Supra 55 VP microscope, which provided high-resolution images that enabled assessment of surface uniformity and film continuity.

3.2.2.2 Optical Characterization

PL Spectroscopy. The optical properties of single-photon emitters (SPEs) were investigated using a custom-built scanning confocal microscope. [187–189] Excitation was provided by a continuous-wave 532 nm laser (Laser Quantum, Gem 532). The laser beam was passed through a 532 nm line filter and its polarization adjusted with a half-wave plate before being focused onto the sample using a high numerical aperture objective (100 X, 0.9 NA, Nikon). Sample scanning was achieved by a fast-steering mirror (FSM-300) in the X–Y plane. The emitted PL was separated from the excitation light by a 532 nm dichroic mirror and filtered with a 568 nm long-pass filter. The collected signal was then coupled into a 62.5 μm core graded-index multimode fibre, which simultaneously functioned as the confocal pinhole.

For detailed spectral and temporal analysis, a movable mirror redirected the signal to either an Acton SpectraPro spectrometer for spectral acquisition or to a pair of avalanche photodiodes (APDs) arranged in a Hanbury Brown–Twiss (HBT) interferometer for photon correlation measurements.[190–192] Photon arrival times were recorded using a PicoHarp 300 time-correlated single-photon counting module, which also enabled time-resolved PL lifetime measurements when combined with a supercontinuum laser source (Fianium WhiteLase).[193–195] The second-order autocorrelation function, $g^2(\tau)$, was calculated from the HBT data and fitted to confirm single-photon emission, typically without background correction unless explicitly noted.[192]

3.2.3 Results

Here we show that LPCVD grown hBN on Cu natively hosts a room-temperature single-photon emitter (SPE) suitable for scalable photonic integration. Figure 3.3 consolidates the key evidence: (i) lattice-vibrational fingerprints confirming crystalline hBN, (ii) optical identification of a single emitter via antibunching, and (iii) sustained photostability under continuous excitation—collectively establishing the relevance of this materials platform. [15,17,29,46,52,56,66] The films exhibit the expected phonon signatures. FTIR reveals a pronounced LO phonon resonance characteristic of ordered sp^2-bonded hBN *Fig. 3.3(d)*.[52,54] Raman spectroscopy shows a sharp E_{2g} mode at ~1367 cm^{-1} *Fig. 3.3(e)*, consistent with high-quality CVD hBN on Cu and indicative of low average disorder and strain. [34,103–105,177–181] These measurements confirm that the subsequent optical response originates from crystalline hBN rather than parasitic phases. Under room-temperature continuous-wave excitation, the PL spectrum displays a visible emission band typical of defect centers in hBN *Fig. 3.3(c)*. [56,65,69] The inset shows the second-order photon correlation with $g^{(2)}(0) \approx 0.37$, demonstrating antibunching from a single emitter embedded in the as-grown film.[15,17,21,56] This verifies that LPCVD growth can yield addressable SPEs without ion or e-beam activation required in alternative workflows. [61,83]

The emitter is stable at modest pump power: the intensity time trace at 300 μW is stationary with a narrow, unimodal count distribution, *Fig. 3.3 (f)*, comparable to best-in-class room-temperature stability in hBN. [17,56,58,65,66] Such stability at low-to-moderate excitation is essential for integrated quantum photonics and sensing. While definitive microscopic assignment is beyond the present dataset, the observed emission energy together with Cu-based CVD conditions aligns with carbon and oxygen-related native defects or N-

interstitial complexes, these families are supported by correlated microscopy and first-principles studies. [65,70–74]

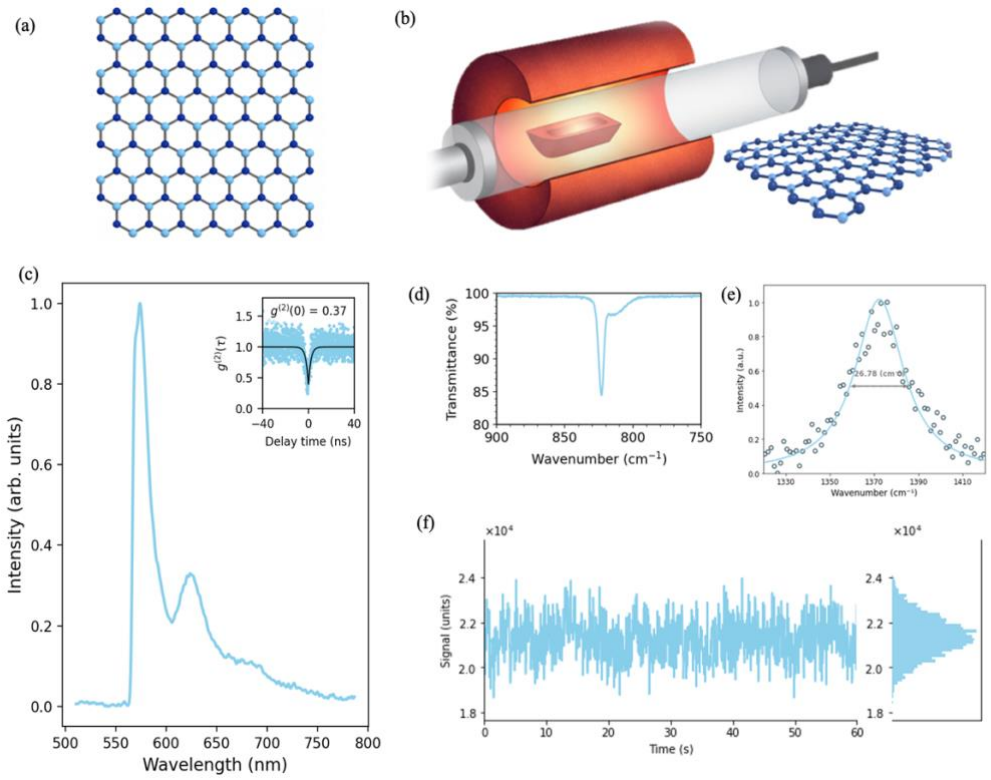

Figure 3.3: Structural, optical, and spectroscopic characterization of hexagonal boron nitride (hBN). *(a) Atomic model of the hBN lattice, showing the hexagonal arrangement of alternating boron and nitrogen atoms. (b) Schematic of the chemical vapor deposition (CVD) growth setup. (c) Room-temperature photoluminescence spectrum (PL) of hBN. The inset displays the second-order autocorrelation function $g^{(2)}(0) < 0.5$, confirming the single-photon emitter. (d) Fourier transform infrared (FTIR) spectrum from as-grown hBN on Cu, highlighting the longitudinal optical (LO) phonon modes characteristic of hBN. (e) Raman spectroscopy of hBN transferred from Cu substrates, spectra shows the sharp phonon mode centered around ~1367 cm^{-1}, characteristic of crystalline hBN. (f) Representative stability measurement of a single-photon emitter (SPE) under continuous-wave laser excitation at 300 μW, demonstrating the emitter's intensity fluctuations over time. The histogram on the right shows the statistical distribution of signal counts, confirming stable emission within the acquisition window.*

In summary, *Fig. 3.3* establishes that LPCVD on Cu produces crystalline hBN with robust phonon fingerprints (FTIR/Raman), hosts a room-temperature single-photon emitter verified by $g^{(2)}(0) < 0.5$, and exhibits stable emission at 300 μW, a cohesive set of observations that underpins the viability of LPCVD grown hBN for emitter on-chip architectures. [29,46,56,66]

The effect of growth temperature on the crystalline quality of LPCVD-grown hBN films and their associated emitters is shown in *Fig. 3.4*. Raman spectroscopy provides a clear indication of temperature-dependent crystallinity. Films grown at 1000 °C and 1040 °C (blue and green, *Fig. 3.4(a)*) show relatively broad E_2g phonon linewidths of ~ 34–29 cm^{-1}, indicative of increased disorder and grain boundary scattering. In contrast, the 1060 °C film (pink) exhibits a pronounced narrowing of the linewidth to ~ 26 cm^{-1}, reflecting improved crystalline order and a reduction in structural defects. At the highest temperature of 1080 °C (purple), the linewidth broadens again to ~32 cm^{-1}, suggesting a loss of crystalline uniformity, likely due to increased desorption and competing nucleation effects at elevated thermal budgets. These trends are summarized in *Fig. 3.4(b)*, where the FWHM shows a distinct minimum at 1060 °C, while the Raman peak position remains essentially constant at ~1372 cm^{-1} across all conditions, confirming that strain and average lattice spacing are largely unaffected by temperature variation. [34,52,54,103–105,177–181]

The influence of temperature on emitter properties is equally significant. Photoluminescence measurements from the 1060 °C sample reveal sharp emission features in the visible range, and the representative spectrum in Fig. 3.4c shows a strong zero-phonon line. The corresponding second-order correlation yields $g^{(2)}(0) = 0.23$, well below the 0.5 threshold, confirming the presence of a single-photon emitter embedded in the film. [15,17,21,56]

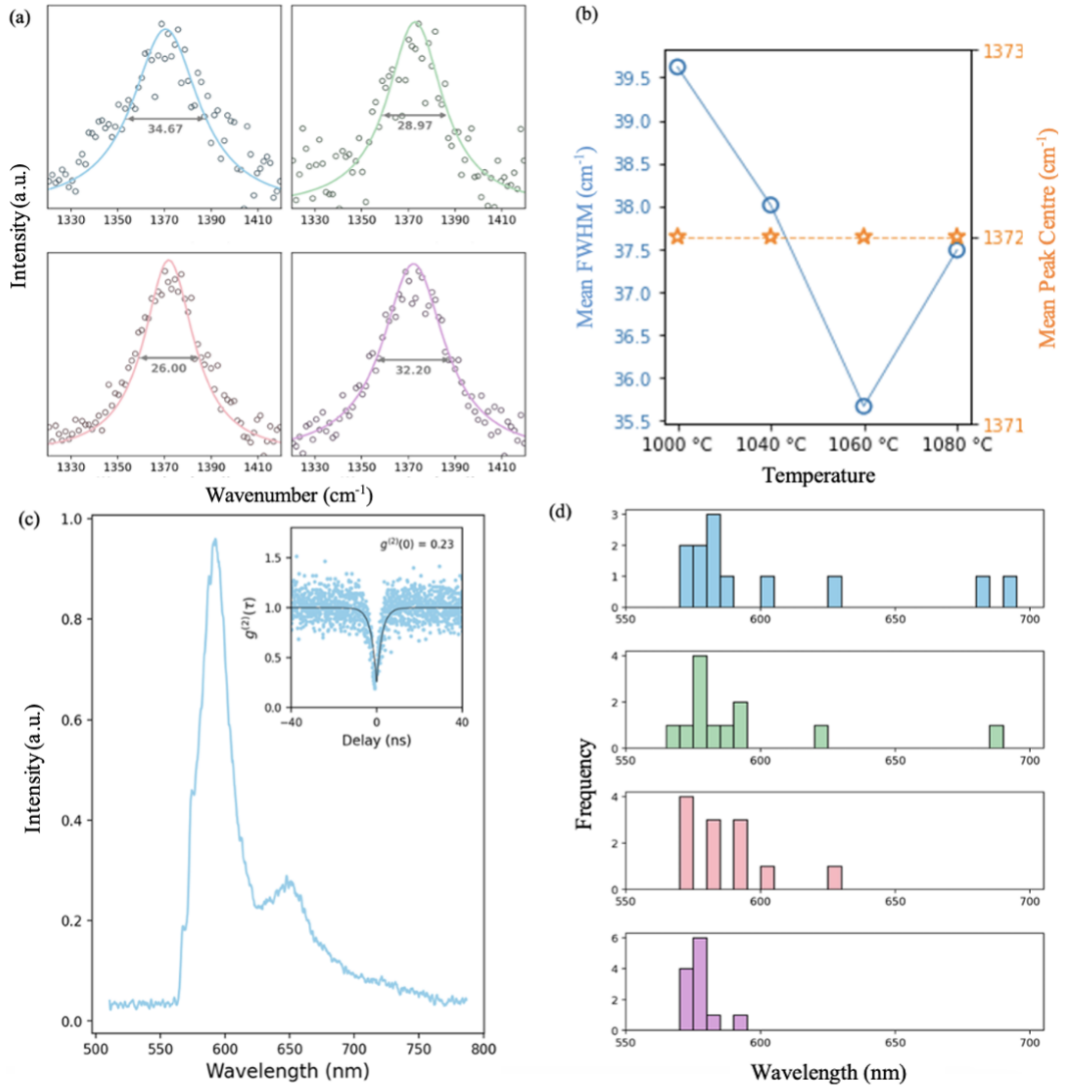

Figure 3.4: Temperature-dependent Raman and optical characterization of LPCVD-grown hBN films. *(a) Raman spectra of the E_{2g} phonon mode fitted with Lorentzian profiles for films grown at 1000 °C (blue), 1040 °C (green), 1060 °C (light pink), and 1080 °C (purple). Extracted FWHM values demonstrate a clear dependence on growth temperature. (b) Summary plot of the mean FWHM (blue, left axis) and mean peak position (orange, right axis) as a function of growth temperature. The narrowest FWHM is observed at 1060 °C, while the Raman peak position remains stable near 1372 cm^{-1}. (c) Representative photoluminescence spectrum from a single emitter in the 1060 °C sample, with the inset showing the second-order autocorrelation $g_{(2)}(0)=0.23$, confirming the quantum nature of emission. (d) Histograms of zero-phonon line (ZPL) wavelengths for emitters from each growth temperature, revealing the statistical spread and distribution of emission energies.*

This result underscores that optimized growth conditions not only improve lattice quality but also enhance emitter purity by suppressing background fluorescence. Statistical analysis of emitter ZPLs across the temperature series further highlights this trend, *Fig. 3.4 (d)*. The distributions from the 1000 °C and 1040 °C films are broad and irregular, reflecting a higher degree of spectral inhomogeneity. By contrast, the 1060 °C sample shows the narrowest and most concentrated ZPL distribution, indicating a more uniform defect environment and reduced variability in defect charge state or local strain. At 1080 °C, the spectral spread broadens again, consistent with the Raman results pointing to reduced crystalline quality at higher growth temperatures. These findings align with reports that carbon- and oxygen-related point defects, stabilized under specific thermal growth windows, dominate visible emission in hBN. [65,70–74]

Overall, the results demonstrate that 1060 °C represents the optimal growth condition for LPCVD on Cu, producing films with narrow Raman linewidths, stable lattice characteristics, and high-quality single-photon emitters. At this temperature, the interplay between nucleation kinetics and defect incorporation yields both improved crystalline order and reduced emitter inhomogeneity, establishing a growth regime favourable for scalable hBN-based quantum photonics. [29,46,56,61,66]

The sequential optical and AFM characterization reveals how the morphology of hBN films evolves with growth time. After 10 minutes, hBN domains display pronounced lateral expansion with minimal vertical accumulation, as evident in the AFM line profile where step heights remain in the low nanometre range. This stage is dominated by surface diffusion–mediated lateral growth, consistent with the early nucleation dynamics observed in low-pressure CVD processes. [177, 178]

By 20 minutes, a marked increase in film thickness is observed. AFM line profiles show step heights exceeding several tens of nanometres, while the AFM images reveal densely packed features with higher surface roughness. This indicates a transition from predominantly lateral domain expansion toward vertical accumulation, in agreement with the reservoir-limited growth models reported in the literature. [179, 180]

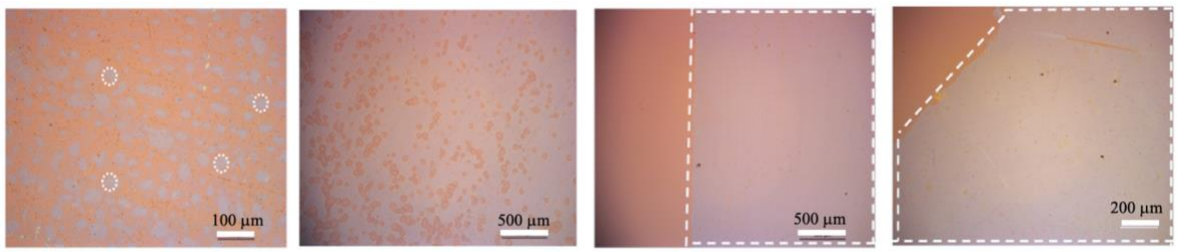

Figure 3.5: Optical microscopy of hBN films grown at different times. *Optical images of hBN transferred to SiO_2 substrates after growth durations of 10, 20, 30, and 40 minutes (left to right). The images reveal clear differences in lateral coverage and nucleation density across the time series.*

The 30-minute growth yields a more uniform film with smooth edges. AFM profiles indicate moderate step heights with improved uniformity across the sample, suggesting an optimal balance between lateral domain merging and vertical stacking. Such uniform domains are desirable for scalable electronic and photonic applications, where atomically flat, crystalline hBN layers are essential. [93, 101]

At 40 minutes, AFM analysis reveals irregular step features and increased height fluctuations, pointing to surface roughening and multilayer overlap. The corresponding optical micrograph highlights reduced uniformity compared to the 30-minute film, reflecting competing processes between continuous nucleation and vertical accumulation during prolonged growth. [179, 181]

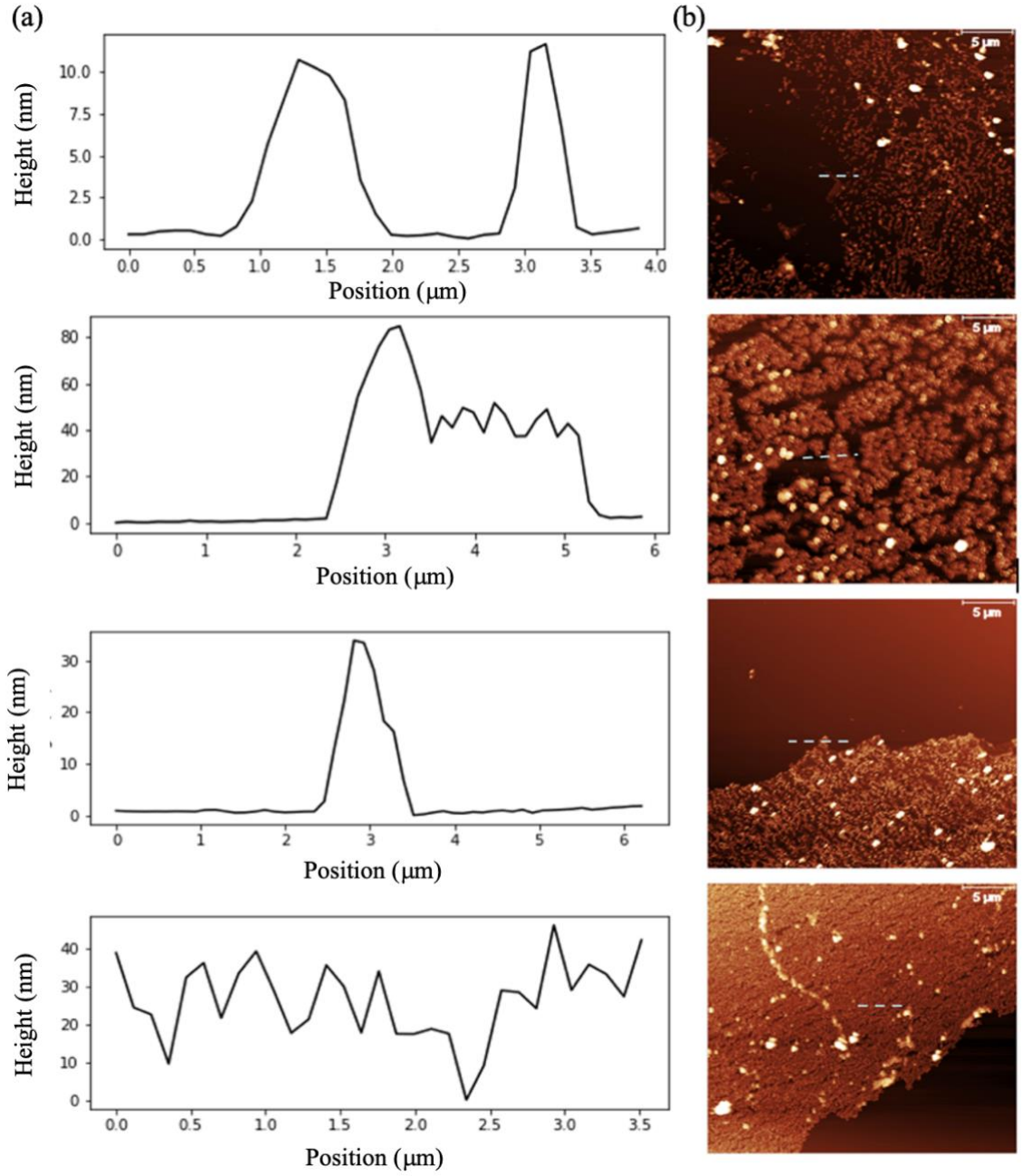

Figure 3.6: AFM analysis of hBN films grown at different times. *(a) Representative AFM line profiles taken along the dashed lines in (b), highlighting the vertical thickness and step features associated with each growth duration of hBN transferred to SiO_2 substrates after growth durations of 10, 20, 30, and 40 minutes (top to bottom). (b) AFM topographic images (30 × 30 μm²).*

Atomic Force Microscopy (AFM) roughness analysis further quantifies the morphological evolution of hBN films with increasing growth duration. Both the arithmetic

average roughness (Ra) and the root-mean-square roughness (Rq) exhibit a pronounced increase, reflecting the transition from smooth, laterally continuous layers to thicker, more irregular multilayer structures. Specifically, the roughness parameters evolve from Ra = 3.4 nm and Rq = 3.9 nm at 10 minutes to Ra = 24 nm and Rq = 27 nm at 20 minutes, before stabilising at Ra = 5 nm and Rq = 8 nm (30 minutes) and Ra = 8 nm and Rq = 10 nm (40 minutes). This non-linear trend indicates an initial rapid increase in surface roughness associated with vertical nucleation and island formation, followed by partial smoothing as the domains coalesce into thicker films. Overall, these findings demonstrate that growth time strongly governs surface morphology, offering a controllable parameter to tailor hBN thickness and roughness for specific device applications.

Single-photon emission in hBN arises from defect-related optical transitions. The zero-phonon line (ZPL) represents the direct electronic transition of the defect without phonon involvement, while the phonon sideband (PSB) originates from phonon-assisted recombination processes. The relative intensity of ZPL to PSB, typically expressed as the ZPL:PSB ratio or the Debye–Waller factor is widely used as a metric of emitter quality, with higher ratios indicating reduced electron–phonon coupling, narrower linewidths, and improved suitability for quantum applications. [17, 56, 179]

The confocal PL maps and spectra in *Fig. 3.7* reveals that both emitter density and ZPL:PSB ratios are strongly dependent on growth time. After 10 minutes, only a few isolated emitters are observed. Their PL spectra are broad, with a weak ZPL peak and dominant PSB contribution, yielding a low ZPL:PSB ratio of approximately 0.3–0.4. This indicates strong phonon coupling and explains the moderate antibunching purity of $g^{(2)}(0) \approx 0.45$. At 20 minutes, the emitter density increases significantly, and the PL spectra show a sharp ZPL

peak with suppressed PSB. The ZPL:PSB ratio increases to around 0.7–0.8, reflecting reduced phonon scattering and improved emission coherence.

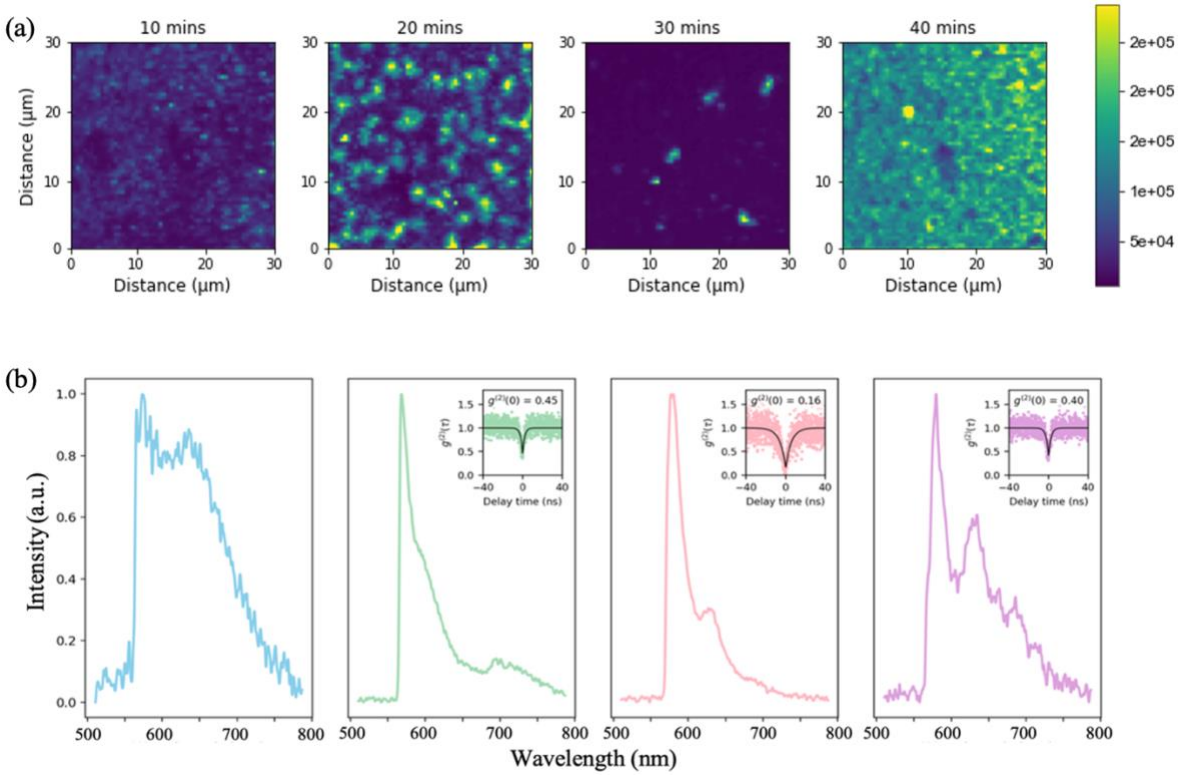

Figure 3.7: Confocal photoluminescence (PL) mapping and quantum emission analysis of hBN films grown for different times. *(a) Confocal PL intensity maps of hBN after 10, 20, 30, and 40 minutes of growth (left to right). Bright localized spots correspond to optically active defect centers, with their density increasing systematically with growth time. (b) Representative room-temperature PL spectra of single emitters for each growth duration. Insets show the corresponding second-order autocorrelation functions $g^{(2)}(\tau)$, confirming single-photon emission $\{g^{(2)}(0)<0.5\}$. The spectral contrast between the zero-phonon line (ZPL) and the phonon sideband (PSB) provides a quantitative measure of emission quality, where higher ZPL:PSB ratios correspond to reduced electron–phonon coupling and improved optical coherence.*

This is consistent with the observed high-quality single-photon emission, as evidenced by $g^{(2)}(0) \approx 0.16$, which represents the best photon purity across the growth series.

The 30-minute growth produces fewer emitters than the 20-minute case, but their optical quality is enhanced. The PL spectra are dominated by strong and spectrally isolated ZPL peaks, with PSB contributions further reduced. The ZPL:PSB ratio reaches values close to 0.8–0.9, suggesting near-optimal emission conditions with minimal phonon coupling. Together with the smoother film morphology observed at this growth duration (*Fig. 3.7*), these results confirm that intermediate growth times favour fewer but optically superior emitters.

In contrast, the 40-minute sample yields a high density of emitters, as shown by the confocal PL map. However, the PL spectra often display multiple overlapping ZPLs and broadened PSBs. The ZPL:PSB ratio decreases to about 0.4–0.5, consistent with enhanced phonon participation and background luminescence. The corresponding autocorrelation data, $g^{(2)}(0) \approx 0.40$, indicate that high emitter density at longer growth times compromises single-photon purity due to spectral crowding and defect clustering. [180, 181]

In summary, the analysis of ZPL:PSB ratios demonstrates a clear trade-off between emitter density and optical quality. Short growth produces broad spectra with low ZPL contrast, intermediate growth (20–30 minutes) yields high ZPL:PSB ratios and spectrally isolated, high-purity emitters, while prolonged growth increases emitter density but reduces optical quality due to enhanced phonon coupling and defect clustering. This emphasizes the need for growth-time optimization to achieve both high-quality and application-specific emitter characteristics.

The Raman E_{2g} phonon in hBN, normally observed around 1366–1372 cm^{-1}, is highly sensitive to lattice strain and disorder. [34, 93, 177] In this study, the phonon peak exhibits

a progressive blue-shift as the heating/cooling rate increases from 4 to 10 °C min⁻¹ *Fig. 3.8(b-c)*.

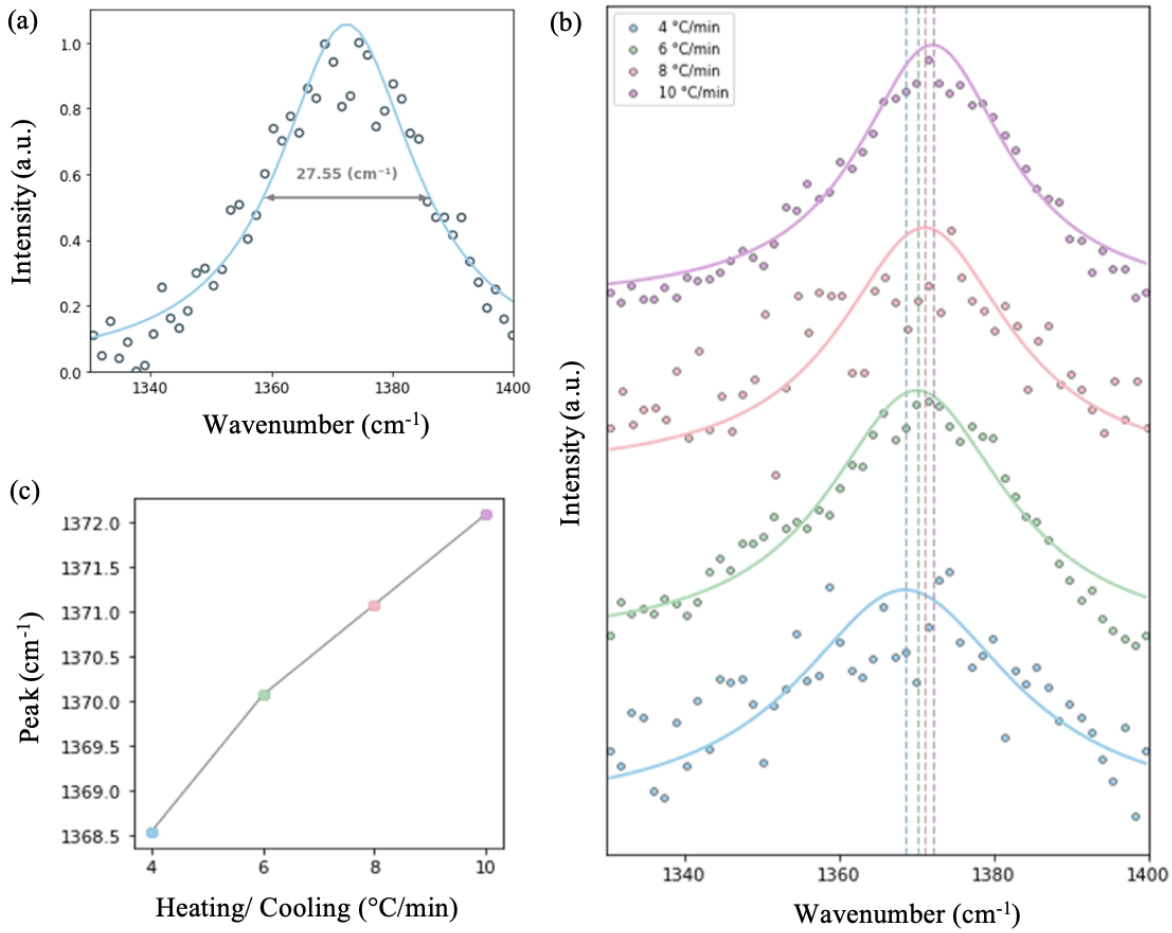

Figure 3.8: Effect of heating/cooling rate on hBN lattice phonons. *(a) Raman E_{2g} spectra of grown hBN (b) Raman E_{2g} spectra of hBN grown under different thermal ramps (4, 6, 8, and 10 °C min⁻¹; blue→green→rose→purple). Solid curves are Lorentzian fits; vertical dashed lines mark the fitted peak centers. (c) Evolution of the Raman peak center with ramp rate, showing a monotonic upshift toward ~1372 cm⁻¹ at 10 °C min⁻¹.*

A blue-shift corresponds to an increase in phonon frequency, which generally indicates stiffer in-plane B–N bonds. The most likely cause is the build-up of residual compressive strain during rapid cooling, driven by thermal-expansion mismatch between

hBN and the underlying substrate. [52, 54, 103] Faster ramps "quench" the lattice more quickly, freezing in compressive stress and leading to stronger restoring forces on the B–N vibrations.

In contrast, slower ramps (4–6 °C min^{-1}) result in Raman peaks at lower wavenumbers, i.e. a relative red-shift, consistent with a more relaxed lattice and possibly enhanced surface diffusion that allows strain relaxation and the formation of more extended defects. [139–141]

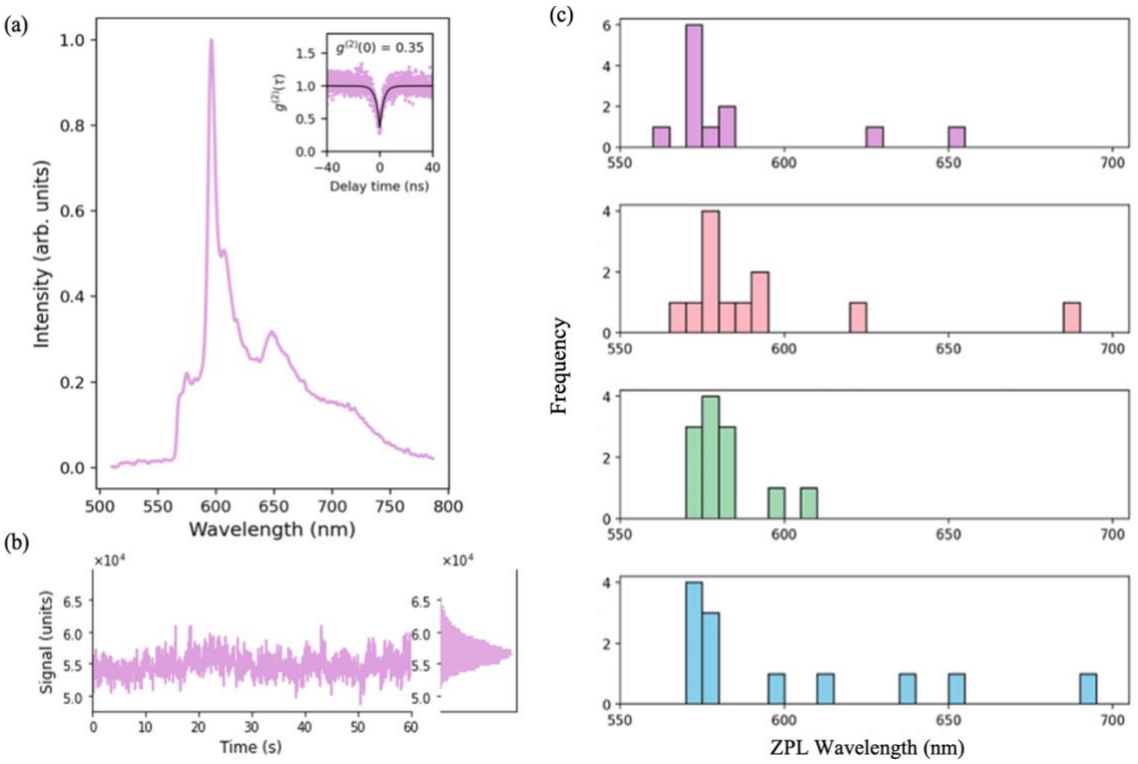

Figure 3.9: Effect of heating/cooling rate on hBN defect emission. *(a) Representative room-temperature PL spectrum from the 10 °C min^{-1} sample; inset: second-order autocorrelation with $g^{(2)}(0)=0.35<0.5$, confirming single-photon emission. (b) Intensity vs time trace for the same emitter demonstrating stable output; right panel shows the count-rate distribution. (c) Zero-phonon-line (ZPL) wavelength histograms for emitters obtained from each thermal ramp condition (4, 6, 8, and 10 °C min^{-1}; blue→green→rose→purple), illustrating changes in spectral spread and preferred emission energies.*

The absence of significant linewidth broadening across the ramp range suggests that disorder is not the dominant factor; instead, strain is the main driver of the observed blue-shift. These structural changes correlate with emitter statistics. At low ramp rates, the ZPL histograms *Fig. 3.9(d)* show broad distributions with longer-wavelength ZPLs, reflecting inhomogeneous strain and charge microenvironments. As the ramp increases, the ZPLs shift toward shorter wavelengths (a blue-shift in emission) and cluster more narrowly around 580–620 nm. This trend indicates more uniform strain fields and a stabilization of a specific family of visible defect centers. [58, 65, 66] A representative emitter from the 10 °C min^{-1} condition, *Fig. 3.9 (a, b)* exhibits a strong ZPL with suppressed phonon sideband (PSB) intensity, along with single-photon purity ($g^{(2)}(0) = 0.35$) and high photostability. The stronger ZPL and reduced spectral diffusion at higher ramp rates are consistent with a strain-stabilized defect environment that minimizes phonon-assisted transitions and blinking. [17, 56, 66]

In summary, faster thermal ramping induces a blue-shift in the Raman phonon and a corresponding blue-shift and narrowing of ZPL emission, both of which are attributed to compressive strain effects. Slower ramps yield relatively red-shifted and more broadly distributed features, consistent with a relaxed but more heterogeneous defect environment. These findings demonstrate that thermal ramp engineering provides a powerful lever to tune strain and, in turn, control both lattice vibrations and single-photon emitter quality in LPCVD-grown hBN.

3.3 hBN Growth- position dependent variation

3.3.1 Introduction

The controlled bottom-up synthesis of hexagonal boron nitride (hBN), spanning atomically thin monolayers to multilayered films, has been extensively explored through chemical vapour deposition (CVD) and other vapour-phase growth methods over the past decade. [142–144] Although position-dependent growth phenomena are well documented for graphene where variations in precursor concentration, temperature gradients, and boundary-layer flow strongly influence nucleation density and stacking sequence[185–187] comparable analyses for hBN remain limited.

In this study, we systematically investigate how substrate position within the CVD furnace influences hBN growth behaviour, including film morphology, crystallinity, and layer thickness. Such position dependence arises primarily from non-uniformities in local temperature distribution, precursor residence time, and carrier-gas velocity, which together modulate the decomposition kinetics of boron- and nitrogen-containing precursors (e.g., ammonia borane, borazine). [188–190] These variations directly affect the rates of precursor pyrolysis, mass transport, and surface adsorption–desorption equilibria, ultimately leading to spatially distinct growth modes ranging from atomically smooth monolayers to rougher multilayer domains. [191]

A detailed understanding of these thermo-kinetic and transport phenomena is essential for achieving wafer-scale uniformity and reproducibility in hBN film fabrication. By correlating furnace-zone position with experimentally measured parameters such as AFM roughness, Raman FWHM, and optical contrast, this work establishes a foundation for

optimising growth environments. This includes fine-tuning of precursor delivery rates, carrier gas composition, and thermal zoning strategies to enable the scalable synthesis of high-quality hBN with precise control over structural and electronic properties. [192–194]

3.3.2 Methodology

The LPCVD standard hBN growth method described in the previous section of this chapter was utilised to conduct this experiment. *Figure 3.8* presents a schematic of the chemical vapor deposition (CVD) furnace used for hBN growth, including detailed specifications and measurements. The furnace comprises a quartz growth tube housed within a heating chamber. The quartz tubes employed in these growths were customised to ensure the complete elimination of any contaminants. Infused quartz tubes capable of withstanding temperatures of up to 1200 °C (AdValue Technology, Fused Quartz Tube – OD 50 mm × ID 46 mm × L 1219 mm) were used.

The tube was connected to a vacuum pump on the left side and to a crucible on the right, which contained the solid precursor (ammonia borane) for hBN growth. Gas lines fitted on the right introduced argon (Ar) and hydrogen (H_2), with flow rates controlled using mass flow controllers (MFCs).

Samples were placed at positions A, B, and C located 20 cm, 30 cm, and 40 cm, respectively, from the crucible. Following growth, the samples were transferred onto SiO_2 substrates, treated with NMP for PMMA residue removal, and further annealed. Finally, the obtained samples were characterised to investigate the effect of sample position in the furnace on their optical properties.

Photoluminescence (PL) spectroscopy: Single-photon emitter properties were investigated using a confocal microscope excited with a continuous-wave 532 nm laser. Emission was spectrally filtered and directed either to a spectrometer for spectral acquisition or to a Hanbury Brown–Twiss interferometer with APDs for photon correlation and lifetime measurements.[187–195] The second-order autocorrelation function, $g^2(\tau)$, was evaluated to confirm single-photon emission. Additional details of the PL setup can be found in Section 3.2.2.

Wide-field EMCCD imaging: To gain an overview of the spatial distribution of quantum emitters in the hBN samples, wide-field imaging was carried out with an Electron-Multiplying CCD (EMCCD) camera. Unlike confocal microscopy, which restricts detection to a single diffraction-limited spot, wide-field imaging makes it possible to capture many emitters within one field of view.

A 532 nm continuous-wave laser was used as the excitation source, with a power of about 3 mW. The beam was expanded and weakly focused so that an area of roughly 5 × 5 μm^2 on the sample surface was illuminated uniformly. Photoluminescence from the sample was collected with a high-NA objective, spectrally filtered to remove residual excitation light, and imaged onto the EMCCD. For each measurement, a sequence of 100 frames was recorded with an exposure time of ~200 ms. The electron-multiplying function of the EMCCD enhanced the detection of weak signals, making it possible to resolve faint single-photon emitters alongside brighter ones. In this way, several emitters could be observed at once and their relative brightness, distribution, and stability compared across the illuminated region.

This wide-field approach provided a fast way to survey large areas of CVD-grown hBN and identify regions of interest for further study with confocal microscopy.

Raman spectroscopy Fourier: Vibrational modes of hBN were characterised using a Renishaw inVia confocal Raman system with a 633 nm excitation laser. Calibration was performed with a silicon reference at 520 cm^{-1}. The characteristic E_2g phonon mode was fitted with a Lorentzian profile to extract peak position and FWHM, providing information on crystalline quality after transfer onto SiO_2 substrates. [177–179] Full details of the setup are described in Section 3.2.2.

Transform Infrared Spectroscopy (FTIR): FTIR measurements were carried out with a Thermo Scientific Nicolet 6700 system equipped with an ATR unit. Spectra were acquired from hBN films after transfer onto SiO_2 substrates, enabling evaluation of the vibrational response without artefacts from the copper growth substrate. [180–182] Further experimental parameters are provided in Section 3.2.2.

3.3.3 Results

To ensure accurate control of furnace temperature, the controller set values (SV) were calibrated against the actual temperatures measured using an external thermocouple (Thermo). Figure 3.10(b) shows the measured temperature plotted as a function of the set value, together with linear, quadratic, and cubic polynomial fits. While the linear model ($R^2 \approx 0.986$) captured the overall trend, the quadratic fit ($R^2 \approx 0.999$) provided an improved description. The cubic fit achieved the best performance ($R^2 \approx 0.9995$), accurately capturing the slight nonlinearity observed at higher setpoints.

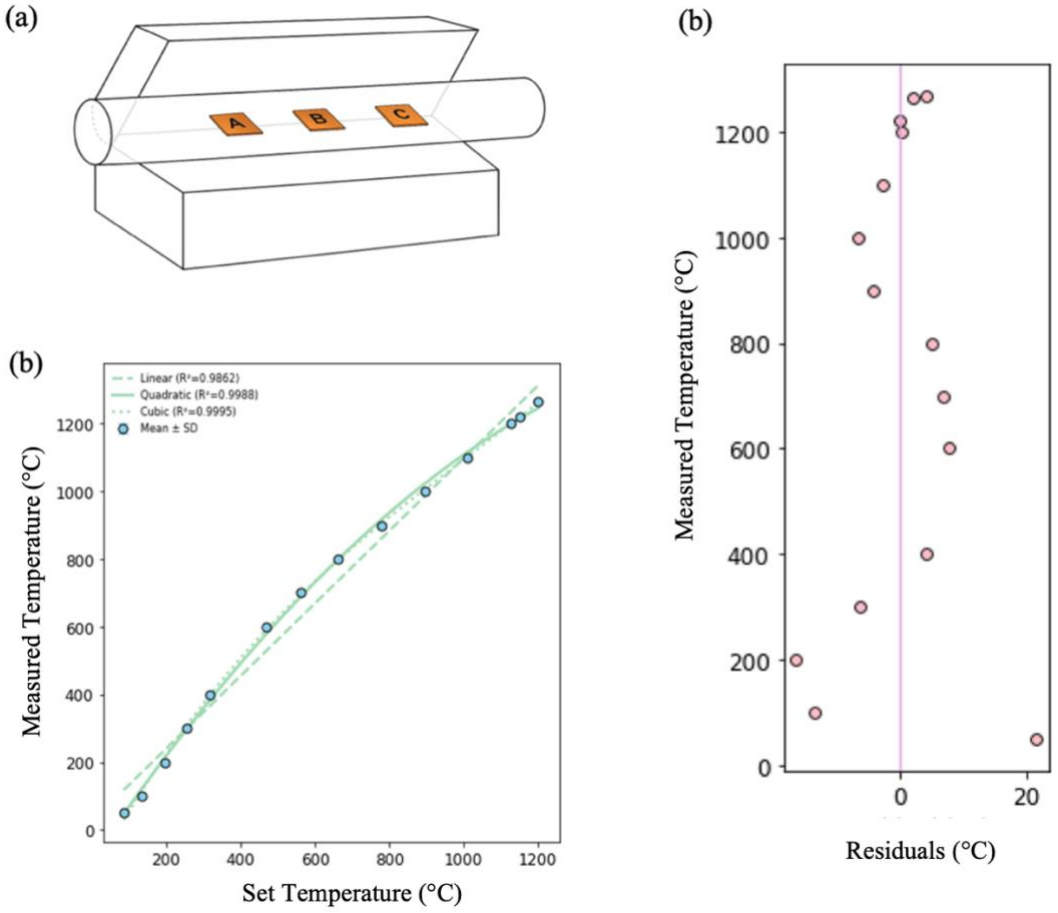

Figure 3.10: Setup Schematic and Controller calibration. *(a) Schematic illustration of the quartz tube furnace setup used for LPCVD growth of hBN, showing three copper substrates (A, B, and C) positioned along the central heating zone to study temperature-dependent growth behaviour. The quartz tube is transparent to indicate the relative positions of the samples inside the furnace. (b) Calibration curve of the measured temperature versus the set furnace temperature, fitted using linear, quadratic, and cubic models, showing excellent correlation ($R^2 > 0.99$). (c) Residual plot illustrating the deviation between measured and fitted temperatures, confirming uniformity and high accuracy in the temperature calibration across the experimental range.*

Residual analysis, shown in the right panel of *Figure 3.10(c)*, presents the deviation between fitted and measured values as a function of temperature. Residuals were generally small across the full operating range (20–1267 °C), with repeated measurements at 1200 °C

demonstrating good reproducibility (1266 ± 1 °C, n = 2). These results confirm that the cubic calibration provides the most reliable mapping between controller setpoints and true furnace temperatures, and this model was therefore used to correct experimental setpoints in subsequent analyses.

The Raman and XPS analyses reveal a strong position-dependent variation in structural quality along the furnace axis. The left-zone sample (blue) displays the narrowest and most intense E_2g Raman peak, suggesting well-ordered, multilayer hBN with large crystalline domains and minimal lattice distortion. The centre sample (green) shows slightly broader and less intense peaks, indicating moderate disorder, while the right-zone sample (pink) presents weak and broad features consistent with poor crystallinity and thinner, defect-rich growth. XPS spectra across all samples exhibit B 1s and N 1s peaks centred at ~190.2 eV and ~398.1 eV, respectively, characteristic of stoichiometric B–N bonding. The absence of significant B–O or C–N components suggests that the observed quality differences stem from variations in crystalline order rather than chemical composition.

These trends can be attributed to the spatial variation in the local reaction environment within the quartz-tube furnace, especially the decomposition behaviour of the ammonia borane ($H_3N{\cdot}BH_3$) precursor under the influence of the Ar/H_2 carrier gas mixture. Hydrogen plays a dual role in the growth mechanism. First, it promotes dehydrogenation of ammonia borane and intermediate species such as borazine ($B_3N_3H_6$), accelerating the formation of reactive B–N radicals. These radicals subsequently adsorb and react on the catalytic copper surface to form sp^2-bonded hBN networks. Second, hydrogen assists in surface cleaning and oxide reduction on the Cu substrate, improving adatom diffusion and facilitating lateral domain growth. The left position, located slightly upstream of the central furnace region,

provides an environment where the local temperature, gas velocity, and precursor concentration

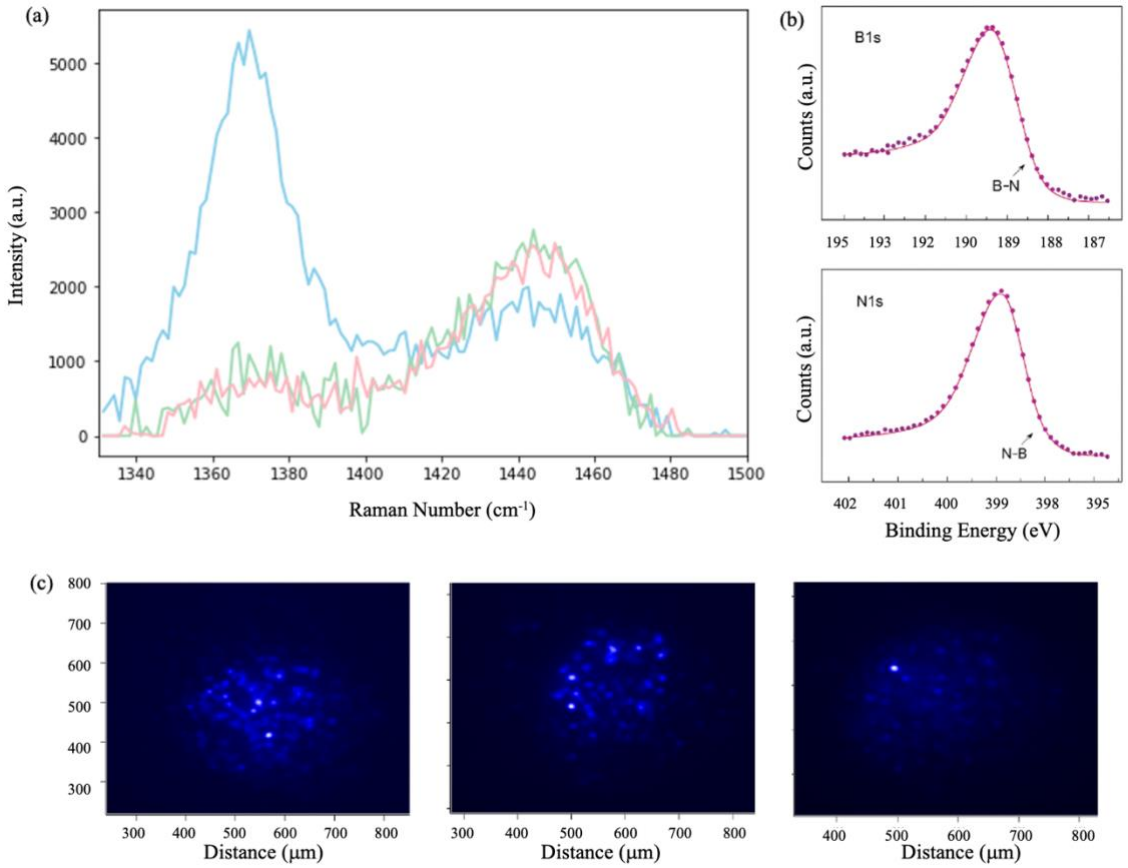

Figure 3.11: Raman and Widefield imaging of grown hBN film. *(a) Raman spectra of hBN films grown at three furnace positions: left (blue), centre (green), and right (pink). Each spectrum displays the E_2g phonon mode near ~1366 cm^{-1}, confirming crystalline hexagonal boron nitride formation. The left (blue) position shows the sharpest and most intense peak, signifying the highest crystallinity and most uniform multilayer structure. The centre (green) spectrum is moderately intense, while the right (pink) position exhibits the broadest, weakest peak, indicative of reduced crystalline order and increased structural disorder. (b) High-resolution XPS spectra of the B 1s and N 1s core levels, each fitted with a single dominant B–N/N–B component, confirming sp^2-bonded hBN with negligible contamination. (c) Wide-field images of hBN films grown at the left, centre, and right furnace positions. Each circular illuminated region corresponds to the excitation beam footprint on the sample surface. Emission intensity and spot density variations within these regions reflect spatial differences in emitter density and optical activity.*

are optimally balanced. Here, the hydrogen fraction is sufficient to activate ammonia borane decomposition while preventing excessive etching, resulting in rapid yet controlled surface nucleation and diffusion. Consequently, hBN domains grow laterally with minimal defect incorporation, producing the sharp raman peak and the dense, bright emitter population observed in the PL image.

At the furnace centre, the gas mixture remains reactive but hydrogen-driven etching becomes more pronounced. This condition maintains stoichiometry but partially suppresses lateral growth, leading to moderately crystalline films with reduced emitter density. In contrast, the right position lies downstream, where precursor depletion and by-product accumulation lower the effective reactive flux reaching the substrate. The diminished availability of BN species, combined with increased H_2:precursor ratios, favours etching over deposition. As a result, the right-zone sample exhibits the lowest Raman intensity and a sparsely populated PL map dominated by isolated emission sites.

Wide-field PL imaging offers direct visual evidence of these position-dependent effects. The circular illuminated areas correspond to the excitation beam footprint from a collimated 532 nm continuous-wave laser, expanded to a field of view of approximately tens of micrometres. Within each illuminated region, the intensity distribution and emitter density correspond to the underlying film morphology. The left sample exhibits the brightest and most densely distributed emission centres, consistent with its superior crystallinity. The centre sample shows a moderate density of emitters, and the right sample displays only a few dim emission spots, indicative of poor defect activation and lower optical quality.

Overall, these results demonstrate that the carrier gas composition and local growth environment jointly dictate the morphology and optical properties of hBN. The left furnace

zone offers the most favourable balance between ammonia borane decomposition, hydrogen-assisted surface reactions, and copper-catalysed diffusion, leading to the formation of uniform, stoichiometric, and optically active hBN films. In contrast, the centre and right regions exhibit suboptimal conditions due to excessive hydrogen etching and precursor depletion, respectively. Careful optimisation of the Ar/H_2 ratio and temperature profile is therefore essential to achieve spatially uniform, high-crystallinity hBN suitable for optoelectronic and quantum emitter applications.

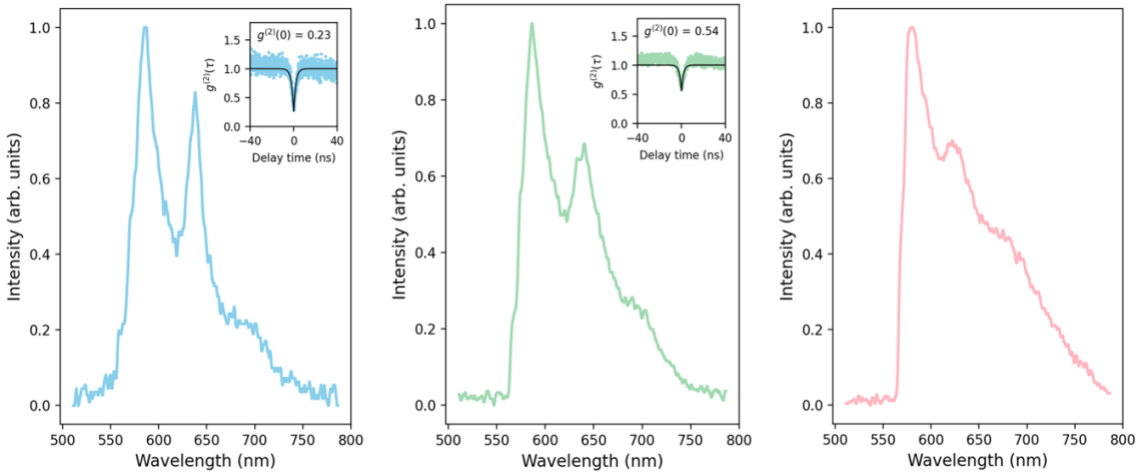

Figure 3.12 – Photoluminescence (PL) spectra and photon correlation from hBN samples at positions A–C. *PL spectra recorded from hBN samples grown at positions* ***A (20 cm)***, ***B (30 cm)***, *and* ***C (40 cm)*** *inside the furnace. The spectra reveal multiple emission features in the visible range (500–800 nm), with prominent peaks around 600–650 nm associated with quantum emitters in hBN. Insets show second-order autocorrelation measurements, $g^2(\tau)$, confirming single-photon emission behaviour for selected emitters: position A exhibits strong antibunching with $g^2(0) \approx 0.23$, position B shows partial suppression with $g^2(0) \approx 0.54$, while position C displays ensemble-like emission without clear antibunching signature.*

PL spectra were recorded from hBN samples grown at positions A (20 cm), B (30 cm), and C (40 cm) inside the furnace, distance measured from precursor position. The spectra show emission features in the visible range (500–800 nm), with strong peaks around

600–650 nm. Insets display second-order autocorrelation measurements, $g^2(\tau)$, confirming differences in single-photon emission behaviour between the three samples: position A shows clear antibunching with $g^2(0) \approx 0.23$, position B exhibits partial suppression with $g^2(0) \approx 0.54$, while position C indicates ensemble-like emission without evidence of single-photon statistics.

The PL measurements highlight how the location of the sample within the furnace affects emitter properties. At position A, the spectrum is dominated by sharper peaks, and the autocorrelation dip demonstrates non-classical light emission, indicating stable single-photon emitters. At position B, the spectral features are broader and less isolated, and the $g^2(0)$ value suggests mixed emission from single defects and background luminescence. By position C, the spectrum appears dominated by ensemble emission, with the autocorrelation trace lacking any clear antibunching behaviour. The results show a clear spatial dependence on emitter formation, with samples closer to the crucible providing stronger and more reliable single-photon characteristics, while those further away produce broader, less distinct emission profiles. This trend reflects the impact of temperature gradients and precursor distribution across the furnace on the optical quality of hBN.

The three emitters exhibit markedly different stability profiles, reflecting variations in their defect environments. Emitter A produced the brightest output (~150 kcps) and remained photostable over the acquisition, with only brief intensity excursions that may correspond to fast charge reconfiguration events. This behaviour suggests efficient radiative recombination and minimal coupling to non-radiative channels. Emitter B, in contrast, displayed frequent fluctuations in count rate (~70 kcps on average), typical of blinking driven by charge-state switching or photoionization. Such dynamics are consistent with a high density of nearby

trap states or adsorbates that modulate the local charge environment, producing both spectral wandering and intermittent emission. Emitter C showed the lowest brightness (~45 kcps) but relatively steady output, pointing to reduced radiative efficiency rather than strong blinking, potentially due to enhanced non-radiative relaxation or partial bleaching of the defect centre.

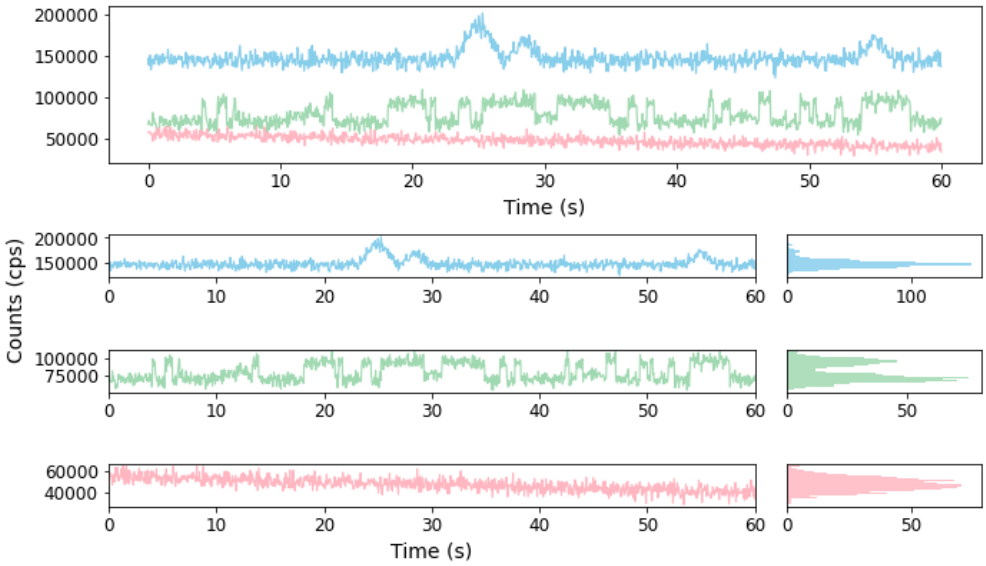

Figure 3.13: Photoluminescence stability of emitters A, B, and C. *Time-resolved photon count traces are shown for emitters A (blue), B (green), and C (pink) over a 60 s acquisition. Corresponding histograms of count distributions (right panels) highlight the intensity fluctuations and mean stability of each emitter.*

These differences underline the sensitivity of hBN single-photon emitters to their nanoscale surroundings. Interface traps at the hBN/SiO_2 boundary, local strain variations, and residual contaminants from transfer are all plausible sources of the observed instability. Previous reports have shown that encapsulation in layered dielectrics or surface passivation can suppress blinking and bleaching by screening charge noise and stabilising the defect charge state. Applying such strategies would likely enhance the reproducibility of single-photon emission in hBN and allow emitters such as A to be harnessed as reliable quantum light sources.

3.4 Conclusion

This chapter establishes quantitative links between LPCVD growth settings and the structural/optical performance of defect-based emission in hBN. A tight temperature window near ~1060 °C minimises the Raman E_2g FWHM and yields more uniform ZPL distributions, balancing lattice order with the likelihood of forming optically active point defects; growth durations of ~20–30 min maximise optical quality (higher Debye–Waller factors, cleaner antibunching) without inducing excessive spectral crowding; and faster thermal ramps (~8–10 °C min^{-1}) produce reproducible blue-shifts of Raman/ZPL peaks consistent with residual compressive strain that narrows spectral spread and stabilises emission, whereas slower ramps relax strain but increase inhomogeneity.

Position within the tube is also decisive, substrates placed upstream/centre outperform downstream placements in both structural (narrower E_2g) and optical metrics (brighter PL, lower $g^2(0)$), consistent with the interplay of precursor flux and H_2-etch chemistry; incorporating the furnace temperature-calibration fit into reported setpoints reduces systematic offsets. To ensure comparability and reproducibility, results should be reported with uniform statistics (mean ± SD, n), explicit histogram bin widths, and a clear statement of whether $g^2(0)$ values are background-corrected with associated confidence intervals. Practically, an effective recipe is to anneal near the target growth temperature and then grow at ≈1060 °C and ~2 Torr with specified Ar/H_2 flows for 20–30 min, using 8–10 °C min^{-1} ramps, placing substrates upstream/centre, transferring with a consistent cleaning protocol, and reporting Raman/PL statistics with uncertainties and counts.

Remaining limitations include propagating furnace-calibration residuals into temperature error bars, adding background-corrected $g^2(0)$ with 95% confidence intervals and standardised acquisition windows, and exploring alternative boron precursors/H_2 fractions alongside in-situ diagnostics to decouple temperature from flux effects.

4

Homoepitaxial growth of hBN on pristine flakes

The homoepitaxial growth of hexagonal boron nitride (hBN) has emerged as a powerful route to structurally coherent, defect-controlled 2D films in which intrinsic properties are preserved rather than obscured by substrate-induced disorder. Whereas growth on foreign substrates often introduces lattice mismatch, interfacial strain, surface roughness, and adventitious impurities, homoepitaxy nucleates new hBN layers directly on pre-existing hBN with the same lattice constant and symmetry. This near-perfect registry suppresses grain boundaries, promotes terrace-mediated growth, and allows the overlayer to inherit the crystallographic order of the seed. The resulting continuity is especially important for quantum photonics, where the optical behaviour and stability of single-photon emitters (SPEs) are exquisitely sensitive to local strain, charge environment, and thickness uniformity.

By retaining the chemical inertness and atomic flatness of hBN while avoiding interface-driven defect formation, homoepitaxy provides a clean platform to study emitter

stability, spectral reproducibility, and the mechanisms governing defect formation under controlled growth conditions. [103, 106, 107]

In this chapter, we establish a homoepitaxial LPCVD workflow on exfoliated hBN/SiO_2/Si that builds on the calibrated growth window from Chapter 3, it clarifies the rationale and novelty relative to the single prior report of hBN homoepitaxy. Presents a methodology aligned with Chapter 3 (temperatures, ramps, pressure/flows, substrate preparation) to enable direct comparison and quantify structural and optical outcomes via Raman E_2g position/FWHM, AFM step morphology, SEM surface continuity, wide-field/confocal PL maps and spectra, and emitter metrics where applicable. Collectively, these results demonstrate that homoepitaxy maintains crystalline order while enhancing optical response, motivating hBN as a scalable platform for deterministic emitter engineering and integrated quantum photonic devices.

4.1 Abstract

Homoepitaxial growth of hexagonal boron nitride (hBN) offers a lattice-matched pathway to highly ordered, defect-controlled films in which the intrinsic lattice environment is preserved. Building on the calibrated LPCVD window from Chapter 3, this chapter examines the controlled deposition of new hBN layers directly onto mechanically exfoliated hBN flakes supported on SiO_2/Si with a 295 nm oxide. The goal is to decouple film properties from substrate-induced disorder and to quantify how homoepitaxy affects structural coherence and optical response relevant to quantum photonics. Exfoliated flakes were selected by optical contrast and verified by AFM before growth. LPCVD parameters (temperature setpoints, pressure, Ar/H_2 flows and thermal ramps) were aligned with Chapter

3 to permit direct comparison. Structural characterisation combined AFM (surface morphology, step continuity), Raman spectroscopy (E_2g phonon position and FWHM as proxies for order/strain), and SEM (lateral uniformity), while optical characterisation used wide-field/confocal photoluminescence (PL) mapping and spectral comparison before and after growth.

Quantitatively, AFM on pristine flakes shows atomically flat terraces with step heights of ~0.33–0.40 nm, consistent with single hBN layers, and these terraces persist after growth with only a slight increase in step height indicative of layer-by-layer overgrowth (step-flow/terrace-mediated growth). Raman spectra remain centred near the characteristic E_2g mode (~1366 cm^{-1}) before and after growth, with a small post-growth shift and a modest increase in linewidth from 8.2 cm^{-1} to 9.0 cm^{-1}. This ~0.8 cm^{-1} broadening is consistent with a minor rise in strain/thickness inhomogeneity while preserving crystalline order. SEM imaging corroborates a continuous, defect-free surface without secondary grain formation or delamination. PL mapping reveals a clear enhancement in emission intensity after homoepitaxy alongside subtle spatial modulation that reflects small, lateral variations in local strain or thickness; to present these results without crowding, PL maps are shown separately from the corresponding spectra. The comparison PL spectra (pre- vs post-growth) exhibit increased integrated intensity and mild band broadening, but no emergent sub-bandgap features, indicating that the process does not introduce additional optically active impurities or non-radiative centres.

Taken together, these measurements show that homoepitaxial LPCVD on hBN preserves atomic flatness and crystallographic continuity while improving optical response. The structural metrics (E_2g near ~1366 cm^{-1}, FWHM 8.2- 9.0 cm^{-1} and terrace heights ~0.33–

0.40 nm) provide a quantitative baseline for assessing order and strain, and the optical metrics (enhanced PL intensity without new defect bands) point to cleaner emission environments suitable for reproducible studies of defect photo physics. Practically, the results validate a reproducible workflow—substrate selection, cleaning, temperature and gas flow control aligned with the calibrated furnace map, and characterisation that yields structurally coherent, optically stable homoepitaxial films. Conceptually, they demonstrate that growing hBN on hBN suppresses interface-driven disorder and stabilises the optical landscape, providing a platform for deterministic emitter engineering and scalable integration of hBN into quantum photonic device architectures.

4.2 Introduction

Hexagonal boron nitride is known for its wide bandgap (~6 eV), strong in-plane covalent bonding, and chemical stability, which make it one of the most promising materials for hosting optically active point defects that can act as single-photon emitters. However, common synthesis techniques such as chemical vapour deposition (CVD) or mechanical exfoliation often produce layers with significant inhomogeneity i.e., grain boundaries, variable thickness, and impurity incorporation—that interfere with reproducible optical performance . [34, 177, 179] Homoepitaxial growth provides a way to overcome these issues by maintaining the same atomic registry between the substrate and the newly deposited layer, thereby reducing structural disorder and maintaining surface continuity.

In this section, hexagonal boron nitride (hBN) was grown on mechanically exfoliated hBN flakes supported on SiO_2/Si substrates with a 295 nm oxide layer. The oxide thickness was selected to provide strong optical contrast for identifying thin flakes and to offer a stable

base during thermal processing. With careful control of furnace temperature and the carrier-gas composition, the newly deposited hBN followed the crystallographic orientation of the underlying flake, enabling layer-by-layer homoepitaxial growth. This alignment suppresses misfit defects and supports continuous lateral extension of the film. [195-196]

The resulting films provide a clean, uniform platform for investigating optically active defects, particularly the negatively charged boron vacancy (V_B^-). Because the overlayer remains coherent with the seed lattice, local strain and charge environments around individual defects can be better managed, which stabilises emission and improves spectral reproducibility—key requirements for quantum photonics. The same platform makes it practical to study how growth temperature, carrier-gas ratios, and layer thickness influence both the likelihood of defect formation and the resulting photo-physics. [179]

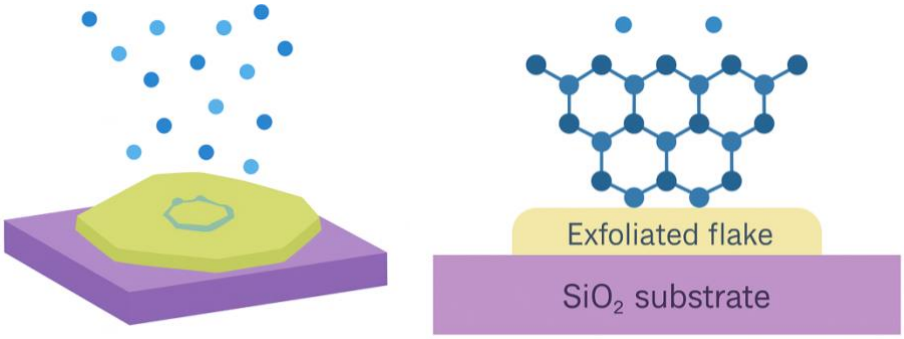

Figure 4.1 - Schematic illustration of the homoepitaxial growth of hexagonal boron nitride (hBN) on exfoliated flakes*. Left: carrier gas transports boron- and nitrogen-containing species (from the ammonia borane precursor) toward the substrate surface, where decomposition initiates on the exposed hBN flake. Right: atomic arrangement showing the aligned hBN lattice forming atop the exfoliated flake, which rests on a SiO_2/Si substrate (295 nm oxide). The coherent lattice stacking ensures minimal strain and dislocation, promoting uniform crystalline growth across the flake surface.*

Structural and optical characterisation using Raman spectroscopy, atomic force microscopy (AFM), photoluminescence (PL), and optically detected magnetic resonance

(ODMR) showed that the quality of the homoepitaxial interface directly impacts both structural coherence and optical activity. Taken together, these results provide simple guidance for reproducibly growing high-quality hBN suitable for single-photon emission and quantum sensing, linking precise thin-film synthesis to deterministic defect engineering in two-dimensional materials. [193]

The schematic illustrates the experimental configuration used for homoepitaxial growth of hBN on exfoliated flakes deposited on SiO_2/Si substrates. The oxide thickness of 295 nm enhances optical contrast for identifying thin flakes prior to growth and provides thermal stability during high-temperature processing. The precursor, ammonia borane (NH_3BH_3), decomposes at elevated temperature to release borazine ($B_3N_3H_6$) and related intermediates that serve as the reactive species. Under an Ar/H_2 carrier gas environment, these fragments are directed toward the substrate where they nucleate and attach epitaxially to the existing hBN lattice.

The right-hand schematic highlights the atomic continuity at the interface between the exfoliated flake and the newly grown layer. Because both share the same hexagonal symmetry and lattice constant, epitaxial alignment is naturally maintained, suppressing the formation of grain boundaries. The resulting homoepitaxial film preserves the intrinsic crystallinity and enables controlled study of defect formation within an atomically clean environment.

4.3 Methodology

Sample Preparation and Growth: Homoepitaxial growth of hBN was carried out on mechanically exfoliated hBN flakes supported on SiO_2/Si substrates with a 295 nm thermal oxide layer, selected to provide strong optical contrast for identifying flake thickness and

lateral uniformity. The substrates were first cleaned sequentially in acetone and isopropanol (IPA), followed by a nitrogen blow-dry and hot-plate bake to remove physiosorbed moisture. To further minimise surface contaminants prior to flake transfer, the cleaned substrates were annealed in air at 450 °C for 30 minutes.

Japanese bulk crystals (*Batch No. M994)* were used as the source material for hBN exfoliation. Mechanical exfoliation was performed using adhesive tape, and flakes with large lateral dimensions were identified under optical microscopy using the characteristic colour contrast afforded by the 295 nm oxide layer. To reduce potential carbon-based residues associated with the exfoliation tape, the freshly prepared substrates were exposed to ultraviolet (UV) ozone for 1 minute prior to loading into the LPCVD furnace. This brief surface treatment has been shown to effectively remove polymeric contaminants without introducing measurable disorder into the hBN lattice.

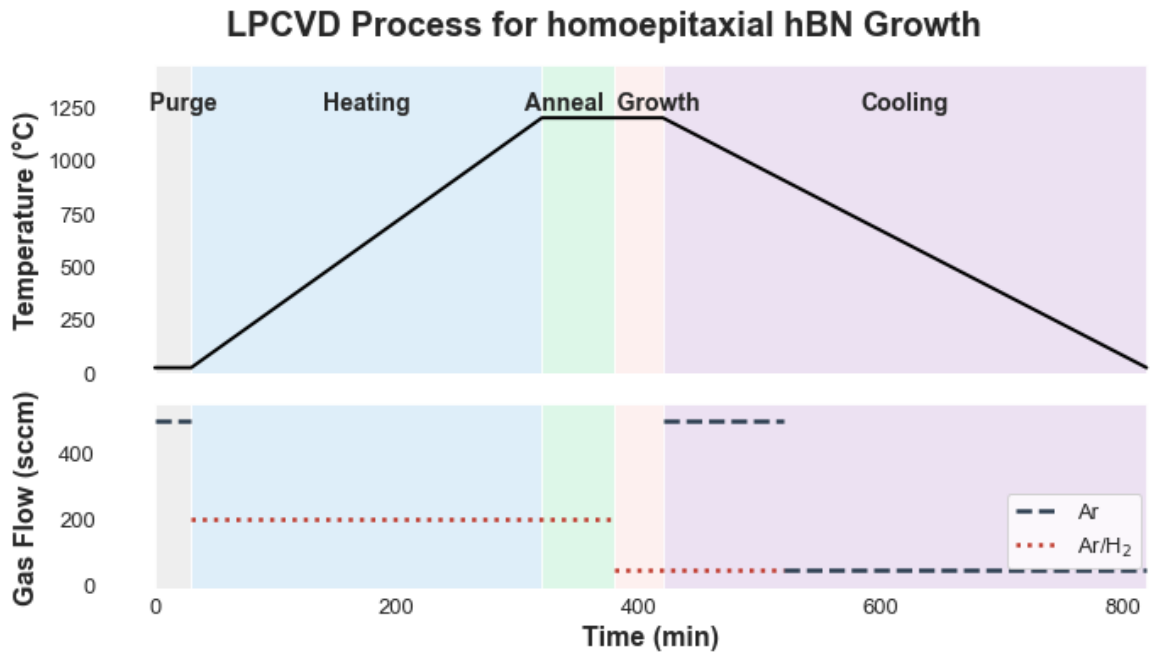

Figure 4.2: LPCVD schedule for homoepitaxial hBN on 295 nm SiO_2/Si. *Shaded regions denote purging, heating, annealing, growth, and cooling stages.*

Growth was conducted in the same horizontal tube furnace configuration described in Chapter 3, with modifications to target homoepitaxial rather than catalytic nucleation growth. The furnace temperature was ramped to 1200 °C at a heating rate of 4 °C min^{-1} under a continuous flow of carrier gases. Throughout the growth process, the total gas flow was maintained at 300 sccm (Ar/H_2 mixture), and no metallic catalyst was introduced, allowing the exfoliated hBN flakes to act as their own crystallographic seed. The precursor supply (based on thermally decomposing ammonia borane) was held at a fixed temperature of approx. 93 °C to ensure a stable boron–nitrogen chemical flux during growth. The growth was carried out for approximately 40 mins to allow full deposition of hBN on the sample surface.

Following growth, the furnace was cooled to room temperature under the same carrier gas atmosphere at ~4 °C min^{-1} to minimise thermally induced strain gradients across the flake. The resulting samples were removed from the quartz tube once cooled and immediately characterised to avoid ambient adsorption effects. Structural and optical analysis was performed on the same flake regions before and after growth to ensure direct comparison, as detailed in the subsequent Results section.

Raman spectroscopy: Vibrational modes of hBN were characterised using a Renishaw inVia confocal Raman system with a 633 nm excitation laser. Calibration was performed with a silicon reference at 520 cm^{-1}. The characteristic E_2g phonon mode was fitted with a Lorentzian profile to extract peak position and FWHM, providing information on crystalline quality after transfer onto SiO_2 substrates. [177–179] Full details of the setup are described in Section 3.2.2.

Atomic Force Microscopy (AFM): Nanoscale surface features of the hBN films were characterised using a Veeco Dimension 3100 AFM operating in tapping mode. [183–185] The system employed a silicon cantilever with a nominal tip radius of 8 nm (MikroMasch, CSC17/Ti-Pt). High-resolution topographical images were obtained with a scan resolution of 512 × 512 pixels. The data were analysed using Nanoscope Analysis 1.5 software to extract key surface parameters, including step height and surface roughness. Roughness was expressed in terms of average deviation (R_a) and root-mean-square average (R_q) of surface height variations. [183]

Scanning Electron Microscopy (SEM): The morphology of transferred hBN films on Si/SiO_2 substrates was studied using SEM. [186] Imaging was conducted on a Zeiss Supra 55 VP microscope, which provided high-resolution images that enabled assessment of surface uniformity and film continuity.

Photoluminescence (PL) spectroscopy: Single-photon emitter properties were investigated using a confocal microscope excited with a continuous-wave 532 nm laser. Emission was spectrally filtered and directed either to a spectrometer for spectral acquisition or to a Hanbury Brown–Twiss interferometer with APDs for photon correlation and lifetime measurements.[187–195] The second-order autocorrelation function, $g^2(\tau)$, was evaluated to confirm single-photon emission. Additional details of the PL setup can be found in Section 3.2.2.

4.4 Results

To assess the sensitivity of homoepitaxial growth to the underlying support, an initial series of experiments used exfoliated hBN flakes on Si/SiO_2 with a 90 nm oxide. Although

this thickness is frequently employed for optical identification of two-dimensional materials, it proved inadequate under the present high-temperature LPCVD conditions. During the 1200 °C process the thin oxide partially densified and was vulnerable to hydrogen-assisted etching, which destabilised the hBN–SiO_2 interface and prevented coherent layer-by-layer overgrowth.

Post-growth SEM imaging (Figure 4.3) shows non-uniform, mottled contrast across the flake interiors together with irregular edges and occasional wedge-like lifting. These features are not consistent with grain boundaries or domain stitching; rather, they indicate nanoscale topography changes associated with local oxide loss, interfacial voiding and relaxation of in-plane stress. In several regions the terrace pattern visible prior to growth is disrupted, and step continuity is lost, implying that terrace-mediated propagation could not be sustained on the compromised substrate. The combined evidence supports the following interpretation. First, at temperatures above 1000 °C, thin SiO_2 layers compact and shrink, generating shear at the hBN/oxide boundary. Second, in an Ar/H_2 ambient, even modest hydrogen activity can etch amorphous SiO_2 and any carbonaceous residues left by exfoliation, producing pits and undercut regions beneath the flakes. The coupling of thermal compaction and chemical thinning explains the observed contrast pattern and partial delamination. As a consequence, the growth did not proceed homoepitaxially; instead, it produced a roughened surface with poor adhesion and disrupted terraces, conditions that are incompatible with stable optical emitter formation and reproducible spectroscopy.

This failed attempt establishes a practical requirement for the remainder of the study. A thicker oxide provides the thermal and chemical buffering needed to preserve interface integrity during high-temperature LPCVD. Increasing the oxide thickness to 295 nm, which

is used for all successful samples reported later in this chapter, prevents undercutting and maintains step continuity so that the overlayer can inherit the crystallographic order of the seed flake.

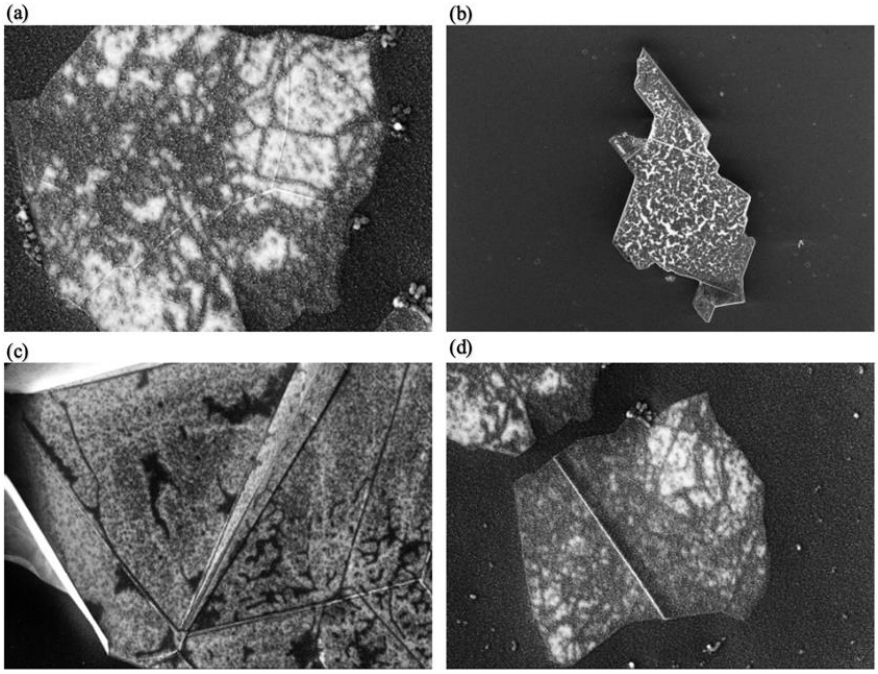

Figure 4.3: SEM images of exfoliated hBN flakes on 90 nm SiO_2/Si following an attempted homoepitaxial LPCVD growth at 1200 °C. *SEM images (a)- (d) show wide-area views revealing mottled contrast across the flake interiors and irregular edges, it highlights disrupted step morphology and regions of apparent undercut or partial delamination. The 90 nm oxide does not provide sufficient thermal and chemical buffering under these conditions, leading to hydrogen-assisted oxide thinning and interfacial instability.*

The morphology of the exfoliated hBN flakes before and after homoepitaxial growth was first examined using optical microscopy and atomic force microscopy (AFM). Optical imaging provided an overview of flake geometry and thickness contrast, while AFM offered nanometre-scale information on surface roughness and step structure. *Figure 4.4 (a)* shows a representative exfoliated hBN flake on a SiO_2/Si substrate with a 295 nm oxide layer, selected for its large lateral dimensions and smooth surface. The enhanced optical contrast

afforded by the oxide thickness facilitated precise identification of flake boundaries and thickness uniformity prior to growth.

The AFM map of the pristine flake *Figure 4.4 (b)* reveals a clean, atomically flat surface with distinct step terraces. These steps, typically 0.33–0.4 nm in height, correspond to individual hBN monolayers, confirming the high crystalline quality of the exfoliated material. Such flat terraces are essential for achieving coherent epitaxial overgrowth, as they provide low-energy pathways for adatom migration and attachment.

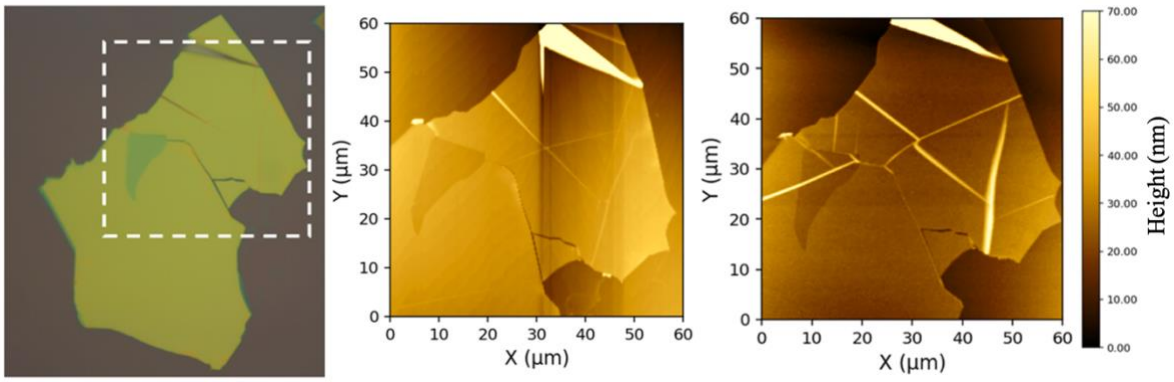

Figure 4.4: Optical and atomic force microscopy (AFM) characterization of exfoliated hBN flakes before and after homoepitaxial growth. *(a) Optical image of a representative exfoliated hBN flake on a SiO_2/Si substrate (295 nm oxide), with the white dashed region indicating the scanned AFM area. (b) AFM topography of the pristine flake prior to growth, exhibiting atomically flat terraces and step edges typical of mechanically exfoliated hBN. (c) AFM map acquired after homoepitaxial growth, revealing additional terraces and uniform height modulation across the surface, consistent with continuous overlayer formation and step-flow growth.*

After homoepitaxial growth *Figure 4.4(c)*, the AFM topography remains smooth and continuous, with a marginal increase in step height and a subtle change in overall surface contrast. These features indicate that the growth proceeded via a layer-by-layer mechanism rather than through island nucleation. The absence of grain boundaries or abrupt step

discontinuities suggests that the newly deposited hBN maintains registry with the underlying flake lattice, consistent with homoepitaxial alignment. The uniformity of the height profile also confirms that precursor adsorption and surface diffusion were well balanced across the flake, leading to a conformal film rather than thickness gradients.

These observations highlight the critical role of substrate cleanliness and surface energy in promoting epitaxial continuity. Since the exfoliated hBN presents an atomically inert and lattice-matched surface, it provides an ideal template for adatom incorporation, resulting in coherent overlayer formation without significant interfacial strain.

Raman spectroscopy and scanning electron microscopy (SEM) were employed to evaluate the crystalline structure and lattice integrity before and after growth. The Raman spectra in *Figure 4.5 (a)* display the characteristic E_2g in-plane vibrational mode near 1366 cm^{-1} for both the pristine (blue) and overgrown (red) flakes. A small shift in the E_2g peak position is observed after growth, indicating subtle changes in the local strain or lattice environment. The full width at half maximum (FWHM) also increases slightly from 8.2 cm^{-1} to 9.0 cm^{-1} following growth consistent with minor broadening due to the introduction of additional layers or strain relaxation during the homoepitaxial process.

This subtle broadening can be attributed to slight strain variations or thickness fluctuations within the newly deposited hBN layer. The small shift in the peak position further suggests a minor relaxation of lattice strain following overgrowth. Importantly, no additional vibrational features were observed, indicating that the epitaxial process did not introduce chemical impurities or structural disorder. The overall similarity between the pristine and overgrown Raman profiles confirms that the homoepitaxial interface remains highly coherent, with well-preserved crystal quality and minimal defect incorporation.

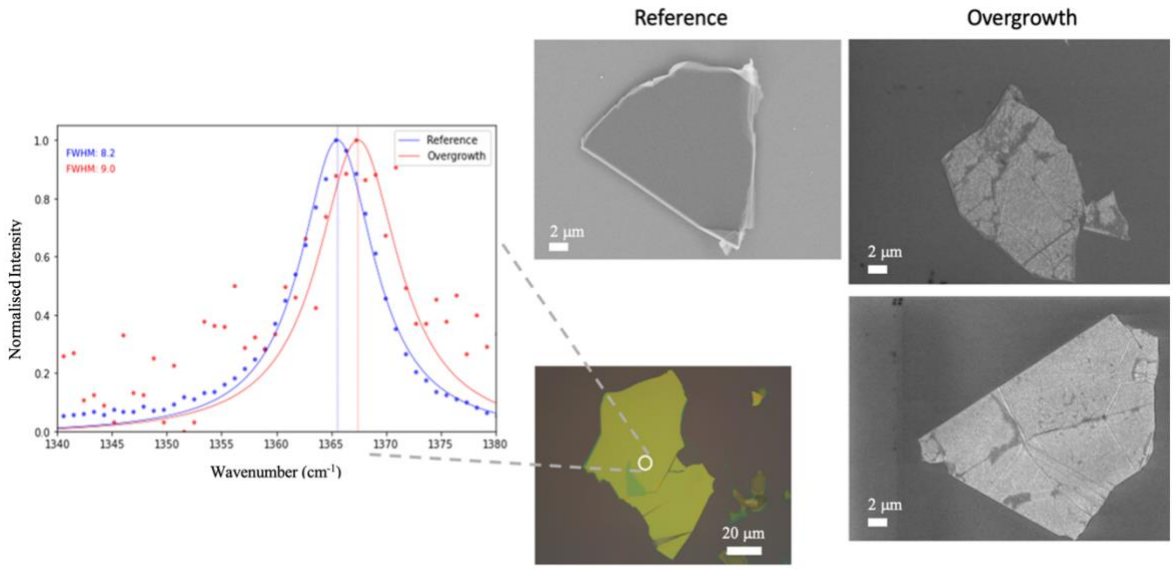

Figure 4.5: Raman spectroscopy and scanning electron microscopy (SEM) of exfoliated hBN flakes before and after homoepitaxial growth. *(a) Raman spectra comparing the pristine (reference) and overgrown hBN, showing the characteristic E_2g phonon mode near 1366 cm^{-1}. The FWHM increases slightly from 8.2 cm^{-1} to 9.0 cm^{-1} after growth, indicating minor strain and thickness variations while preserving the crystalline order. (b) SEM image of the pristine flake (left- Reference) displaying a smooth, well-defined morphology, after homoepitaxial overgrowth (right- Overgrowth).*

SEM imaging provides complementary evidence of structural continuity. The pristine flake *Figure 4.5 (b- left)* shows well-defined edges and uniform contrast, typical of mechanically exfoliated hBN. After overgrowth *Figures 4.5 (b- right)*, the same regions exhibit consistent surface morphology without signs of delamination or irregular nucleation. The smooth texture and lack of secondary grains corroborate the AFM findings and confirm that the epitaxial film extends laterally across the entire flake surface.

Together, the Raman and SEM analyses demonstrate that homoepitaxial hBN growth proceeds with excellent structural preservation. The minimal FWHM change suggests low strain accumulation, while the morphological uniformity observed in SEM indicates a continuous crystalline interface. These results collectively confirm that the growth

mechanism maintains the intrinsic crystalline quality of the underlying flake while enabling controlled layer extension.

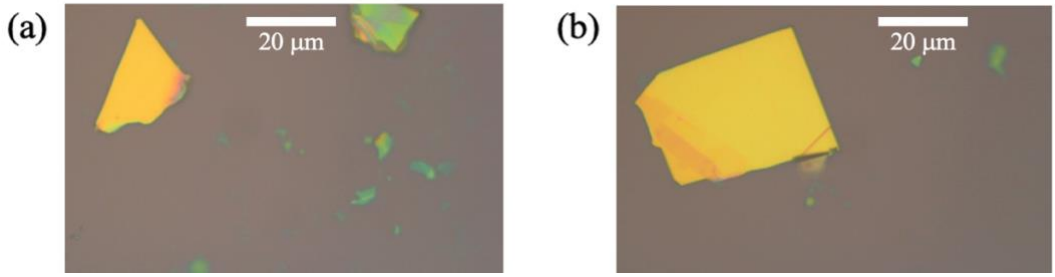

Figure 4.6: Optical images of two representative exfoliated hBN flakes, *selected from the many flakes measured across the samples. These are the same two flakes shown in Figures 4.7 and 4.8.*

The optical images presented in *Figure 4.6 (a-b)* show two representatives exfoliated hBN flakes selected from a larger population measured across multiple substrates. These flakes were chosen because they exhibited large lateral dimensions, well-defined terrace edges, and minimal visible creasing or folding, allowing reliable spatial correlation between pre- and post-growth optical and spectroscopic mapping. The use of the 295 nm SiO_2 substrate provides strong optical contrast, enabling clear identification of flake boundaries and thickness variations prior to growth. These same regions were subsequently mapped by photoluminescence (PL) imaging both before and after homoepitaxial deposition, ensuring that observed changes in optical response can be directly attributed to the growth process and not to variations in flake geometry, illumination conditions or measurement position.

Before growth, the PL signal across the exfoliated hBN flakes (Figure 4.7) is relatively weak and spatially uniform, consistent with the optical behaviour expected for thin exfoliated hBN in which the emission is dominated by intrinsic excitonic recombination. This regime is characterised by broad visible luminescence without strong spectral substructure, reflecting a low density of optically active defect states. The uniformity of the PL intensity in the pre-

growth maps indicates that the flakes are structurally intact, free of strong localised nonradiative quenching sites, and exhibit minimal thickness variation across the imaged area.

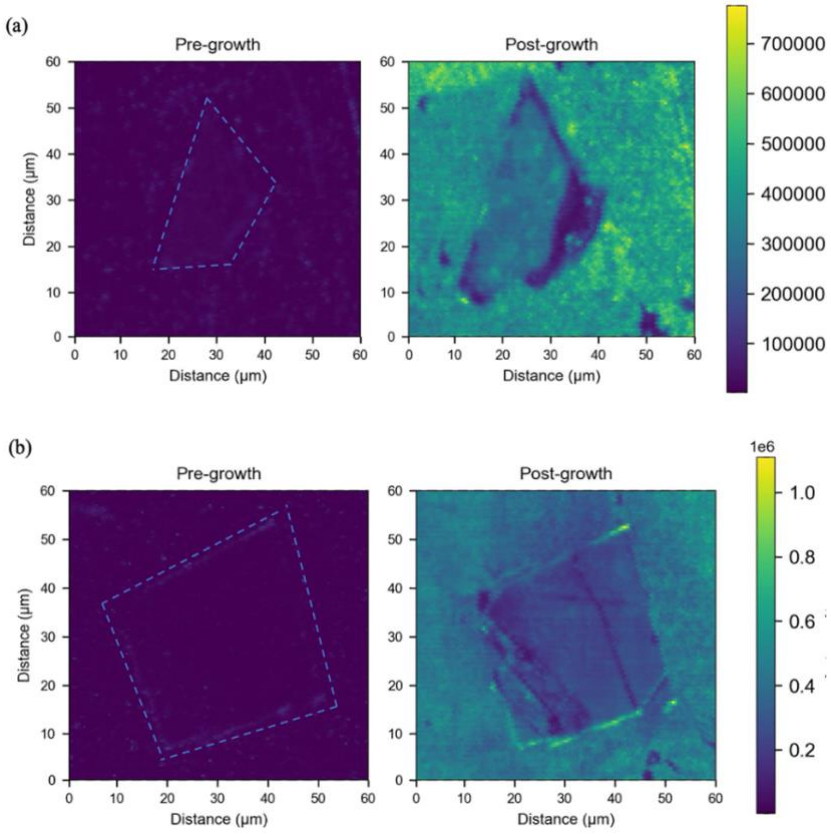

Figure 4.7: Photoluminescence intensity maps of the same two flakes before homoepitaxial growth, showing weak, largely uniform emission typical of pristine hBN. *These maps serve as the baseline, after growth the same regions exhibit a clear upward shift in per-pixel counts and higher peak intensities across the maps.*

The absence of pronounced bright or dark features suggests that the exfoliation procedure and surface preparation (including UV exposure to remove residual tape contamination) produced flakes with clean surfaces and stable optical behaviour suitable for homoepitaxial overgrowth.

Following homoepitaxial LPCVD growth, the optical response of the flakes' changes significantly, as shown in *Figure 4.7*. The PL intensity increases across the mapped areas,

and the spatial distribution of the emission becomes more structured, with clear regions of increased brightness. These brighter domains are attributed to slight local increases in film thickness or small variations in strain introduced during the growth process. Homoepitaxial growth proceeds by terrace propagation across the parent flake, and small differences in terrace nucleation rate or step-flow mobility can lead to thickness variations on the scale of one to a few hBN layers. Because hBN exhibits interference-enhanced luminescence on SiO_2 substrates, even sub-nanometre differences in thickness can translate into measurable differences in PL intensity. Similarly, residual strain introduced during heating, growth and cooling is known to modify excitonic recombination pathways, producing modest but detectable spatial variation in luminescence amplitude. The emergence of spatial contrast in the PL maps therefore reflects a combination of morphological and strain-related modifications induced during epitaxy.

The PL spectra recorded from the same flakes *Figure 4.8* before and after growth further support this interpretation. Both the pristine and overgrown regions display broad visible emission characteristic of hBN, without the appearance of new narrow sub-bandgap peaks. The absence of new bands is a key indicator that the homoepitaxial process does not introduce new optically active point defects with distinct energy levels; in particular, it suggests that vacancy complexes, substitutional impurities, or deep-level centres were not significantly formed during growth. Instead, the spectral envelope after growth shows an overall increase in integrated intensity and a mild broadening of the main emission band. These spectral changes are consistent with the formation of a slightly thicker hBN layer, which increases optical absorption and modulates cavity-like interference conditions at the hBN/SiO_2 interface. In addition, the improved crystalline continuity afforded by homoepitaxial alignment enhances radiative recombination rates by reducing the density of

nonradiative quenching sites such as edge defects, step discontinuities or interfacial disorder. Thus, the PL enhancement does not indicate the creation of new emissive states, but rather the strengthening of the intrinsic excitonic emission already present.

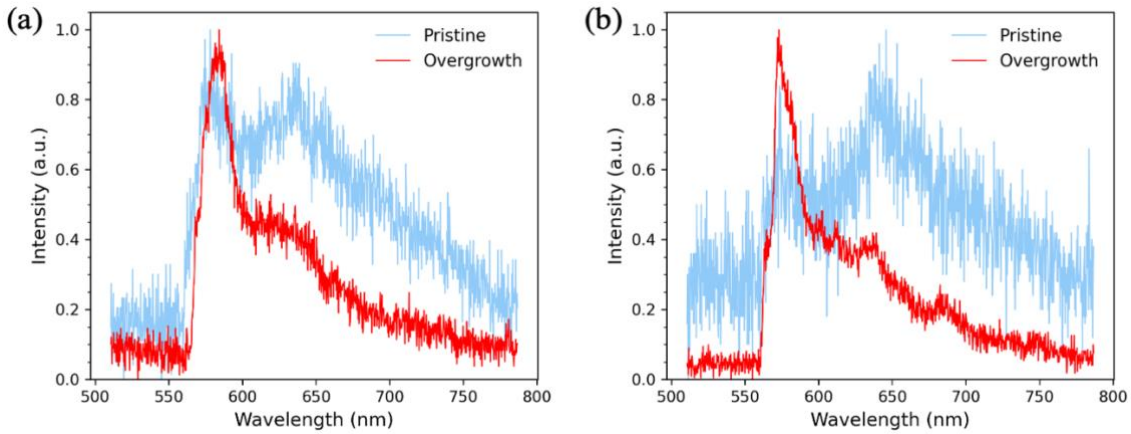

Figure 4.8: Photoluminescence of the same two flakes after homoepitaxial growth. *The PL spectra show enhanced emission, with higher integrated intensity (pristine, blue; overgrowth, red) post growth.*

The combined changes in PL intensity, spatial contrast and spectral line shape therefore serve as optical signatures of successful homoepitaxial growth. The results demonstrate that the overlayer inherits the atomic registry of the parent flake, maintaining the coherent arrangement of the hexagonal lattice. The emergence of mild spatial variation in emission reflects local strain relaxation and sub-layer thickness variations rather than structural degradation. The continuity of luminescence across the flake further confirms that no significant delamination or interfacial voiding occurred during growth, in strong contrast to the behaviour observed on substrates with insufficient oxide thickness, as described earlier in this chapter. Together, these findings indicate that the 295 nm SiO_2 substrate provides adequate mechanical and chemical stability to support homoepitaxial overgrowth at high temperature, allowing the flake and overlayer to expand and cool without introducing cracks, voids or optical quenching sites.

The interpretation of these results gains additional significance when considered alongside the AFM and Raman characterisation. AFM measurements show that the terraces remain continuous after growth, with only slight increases in step height consistent with layer-by-layer deposition. Raman spectra display a narrow E_2g phonon mode with only a minor increase in FWHM (8.2 to 9.0 cm^{-1}), indicating that strain and disorder remain low and that the crystallinity of the homoepitaxial layer closely matches that of the underlying flake. SEM imaging confirms that no new secondary grains or surface roughening occurs in the supported regions. These structural probes verify that the PL enhancements are not artifacts of surface damage, contamination or uncontrolled defect formation, but rather reflect true improvements in optical response arising from coherent structural extension.

Taken together, the optical analysis of Figures 4.6, 4.7 and 4.8 provides strong evidence that homoepitaxial growth on exfoliated hBN templates produces continuous, high-quality films that preserve the intrinsic excitonic emission properties of hBN while increasing overall radiative efficiency. The ability to enhance photoluminescence without inducing new defect states is especially important for quantum photonics applications, where environmental stability and emitter spectral purity are critical. These results support the broader conclusion that homoepitaxial growth enables deterministic tuning of hBN film thickness and strain environment while maintaining structural coherence, thereby offering a scalable and robust route toward engineered optical functionality in two-dimensional material systems.

4.5 Conclusion

This chapter has demonstrated that homoepitaxial LPCVD growth on exfoliated hBN flakes supported by a sufficiently thick SiO_2 buffer layer provides a reliable route to extend the crystalline lattice of hBN while preserving its intrinsic optical response. By using mechanically exfoliated hBN as the growth template, the overlayer inherits the atomic registry and terrace structure of the underlying flake, allowing the growth process to proceed via step-flow propagation rather than nucleation-driven island formation. Structural characterisation by AFM, SEM and Raman spectroscopy confirmed that the epitaxial films maintain low levels of strain and disorder, with only a modest broadening of the E_2g phonon mode (8.2 to ~9.0 cm^{-1}) consistent with slight thickness variation rather than defect incorporation. Crucially, the experiments also revealed the importance of substrate oxide thickness: flakes supported on 90 nm SiO_2 underwent interfacial instability and surface etching during high-temperature growth, whereas those on 295 nm SiO_2 retained terrace continuity and interlayer adhesion throughout the process.

Photoluminescence mapping and spectroscopy provided further evidence of successful homoepitaxy. The same flake regions measured before and after growth exhibited a clear increase in integrated PL intensity without the emergence of new sub-bandgap emission features, indicating that the epitaxial process does not generate additional optically active defects. Instead, the enhanced emission and emergence of mild spatial contrast were attributed to layer-by-layer thickness increase and local strain relaxation, both of which modify exciton recombination efficiency and interference conditions at the hBN/SiO_2 interface. The ability to enhance photoluminescence while maintaining the intrinsic broad excitonic character of the emission demonstrates that the homoepitaxial layer is structurally coherent and free from optically detrimental impurities.

Taken together, these results establish homoepitaxy as a robust strategy for producing high-quality, thickness-controlled hBN films suitable for optical and quantum photonic applications. The method provides a means to modulate optical response through controlled thickness and strain while avoiding the formation of new deep-level defect states. The findings of this chapter therefore form a foundation for the work that follows, in which the focus shifts from maintaining pristine excitonic emission to tailoring, activating and characterising discrete atomic defect centers for deterministic single-photon emission in engineered hBN platforms. In addition, the ability to achieve high-quality, thickness-controlled homoepitaxial layers provides a promising route for integrating quantum emitters with hBN-based photonic structures, such as waveguides, enabling guided single-photon emission for future on-chip quantum photonic devices.

5

Coupling Spin Defects in a Layered Material to Nanoscale Plasmonic Cavities

This chapter investigates the coupling of negatively charged boron vacancy (V_B^-) defects in hexagonal boron nitride (hBN) to nanoscale plasmonic gap cavities. The study aims to enhance the weak optical emission typically observed from these spin defects by leveraging strong near-field confinement within metal–dielectric–metal nanocavities.

The preceding chapters of this thesis established hexagonal boron nitride (hBN) as a robust two-dimensional host for quantum photonics, beginning with methods to grow, transfer, and cleanly integrate few-layer films. Chapter 3 developed growth and transfer protocols that preserve crystalline quality and yield thickness control at the few-nanometre level, a requirement later leveraged for device integration. Chapter 4 mapped the optical response of as-prepared and overgrown flakes and analysed how thickness, strain, and local environment govern excitonic and defect-related emission. In Chapter 5, I will introduce deterministic V_B^- creation by focused ion beam irradiation, and quantified room-temperature

photoluminescence, excited-state lifetimes, and optically detected magnetic resonance (ODMR) contrast from these spin-active centres. Together, these results positioned hBN as a practical platform for room-temperature single-photon generation and spin readout. Yet, they also exposed a central limitation for deploying V_B^- centres in devices: the emission is intrinsically dim because non-radiative channels dominate over radiative decay, suppressing photon rates and constraining ODMR contrast and sensing sensitivity.

This chapter addresses that limitation by introducing plasmonic nanocavities as an application-oriented bridge between the materials and defect engineering developed earlier and functional quantum nanophotonic devices. By coupling V_B^- centres to strongly confined optical modes in plasmonic gap cavities, we aim to simultaneously increase brightness, shorten lifetimes and improve ODMR signal-to-background, thereby directly enhancing device-level figures of merit from single-photon flux to spin readout sensitivity.

This work was published in *Advanced Materials* (2021), where I contributed equally as first author alongside Noah Mendelson. My role included optimising the FIB irradiation dose, assembling the plasmonic cavity structures, performing optical and magnetic characterisation and analysing the resulting data. Cavity simulations and electromagnetic modelling were carried out in collaboration with our partners specialising in nanophotonic design, Prof. Strauf's group. The results demonstrate a scalable approach for significantly improving the emission efficiency of V_B^- centres in hBN and highlight their potential for future quantum photonics and nanoscale sensing applications.

5.1 Abstract

Spin defects in hBN, particularly V_B^- centers, have emerged as promising candidates for quantum sensing. However, their inherently low quantum efficiency results in weak photoluminescence. In this work, we present a scalable method to enhance their emission by coupling them to plasmonic gap cavities consisting of a flat gold mirror and a silver nanocube separated by a few-layer hBN spacer.

This configuration enables two orders of magnitude enhancement in PL intensity and a corresponding twofold increase in ODMR contrast. Such improvements stem from strong light confinement and Purcell enhancement within the nanogap. This study establishes a foundation for developing quantum nanophotonic architectures based on 2D materials with controllable spin–plasmon interactions.

5.2 Introduction

Hexagonal boron nitride (hBN) has gained attention as a versatile platform for nanophotonics and quantum technologies. Its wide bandgap (~6 eV) chemical stability and compatibility with 2D heterostructures make it ideal for hosting deep-level fluorescent centers. These centers can function as room-temperature single-photon emitters, enabling applications in quantum sensing, imaging, and information processing.

Among the known defects in hBN, the negatively charged boron vacancy (V_B^-) is of particular interest due to its spin-active triplet ground state, with a zero-field splitting of approximately 3.5 GHz. Its optical transitions near 850 nm and spin-selective intersystem crossing allow optical initialization and readout of spin states. *Figure 5.1(a)* shows the atomic structure of a V_B^- defect, while *Figure 5.1(b)* depicts its energy-level diagram. *Figures 5.1(c–*

d) illustrate its optical properties, broad near-infrared PL centred around 850 nm with temperature dependent lifetimes (1.73 ns at 300 K and 3.80 ns at 4 K), indicative of reduced non-radiative recombination at cryogenic conditions. Importantly, these defects can be deterministically created using neutron irradiation, laser ablation or focused ion beam (FIB) techniques, enabling reproducible fabrication and integration into nanodevices. However, their low radiative efficiency remains a major bottleneck for practical deployment.

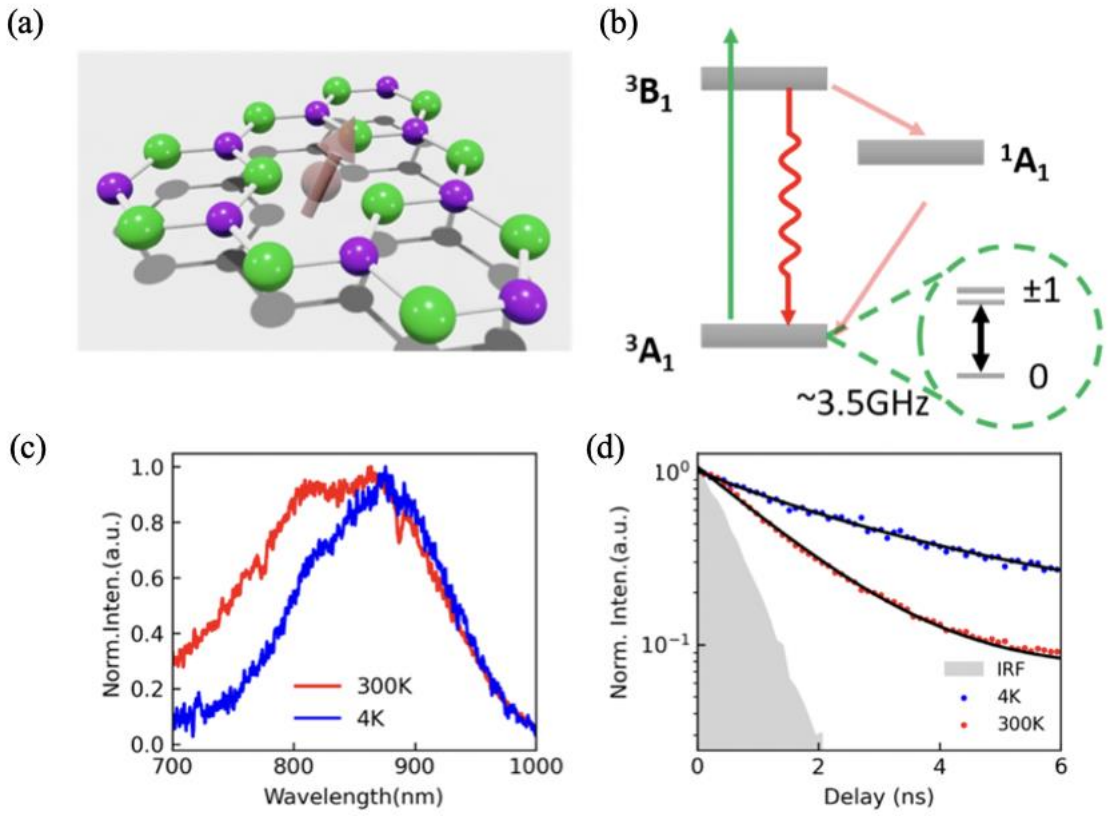

Figure 5.1. *(a) Three-dimensional illustration of the boron vacancy (V_B-) in hBN, with boron and nitrogen atoms depicted as purple and green spheres, respectively. The vacancy resembles a single electron system in a solid material associated with a spin, which can be optically read out. (b) Level structure of the V_B-. (c) Normalized PL spectra of hBN V_B- vacancy at 300K (red) and 4 K (blue). (d) Time-resolved PL spectra of V_B- at 300K (red) and 4K (blue). The extracted lifetime values are 1.73 ns and 3.80 ns, respectively. The instrument response function (IRF) is shaded in grey, yielding an IRF of 0.77 ns.*

At the spin level, the V_B^- centre is described by an S = 1 triplet ground state with sublevels $|m_S = 0\rangle$ and $|m_S = \pm1\rangle$ split by the axial zero-field splitting parameter D ≈ 3.5 GHz and a smaller transverse parameter E arising from local strain and symmetry breaking. In the absence of a magnetic field, $|m_S = \pm1\rangle$ remain nearly degenerate however, an external field lifts this degeneracy through the Zeeman interaction and allows frequency-selective addressing of each transition. Under off-resonant optical excitation, the defect cycles between its triplet ground and excited states, with some population diverted through spin dependent intersystem crossing pathways into metastable singlet levels. The $|m_S = 0\rangle$ state couples weakly to these non-radiative channels than the $|m_S = \pm1\rangle$ states, and therefore emits more fluorescence. Continuous optical pumping gradually drives the system into the brighter $|m_S = 0\rangle$ state, creating a PL signal that depends on the spin projection. This spin-dependent brightness underpins optically detected magnetic resonance (ODMR).

A brief physical picture clarifies why plasmonic environments are well matched to hBN emitters. Plasmonic studies how light couples to collective oscillations of conduction electrons at metal–dielectric interfaces. At a planar interface, these collective modes form surface plasmon polaritons with electromagnetic fields confined to the vicinity of the metal surface. In metallic nanoparticles, the finite size and boundary conditions lead to localized surface plasmon resonances (LSPRs), in which the conduction electrons oscillate collectively against the positive ion background. These resonances occur at discrete frequencies whose values are set by the particle geometry, the metal's dielectric function and the surrounding medium.[111, 212] The resulting optical modes exhibit deeply sub-wavelength localization, with effective mode volumes far below those achievable in dielectric resonators. When a metallic nanoparticle is placed above a metal mirror and separated by a nm-scale dielectric spacer, the electromagnetic fields of the particle and its mirror image hybridise to form a gap mode

tightly confined to the spacer region. From an electrodynamics perspective, this hybridization can be viewed as a strongly coupled antenna–mirror system in which the induced charges on the particle and the mirror face each other across the gap. The normal component of the electric field becomes strongly enhanced in the dielectric spacer, and the spatial extent of the mode in all three dimensions is compressed to the order of the gap thickness and particle footprint.

Because the optical energy is squeezed into a very small volume, the electric field amplitude within the gap rises sharply and the optical mode volume V is reduced. In the language of cavity quantum electrodynamics, the local density of optical states experienced by an emitter is enhanced, and the Purcell factor governing spontaneous-emission acceleration scales approximately as $F_P \propto Q/V$ for an emitter on resonance with a cavity of quality factor Q.[213] Even for modest- Q plasmonic modes, the ultrasmall V attainable in gap cavities can therefore produce very large F_P. More microscopically, the presence of the metallic nanocavity modifies the photonic environment so that the total decay rate τ of an emitter decomposes into enhanced radiative (τ_r) and non-radiative (τ_{nr}) channels, with τ_r boosted by the strong coupling to radiative gap modes and τ_{nr} associated with energy transfer into lossy electron–hole excitations in the metal. Whereas dielectric microcavities achieve large Q but only moderate confinement, plasmonic gap cavities invert this trade-off as they deliver extreme confinement and therefore large radiative-rate enhancement over a broad spectral bandwidth, a particularly attractive attribute for broadband defect emission.

These general advantages align unusually well with the structural and optical properties of hBN. First, few-layer hBN flakes naturally provide spacer thicknesses in the 3 - 15 nm range, which is precisely the regime where gap modes exhibit maximal confinement

without incurring excessive ohmic damping. This obviates the need for depositing polymer spacers or atomic-layer-deposited dielectrics to define the gap and allows the same crystalline film that hosts the emitter to set the cavity dimension with nanometre precision. Second, the emission spectrum of V_B^- centres span a broad near-infrared band, and plasmonic resonances are likewise broadband. This spectral complementarity eases resonance matching and reduces sensitivity to fabrication tolerances or thermal drift. Third, hBN is mechanically and chemically stable, non-fluorescent in the near-infrared and compatible with wet and dry transfer processes, so emitter placement into the gap region can be executed deterministically after defect creation without adding parasitic background or corrosion. Finally, the two-dimensional geometry of hBN simplifies spatial alignment, a flake can be translated and rotated until a desired portion straddles the hotspot under a nanocube, providing practical, high-yield integration pathways that are difficult to realise with 3D hosts.

While the conceptual role of plasmonic in boosting emission is broadly appreciated, the specific device architecture chosen for this work is crucial. We employ cube-on-mirror gap cavities in which a silver nanocube sits above a gold mirror, separated by an hBN spacer of controlled thickness. The cube edge and mirror plane form a capacitor-like geometry that concentrates optical fields into the gap at wavelengths tunable by the gap size and the cube dimension. Numerical simulations and prior experiments on molecular and solid-state emitters have shown that for gap sizes near 5 - 10 nm, the near-field intensity enhancement and Purcell factor can increase by more than an order of magnitude while maintaining radiative out-coupling pathways that collimate emission into the far field.[213,216,217] In practice, this means that the same geometry that accelerates emission also improves the fraction of emitted photons collected by a microscope objective, so brightness gains accumulate through both radiative-rate enhancement and extraction efficiency.

Real devices demand attention to materials choices and irreversible loss channels. Silver nanocubes are selected for their low loss and strong plasmonic response in the visible and near-infrared, but they are susceptible to surface sulfidation and oxidation. Gold mirrors provide chemical stability and reproducible film quality yet introduce a small spectral mismatch relative to silver. A thin alumina capping layer may be used on the gold surface to define a clean interface and suppress non-radiative quenching while still allowing intense field confinement in the hBN. Because the V_B^- dipole orientation in hBN lies predominantly in-plane, optimal coupling occurs when the local gap-mode field has a strong in-plane component at the emitter site; cube-on-mirror cavities naturally provide such a field at the cube edges. Spatial alignment therefore focuses on positioning V_B^- rich regions beneath those edges rather than the cube centre, a task that can be accomplished using dark-field imaging to locate cubes, followed by confocal mapping to identify coupled hotspots.

This device choice intersects naturally with the earlier chapters of the thesis. The transfer protocols validated in Chapter 3 ensure that flakes can be laminated onto evaporated gold films with minimal residue and controlled strain. The optical mapping methods of Chapter 4 allow us to identify flake regions with homogeneous baseline PL before integration, so that post-coupling enhancements can be attributed to cavity effects rather than thickness inhomogeneity. The defect-creation methods discussed in this chapter provide control over V_B^- density and charge stability, enabling us to tune the number of emitters inside a single gap and to balance ensemble brightness with inhomogeneous broadening. Because flake thickness was already measured by atomic force microscopy and optical contrast in those chapters, the same metrology supplies the key geometric parameter for the plasmonic device without additional processing.

The two geometries explored in this chapter are conventional and inverted which further broadened the design space and connect to the mechanical and optical considerations described previously. In the conventional sequence, a flake is transferred to the gold mirror first and cubes are subsequently dispersed, which maximises throughput and allows quick optical screening but offers limited control over the exact number of cubes per region. In the inverted sequence, cubes are positioned first, the hBN is laminated across them and finally an ultra-flat gold crystal is placed atop the stack. This creates a mechanically defined gap with atomically smooth top and bottom interfaces, reduces scattering losses associated with grainy evaporated films and can impose controlled strain near cube edges. That strain can activate otherwise dark emitters in hBN and modulate emission wavelengths, offering a second lever mechanical as well as electromagnetic for engineering the emitter–cavity interaction. Thus, the plasmonic integration in this chapter should be read not as an isolated topic but as the application layer that capitalises on growth, transfer and defect engineering developed earlier to realise a functional, high-brightness quantum emitter platform.

The performance targets for such devices can be phrased in quantitative terms that matter for sensing and spin readout. In continuous-wave ODMR, the shot-noise-limited sensitivity scales approximately as

$$\eta \propto 1/(C\sqrt{I})$$

where C is the ODMR contrast and I is the detected photon rate.[214] Operationally, ODMR is implemented by applying a microwave (MW) drive resonant with the $|m_S = 0\rangle \leftrightarrow |m_S = \pm 1\rangle$ transitions while continuously exciting the defect optically. When the MW frequency matches a spin transition, population is driven out of the bright $|m_S = 0\rangle$ state into the darker $|m_S = \pm 1\rangle$ manifold, increasing the probability of intersystem crossing into the metastable

singlet state and thereby reducing the detected PL intensity. The ODMR contrast C is defined as the relative PL change between off-resonant and on-resonant MW conditions and depends on the branching ratios of radiative and non-radiative decay channels, the efficiency of spin polarization and the MW Rabi frequency. In the time domain, pulsed ODMR sequences exploit coherent control of the spin to probe relaxation (T_1) and decoherence (T_2) times; in all cases the readout fidelity is limited by the number of photons collected per measurement window and by how strongly the spin state is encoded in the PL signal. If plasmonic coupling increases I by a factor of 15 and doubles C, the idealised improvement in η is roughly $\sqrt{15} \times 2 \approx 7.7$, even before considering the benefits of faster dynamics. In time-resolved protocols and pulsed readout, a reduced excited-state lifetime shortens the optical cycle time per readout, allowing more cycles within a fixed measurement window and therefore improved averaging. Provided that the intersystem crossing responsible for spin selectivity remains operative, faster cycles translate into more photons per unit time with preserved contrast. The broadband nature of the gap mode also ensures that enhancement is not confined to a single narrow spectral line but applies across the emission band, which is advantageous for defects whose zero-phonon lines are weak or thermally broadened at room temperature.

There are, of course, constraints that this chapter will quantify. When an emitter approaches a metal, non-radiative energy transfer into lossy electron–hole excitations can quench fluorescence if the separation is too small. The role of the hBN spacer is twofold: it centres the emitter within the high-field region, and it sets a minimum standoff distance from the metal to suppress quenching. Simulations show that for gaps below a few nanometres, the balance can tilt toward loss for gaps around 6 - 10 nm, the regime naturally provided by few-layer hBN—the balance favours enhancement, with radiative-rate increases of several-fold and only modest additional loss.[213,217] Likewise, heating from absorption in the metal can

broaden lines or alter charge states, but the thermal mass of the mirror and the pulsed or low-duty-cycle excitation used for lifetime measurements mitigate these effects. Cube size polydispersity broadens the scattering resonance distribution, yet the emitter's broad emission band ensures overlap with a significant fraction of devices even without post-fabrication tuning. For experiments requiring tighter spectral alignment, small adjustments in gap thickness attained by selecting flakes of slightly different thickness can shift the mode over tens of nanometres.

In summary, plasmonic appears here not as a separate subfield but as the application layer that activates the materials and defect physics established in this thesis. By funnelling optical energy into a nm - scale volume where V_B^- centres reside, plasmonic gap cavities convert weak, non-radiatively dominated emission into bright, rapidly cycling fluorescence with improved spin readout. The choice of cube-on-mirror geometry exploits hBN's unique advantages such as atomically thin, mechanically stable, broadband and non-fluorescent—while aligning with the metrology and processing practices already demonstrated.

The remainder of this chapter implements this strategy in two complementary device geometries (conventional and inverted gap cavities) quantifies brightness, lifetime and ODMR improvements, and benchmarks the measurements against simulations that connect gap thickness and field profiles to the observed enhancements. Results previewed here and elaborated in the following sections show order-of-magnitude photoluminescence enhancement, multi-fold lifetime reduction and approximately two-fold ODMR contrast improvement in both cavity stacks, validating plasmonic coupling as an effective and scalable approach to overcoming the brightness and readout limitations of V_B^- defects in hBN and

setting the stage for integrated quantum sensing and information processing with layered materials under practical ambient conditions.

5.3 Methodology

hBN irradiation for V_B^- defect creation: A silicon substrate with a thermal oxide layer of 90 nm was cleaned with acetone and isopropyl alcohol (IPA) via approximately 15 minutes of sonication in each solvent, respectively. Hexagonal boron nitride (hBN) flakes with thicknesses of ~ 10 nm and below were exfoliated onto these substrates using the scotch tape method. Ideal flakes were identified by measuring their thickness using atomic force microscopy (AFM). The flakes were further exposed to UV ozone to remove tape residues before focused ion beam (FIB) irradiation. FIB was then used to create boron vacancies in the target flake thickness. The system (Thermo Scientific Helios G4 Hydra) utilised a Nitrogen source with the beam current and energy of 1.9 pA and 30 keV respectively. The fluency used to create negatively charged boron vacancy was 1×10^{14} cm^{-2}. The irradiation box was patterned over the desired flake to create defects with dwell time of 25 ns. Finally, the irradiated flakes were transferred with the aid of poly (methyl meth acrylate) - PMMA to the target substrate.

Gold Plate Synthesis: First, high purity chloroauric acid was synthesized from pure metal. Concentrated (36%) hydrochloric acid (HCl) was placed in a pressure-equalizing dropping funnel and slowly added to a side-arm flask containing potassium permanganate ($KMnO_4$) (3g) on a stir plate to gradually generate chlorine gas (Cl_2). The resulting Cl_2 was passed through an airtight tube into a two-necked round-bottom flask containing 100 mL of MilliQ

water and one gold pellet (99.99% purity, 0.326 g). Any unreacted or excess Cl_2 passed through and was scrubbed by a third flask containing a solution of sodium thiosulfate ($Na_2S_2O_3$) (1.1 g) in water (50 ml). The reaction mixture was stirred at 60°C until the gold pellet had completely dissolved in the MilliQ water. The resulting solution was diluted to 200 ml in a volumetric flask with MilliQ water to yield a final stock solution of 8.28×10^{-3}M $HAuCl_4$.

Gold monocrystalline flake samples were then obtained using a modified Brust–Schiffrin method for colloidal gold synthesis via thermolysis. An aqueous solution of chloroauric acid ($HAuCl_4 \cdot 3H_2O$) at a concentration of 0.5 $gmol^{-1}$ was used as the precursor and mixed with a solution of tetraoctylammonium bromide (TOABr) in toluene. After stirring for 10 minutes at 5000 rpm, the mixture was left to rest for 10 mins, allowing the aqueous and organic phases to separate.

Simultaneously, the substrate was prepared by cleaning a silicon substrate with ultrasonication in acetone, isopropyl alcohol (IPA), and ultrapure water (MilliQ) for approximately 15 minutes in each solvent. After drying with nitrogen gas, the substrate was prebaked on a hot plate at 200°C for approximately 5 minutes for dehydration purposes. In the following step, a few microliters of the organic phase were drop-cast onto the substrate, which was then kept on the hot plate at 150°C for 1 hr. After that, the sample was cleaned in toluene at 75°C, followed by acetone and IPA.

Cavity Assembly: The silver cubes solution was bought from nanoComposix and diluted to 1% of its original concentration using ethanol. This diluted solution was then dispersed onto gold mirrors, which were prepared by gradually depositing 90 nm gold films onto clean silicon substrates via an electron beam evaporation system, followed by an atomic layer

deposition of 3 nm aluminium oxide. Further fabrication details are available in our previous work.

Photoluminescence Spectroscopy: The photoluminescence (PL) spectra were collected using a home-built scanning confocal microscope. The samples were excited with a continuous wave (CW) 532 nm laser. The reflection signal was spectrally filtered using a 532 nm dichroic mirror (LP03-532RE-25) and a 715 nm long pass filter. Time-correlated PL measurements were performed using the same setup, with the samples excited by a pulsed 512 nm laser (PiL051X) at a repetition rate of 20 MHz. The laser signal and the filtered PL from VB- defects (APD counts) were correlated using a time-correlated single-photon counting system (PicoHarp 300).

The results in Figure 5.1 (d) were obtained from Prof. Strauf's group, who used an avalanche photodiode (APD, Perkin Elmer) and a supercontinuum laser (NKT Photonics) to measure the lifetime. The APD has a jitter of 420 ps and the laser has a pulse width of 7 ps, resulting in an instrument response function (IRF) of 0.77 ns.

Scattering Spectroscopy: The scattering spectra were obtained using dark-field imaging in a separate home-built confocal microscope at room temperature. This setup employed a long working distance objective (Nikon CF Plan 50x EPI ELWD) with a numerical aperture (NA) of 0.55. White light illumination (Thorlabs OSL2) was directed through a multimode optical fiber and focused onto the sample at an incidence angle of 28° from the surface plane.

5.4 Results

V_B^- defects have a significant limitation due to their low brightness, caused by a high intrinsic non-radiative decay rate, this results in relatively low optically detected magnetic resonance (ODMR) contrast. To overcome the issue of low quantum yield, these emitters can be coupled to plasmonic cavities that enhance both excitation fields and emission rates. This approach has been successfully applied to enhance emission in various systems, including transition metal dichalcogenides and defects in solids. Given the broad emission spectrum of V_B^- defects, plasmonic gap cavities are an excellent solution for emission enhancement. Moreover, these cavities require a very thin medium (less than ~10 nm) to host the light source, making them particularly well-suited for layered materials like hBN. Plasmonic gap cavities also offer broad, tuneable resonance, extremely small mode volumes, straightforward nanofabrication techniques, and the ability to operate at room temperature.

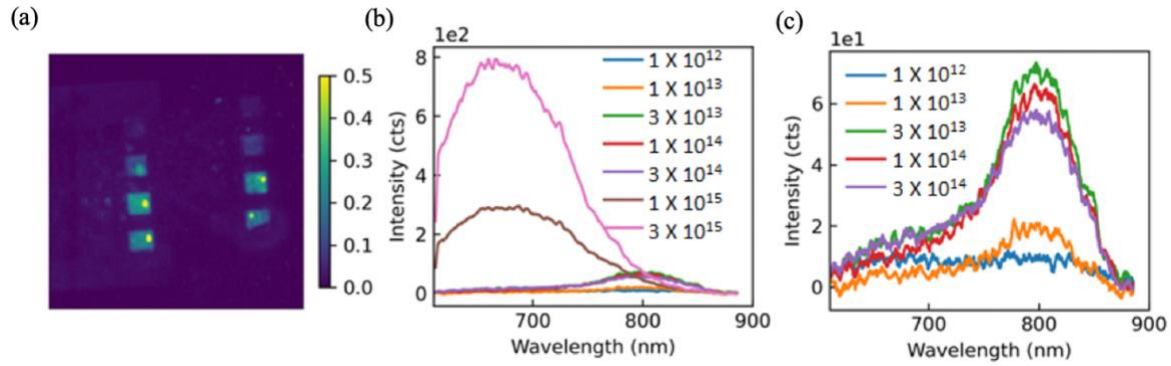

Figure 5.2 - Dose dependent photoluminescence data. *(a) PL map of irradiated samples with varying dosage boxes in the range 3×10^{15} cm^{-2} to 1×10^{10} cm^{-2}. The irradiation boxes visible in (a) correspond to dose $3\times10^{15}cm^{-2}$ (bottom) and 1×10^{14} cm^{-2} (top). (b) & (c) Dose dependent PL intensity of the irradiated hBN flake. Green PL spectra prove to be the optimum dose for V_B^- creation i.e., $3\times10^{13}cm^{-2}$.*

In this investigation, we showcase the coupling of a group of V_B^- emitters with a plasmonic gap cavity. This is achieved through a combination of a gold mirror and a silver

nanocube. We explore two complementary approaches to assess the impact of this setup: (1) transferring hBN onto a gold mirror and situating silver cubes atop the hBN layer, and (2) transferring hBN onto silver cubes and covering them with a synthetic ultra-flat gold mirror. Both techniques yield a substantial enhancement in photoluminescence (PL) emission from the V_B^- defect, accompanied by shortened fluorescence lifetimes and enhanced ODMR contrast. These findings lay a critical groundwork for further investigations into plasmon coupling with defects in 2D materials and will contribute to advancing quantum sensing utilizing this quantum spin system.

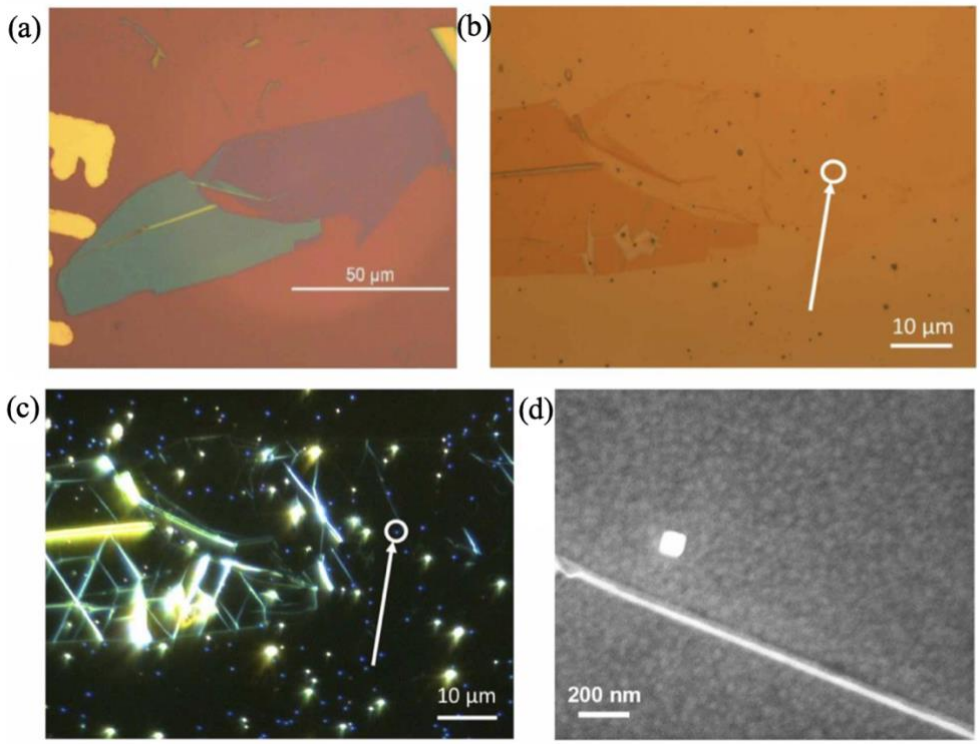

Figure 5.3 - SEM and Optical image of the flake and silver cube. *(a) Optical image of the exfoliated hBN flake on SiO_2 substrate. (b) Optical image of the transferred hBN flake covered with silver cubes on the gold surface. Spot marked by the circle with an arrow point to the silver cube. (c) Dark field image of the flake with silver cubes (bright spots) on top. (d) SEM image of the silver cube marked in (c) & (d).*

A nitrogen ion beam was used to irradiate the hBN flake and to knock out boron atoms to create V_B^- defects in the lattice. To efficiently generate a high density of V_B^- defects with high intensity and minimal damage to the flake, we tested a series of doses. Twelve patterned boxes (1μm×1μm) were irradiated with varying doses (3×10^{15}, 1×10^{15}, 3×10^{14}, … 1×10^{10} cm^{-2}) to determine the optimal conditions. It was challenging to identify fluences of 3×10^{11} cm^{-2} and below and no V_B^- defects were evident from the results. Initially, the trend suggested that V_B^- creation was proportional to the dose, but as the dose approached 1×10^{14} cm^{-2}, significant carbon deposition occurred, which quenched the emission from V_B^- defects.

A thin hBN flake was exfoliated onto a SiO_2 substrate using scotch tape. To remove any tape residue, the flake was cleaned in UV-ozone for about 10 minutes. *Figure 5.3 (a)* presents an optical image of the flake on the SiO_2 substrate before irradiation. Next, the flake was irradiated with a nitrogen ion beam at a fluence of 3×10^{14} cm^{-2} to generate V_B^- defects in the lattice. After irradiation, the flake was transferred to a gold substrate using PMMA. A diluted solution of silver cubes (from nanoComposix) was then dispersed on the gold substrate, covering the flake surface. *Figures 5.3 (b) and 5.3 (c)* show bright-field and dark-field images of the flake, with the silver cube position marked by a white circle for cavity data analysis. Lastly, Figure 3(d) provides an SEM image confirming the presence and geometry of the silver cube.

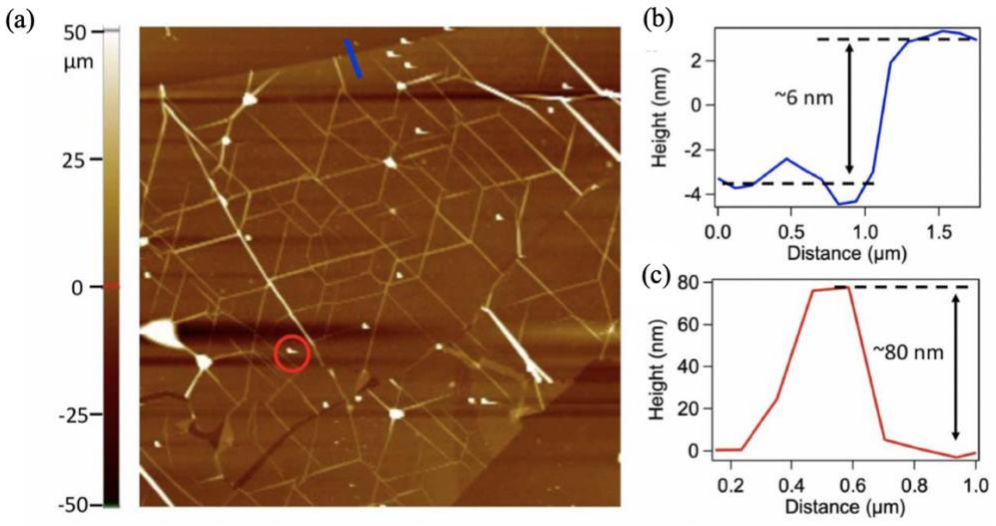

Figure 5.4 - Thickness of the flake in the target area. *(a) AFM (atomic force microscopy) image of the flake obtained with non—contact mode. Blue arrow on top left indicates the area used to find the flake thickness, the target silver cube is marked with a red circle. (b) Flake thickness is measured to be approximately 6 nm by the AFM. (c) Height of the silver cube as seen from the graph is approximately 80 nm.*

Non-contact mode AFM was used to generate the image presented in *Figure 5.4 (a)*, which shows the target flake area. The bright spots in the scan are identified as silver cubes or cube clusters. The specific site used for further cavity experiments is marked with a red circle. The blue arrow at the top of the image indicates the spot where the thickness of the flake was measured. According to *Figure 5.4 (b)*, the flake's thickness is estimated to be 6 nm. The height of the cube, measured for simulations and calculations related to enhancement, is approximately 80 nm, as shown in *Figure 5.4 (c)*.

The general method of integrating plasmonic gap cavities with V_B^- defects is depicted schematically in *Figure 5.5 (a)*. This plasmonic arrangement confines light within the gap between the nanocubes and the gold mirror, ensuring precise spatial alignment of the defects with the hot spot of the gap cavity. Such a cavity significantly enhances emission intensity by improving excitation efficiency, increasing emission rate, and focusing the radiation

pattern into a narrow range of the far field, thus enhancing collection efficiency. Our setup involved utilizing a nano plasmonic gap cavity comprising an ultra-flat gold mirror (~90 nm, coated with 2 nm Al_2O_3), hBN flakes with a thickness of ~8 nm (*Figure 5.4 (b)*), and a silver/gold nanocube (~100 nm edge length).

The resonance of this plasmonic gap cavity is broad, as illustrated by the scattering spectra in *Figure 5.5 (b)*, covering a spectral range from 600 to 850 nm with a peak emission at around 700 nm. The gap cavity system was further examined using finite-difference time-domain (FDTD) methods. The simulation included both the hBN layer (8 nm) and the Al_2O_3 layer (2 nm), with a vertically polarized dipole emitter positioned in the middle of the hBN layer. *Figure 5.5 (c)* presents a side view of the mode's electric field profile. The calculated

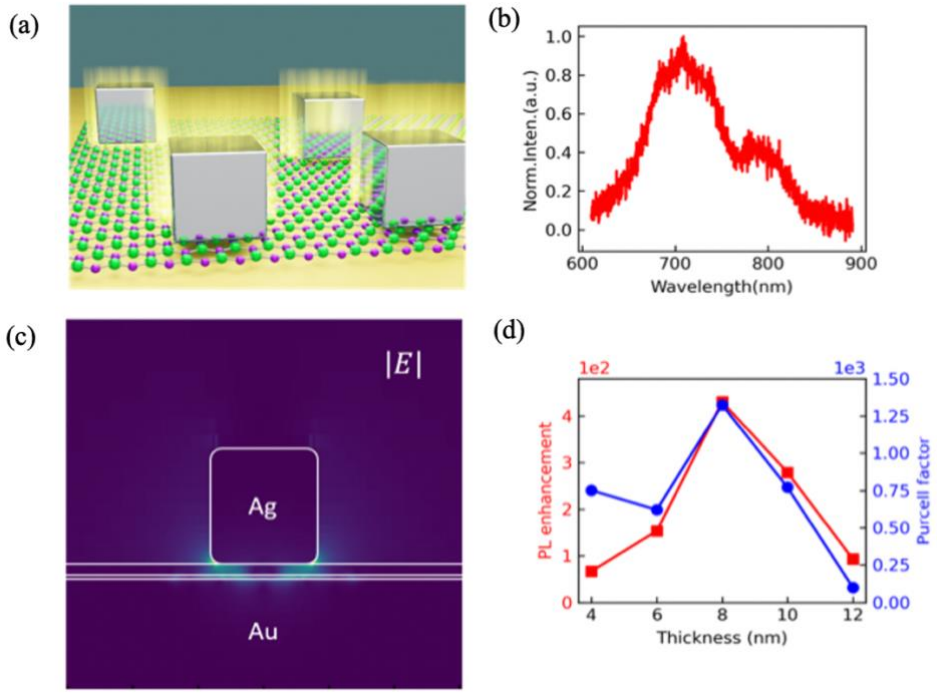

Figure 5.5 - Integration of V_B^- emitters in a plasmonic gap cavity. *(a) Schematic illustration of a nano cube-on-mirror plasmonic gap cavity. FIB-irradiated hBN flakes are positioned inside the gap to spatially match the cavity hot spot. (b) Experimental optical scattering spectrum of a single nanocavity. (c)*

Electric field profile for the gap cavity at λ = 800 nm with 2 nm Al2O3 and 8 nm hBN. (d) Calculated PL enhancement and Purcell factor versus hBN thickness.

photoluminescence (PL) enhancement and Purcell factors, as functions of gap thickness, are plotted in *Figure 5.5 (d)*, with the thickness ranging from 4 to 12 nm. Generally, the Purcell factor decreases with increasing gap size due to a larger mode volume. However, in this case, the resonance centered around 800 nm peaks at a gap thickness of approximately 8 nm, yielding the highest Purcell factor and maximum PL enhancement.

Comprehensive studies were performed to compare the emission from uncoupled (as-fabricated) V_B^- ensembles with those integrated into gap cavities using a home-built confocal optical microscope. *Figure 5.6 (a)* shows a side view of the sample configuration, while *Figure 5.6 (b)* presents a PL intensity map of the fabricated sample, with red spots indicating enhanced emission due to coupling with gap cavities. The white circle highlights the spot used to illustrate the system's characteristics. *Figure 5.6 (c)* compares the PL spectrum from this spot (coupled: blue) with the spectrum from the uncoupled V_B^- emission (red) taken from the same flake. The spectral peak height is about 17 times greater when the V_B^- ensemble is coupled to the plasmonic gap cavity. SEM and dark-field images of the sample (*Figure 5.3 (d)*) confirm that only one silver nanocube is present under the laser spot.

Plots of intensity measured as a function of excitation power for both cases are shown in *Figure 5.6 (d)*. The intensity was integrated from 715 to 900 nm, and the results were fitted using the following equation:

$$I = \frac{I_{sat} P}{(P + P_{sat})}$$

The fit parameters I_{sat} and P_{sat}, representing saturation intensity and power, respectively are determined as 0.184 and 2.497 MHz, and 7.738 and 8.825 mW for the uncoupled and coupled cases, respectively.

Across the investigated power range, the photoluminescence (PL) enhancement factor remains approximately 15, consistent with the previously measured example. This consistency is underscored by the observation that the PL intensity enhancement remains relatively stable throughout the power range, with only a minor variation in the saturation power attributed to coupling with a gap cavity. To identify the contributing enhancement factors, we conducted PL decay rate measurements, as illustrated in *Figure 5.6 (e)*. The lifetimes were found to be 1.80 ns for V_B^- on SiO_2 substrates, which reduced to 0.31 ns for a cavity-integrated ensemble. This reduction suggests that the decay rate increases by a factor of ~6 when the V_B^- emission is resonant with the cavity. This indicates that the observed emission enhancement consists of both excitation enhancement and emission enhancement via the Purcell effect, as will be discussed further.

Then, we measured the optically detected magnetic resonance (ODMR) spectra to assess the spin readout properties of the coupled system. A microwave field was applied using a copper wire (20 μm in diameter) positioned within 10 μm of the hBN flake. The PL counts were recorded as the microwave frequency was swept from 3.1 to 3.8 GHz. After integrating twenty-five ODMR spectra, the results are shown in *Figure 5.6 (f)*.

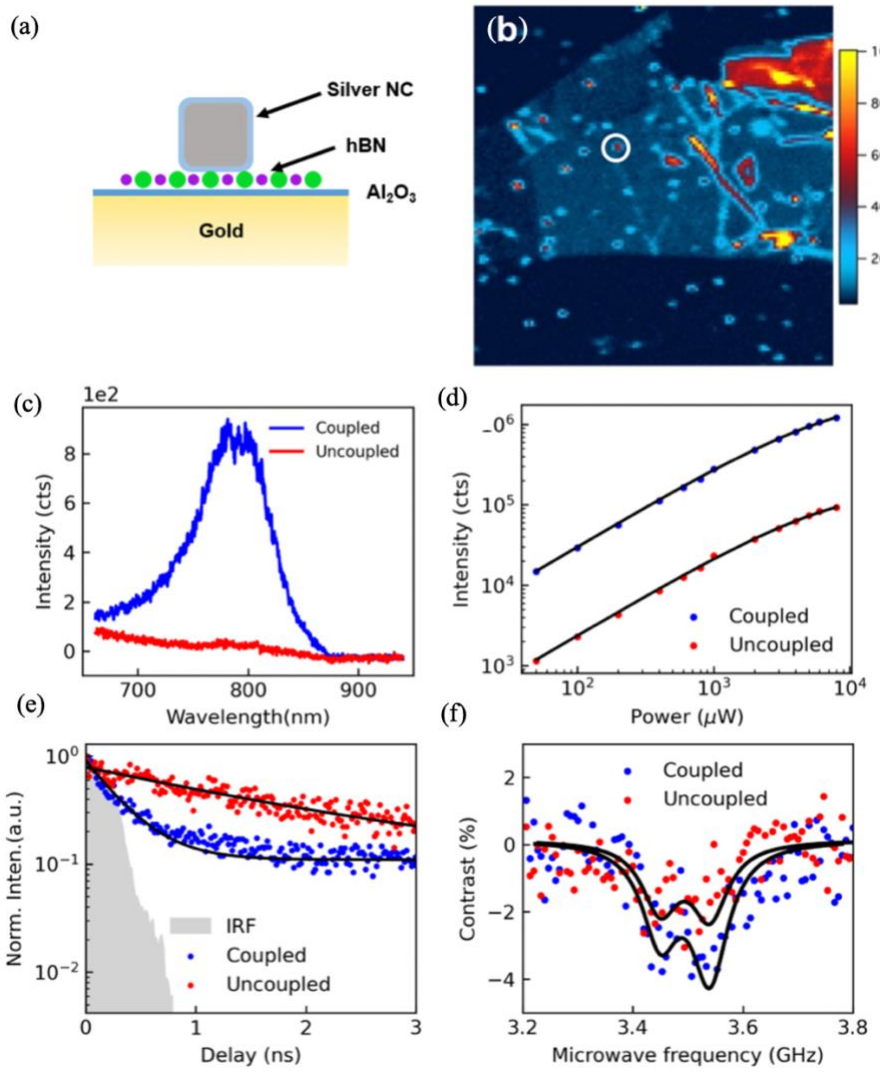

Figure 5.6 *- (a) Side-view illustration of the conventional gap plasmonic sample structure utilized. (b) Confocal PL intensity mapping (integrating from 715 to 900 nm) of the region of interest. The white circle highlights a spot where V_B^- is coupled in the plasmonic resonance. (c) PL spectra of V_B^- coupled (blue) and uncoupled (red) to the gap cavity. The sample is excited with a 532 nm CW laser. (d) Integrated PL intensity of the V_B^- as a function of excitation power. (e) Time-resolved PL spectra of V_B^- coupled (blue) and uncoupled (red) to the gap cavity. The extracted lifetime values are 0.31 and 1.80 ns, respectively. The instrument response function (IRF) is shaded in grey. (f) ODMR spectrum of the V_B^- coupled (blue) and uncoupled (red) to the gap cavity.*

Two dips at 3.45 and 3.55 GHz were detected for both the uncoupled and coupled V_B^- emissions, with the spectra fitted using two Lorentzian functions. Evidently, the PL emission

enhancement improves the signal-to-background ratio of the ODMR spectra; the ODMR signal from V_B^- in the cavity shows an optical contrast of 4.5%, compared to 2.5% for the pristine ensemble.

Following this, we investigate an alternative configuration of the plasmonic gap coupled system featuring an inverted geometry. This inverted structure is anticipated to selectively induce strain at the edges of the silver cubes, where the electric fields are particularly strong. In this configuration, it is possible to create strain-activated emitters from hBN and other transition metal dichalcogenides (TMDCs). Therefore, this geometry presents an avenue for additional investigation.

To fabricate these devices, silver nanocubes were initially drop-cast onto a glass coverslip with a thickness of 180 μm. Subsequently, thin hBN flakes were transferred onto the nanocubes and exposed to nitrogen irradiation to form V_B^- ensembles. Following this, the synthesized gold crystals were precisely aligned and transferred onto the hBN surface using a deterministic transfer technique, completing the cavity assembly. A schematic representation of the sample structure is provided as an inset in *Figure 5.7(a)*. For characterization of the V_B^- emitters in this setup, an inverted scanning optical microscope equipped with an oil-immersion objective (NA = 1.3) was employed.

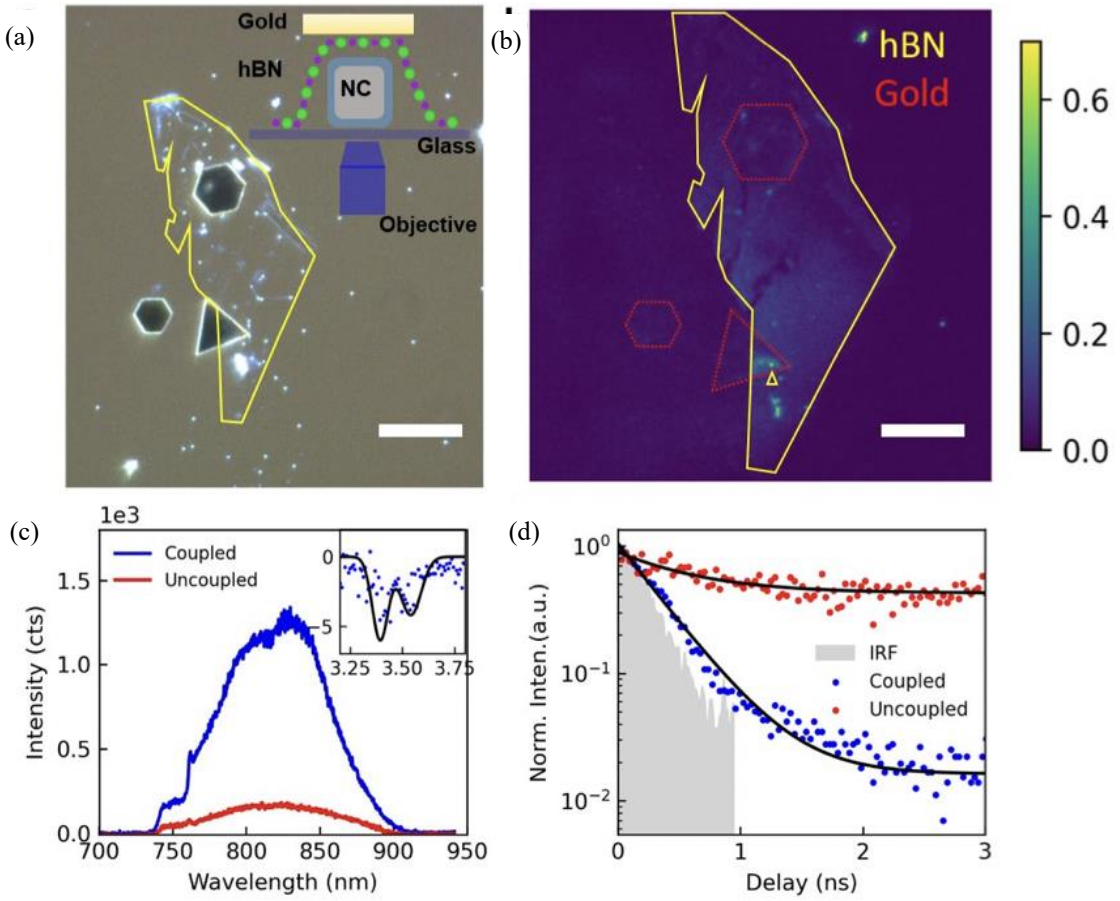

Figure 5.7 *- (a) Dark-field optical image of the fabricated hBN in gap plasmonic structures. The hBN flake, transferred onto a glass coverslip, is outlined in yellow. The black triangle and hexagons represent the ultra-flat gold crystals, while the white dots indicate the silver nanocubes. Inset: a side-view schematic of the inverted sample structure. (b) Confocal PL intensity map of the corresponding area. The yellow triangle points to a spot where V_B^- is coupled in the plasmonic resonance. Scale bar: 15 μm. (c) PL spectra of V_B^- on and off the gap cavity. Inset: ODMR spectrum of the V_B^- resonating with the plasmonic cavity. (d) Time-resolved PL spectra of V_B^- on and off the gap cavity. The extracted lifetime values are 0.56 and 1.30 ns, respectively. The instrument response function (IRF) is shaded in grey, yielding an IRF of 0.27 ns.*

Figure 5.7(a) displays a dark-field optical microscope image of the sample, where the bright spots correspond to the locations of the silver nanocubes, and the dark triangles and hexagons represent the gold crystals. Notably, a PL intensity map in *Figure 5.7 (b)* highlights an enhanced spot in the plasmonic gap cavity, denoted by a small yellow triangle.

The PL spectra obtained from the uncoupled (red) and coupled (blue) V_B^- ensembles are depicted in *Figure 5.7 (c)*. The peak height is enhanced by approximately 7-fold, while the peak position remains almost unchanged.

The inset in *Figure 5.7 (c)* displays an ODMR spectrum indicating an optical contrast of about 5%, which is comparable to that observed in the cavity-coupled V_B^- in the geometry shown in *Figure 5.6*. This level of contrast suggests that the enhancement originated from V_B^- coupled to the plasmonic gap cavity. The recorded lifetimes of 0.56 ns for cavity-coupled and 1.30 ns for uncoupled V_B^- illustrate a twofold enhancement in the emission rate *(Figure 5.6 (d))*.

5.5 Conclusion

We demonstrated that coupling V_B^- defect ensembles in hexagonal boron nitride to plasmonic gap cavities yields substantial improvements in optical brightness, emission dynamics, and spin readout at room temperature. By first optimising ion-irradiation dose to generate V_B^- centres and then integrating thin hBN flakes into cube on mirror, we observed order of magnitude photoluminescence enhancement, shortened fluorescence lifetimes indicative of Purcell-accelerated decay, and a marked increase in ODMR contrast relative to uncoupled ensembles.

Two complementary device geometries (i) hBN transferred onto a gold mirror before silver nanocube deposition and (ii) an inverted stack in which hBN overlays pre-positioned nanocubes and is capped by an ultra-flat gold crystal consistently produced enhancement while offering distinct advantages for field localisation and strain engineering. The combined measurements establish a practical pathway to room-temperature photonic control of V_B^-

defects, with the gap thickness of few-nanometre hBN emerging as a key parameter that balances mode volume, spectral overlap, and fabrication simplicity.

These results provide an experimentally grounded platform for advancing quantum sensing with 2D spin defects, and they motivate integration with deterministic positioning, active spectral tuning, and cavity-assisted microwave control to further amplify sensitivity and contrast in on-chip architectures. Together with scalable fabrication methods, these approaches could enable integrated devices for quantum sensing, spin photon interfaces, and on chip quantum photonic technologies.

6

Conclusion

This thesis has advanced the controlled generation, rigorous characterization, and photonic integration of single-photon emitters (SPEs) in hexagonal boron nitride (hBN). Through coordinated studies of growth kinetics, lattice continuity, impurity regulation, and cavity coupling, it establishes reproducible routes to bright, stable emission at room temperature and outlines viable interfaces to on-chip quantum photonics.

First, low-pressure CVD parameters like temperature, duration, and thermal ramps were systematically optimized to yield uniform, crystalline hBN films that host bright, stable SPEs, with spatial analyses clarifying chamber-environment and nucleation effects on defect incorporation (Chapter 3). Second, homoepitaxial overgrowth on exfoliated hBN established conditions for lattice continuity and showed how modest carbon incorporation governs spectral fingerprints, stability, and emitter spatial statistics, providing a practical lever for deterministic defect formation (Chapter 4).

Third, focused-ion-beam creation of spin-active V_B^- centers and their coupling to gap-mode plasmonic cavities enhanced light–matter interaction and photon extraction, indicating a feasible pathway toward device-grade spin–photon interfaces (Chapter 5).

Conclusion

Collectively, these results address two principal bottlenecks in room-temperature quantum photonics: controlled, scalable emitter formation in a technologically tractable two-dimensional host, and efficient photonic interfacing via nanocavity coupling. The demonstrated methodologies are compatible with wafer-level processing and support integration with resonant and guided-wave architectures relevant to quantum communication, sensing, and computation. Three constraints delimit current performance. The atomically resolved identification of all visible SPE species remains incomplete. Residual spectral diffusion and intermittency persist in select defect classes. Deterministic writing methods require further advances in throughput and placement precision to fully meet device-scale integration demands.

Correlative metrology that combines STEM, ODMR, and low-temperature spectroscopy should be pursued to unambiguously map structure–emission relationships. Engineered defect landscapes, using isotopic enrichment, controlled carbon/oxygen dosing, and strain or electrostatic fields, offer routes to tuning zero-phonon lines, phonon sidebands, and dephasing channels. Low-loss photonic platforms, hybrid dielectric–plasmonic or high-Q dielectric resonators are promising to achieve large Purcell enhancement with reduced optical loss. Electrically driven architectures, such as p–i–n or tunnelling devices, are a critical step toward compact, integrable quantum light sources. Wafer-scale, deterministic placement should be matured via mask-based implantation or laser writing with in-situ registration to photonic circuits and multiplexed optical readout. By coupling scalable materials engineering with precise photonic-environment design, this work positions hBN as a practical platform for room-temperature quantum photonics. The outlined directions, atomic-precision identification, spectral and coherence control, low-loss interfacing, and

electrical driving provide a clear trajectory from laboratory demonstrations to deployable quantum photonic subsystems.

Appendix

This appendix documents a structured-defect engineering workflow for activating single-photon emitters (SPEs) in hexagonal boron nitride (hBN) at predefined micron-scale locations. Patterned activation templates were fabricated and subsequently triggered to generate emitters with high spatial fidelity and reproducible optical signatures. My contribution comprised wide-field and scanning confocal photoluminescence (PL) measurements, spectral and lifetime analyses, and correlation between patterning parameters and emitter statistics. Across multiple flakes and devices, we quantify the relationships between template geometry and emitter yield, zero-phonon-line (ZPL) distributions, spectral-class clustering, lifetimes, polarization, and photostability. The results establish practical guidelines for reproducible, position-controlled activation of visible SPEs suitable for scalable integration.

This appendix supplements the main thesis by providing technical detail, extended data, and protocols referenced in Chapter 3 (growth window, calibration) and Chapter 4 (homoepitaxy on exfoliated hBN). It focuses on post-growth structured activation and device-scale optical characterization rather than repeating growth narratives.

Methodology

Material Growth: Hexagonal boron nitride (hBN) films were synthesized by chemical vapor deposition (CVD) using ammonia borane (AB, 97%) as precursor in a 1-inch quartz tube. Approximately 2 mg of AB was positioned ~32 cm upstream and heated independently during growth. Substrates were 15 × 15 mm copper foils with controlled carbon contents of 0.0005, 0.003, and 0.082 at.% (ICP-MS verified, Table A.1). Foils were deoxidized in acetic acid (5 min), rinsed in deionized water, and dried under argon; each foil was mounted on a tungsten support. The tube was purged in 250 sccm Ar (10 min), then heated to 1090 °C in 250 sccm Ar and 25 sccm H_2; the Cu was held molten for 10 min before AB activation at 90 °C for either 30 min (isolated domains) or 2.5 h (continuous films). Growth was terminated by switching off H_2 and the AB heater, followed by rapid Ar cooling. Brief Cu surface oxidation at 180 °C for 2 min enhanced optical contrast of grains prior to transfer.

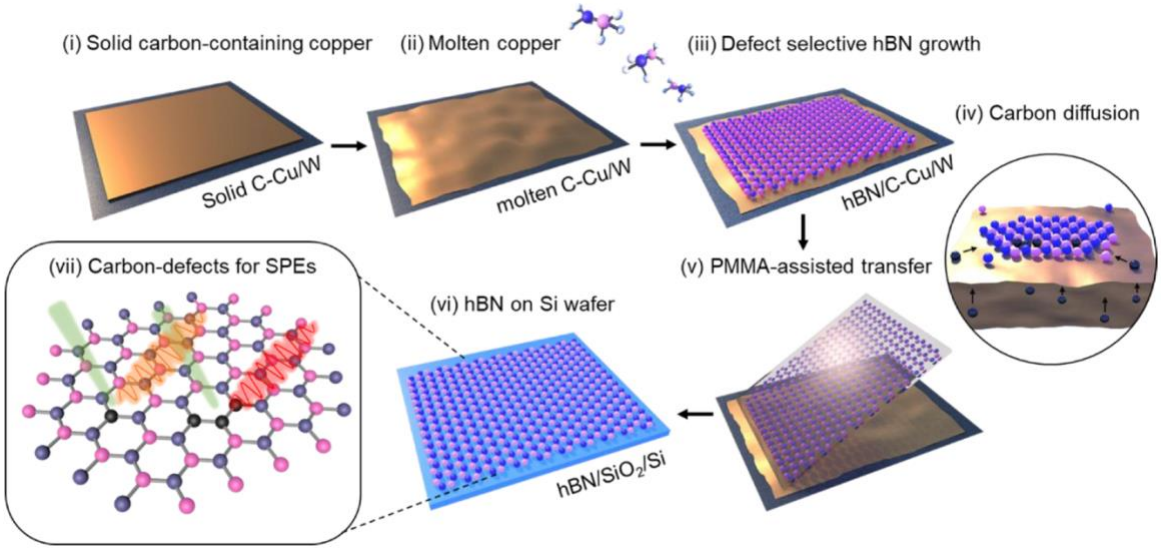

Figure A.1: Growth and transfer schematic for defect-selective hBN. *(a) C-Cu/W catalyst; (b) molten C-Cu/W; (c) hBN growth with defect-selective incorporation; (d) carbon diffusion into the lattice; (e) PMMA transfer; (f) hBN/SiO_2/Si; (g) carbon-related point defects acting as SPEs.*

Transfer of hBN Samples: The PMMA-assisted electrochemical delamination was used. PMMA was spin-coated (500 rpm, 10 s; 5000 rpm, 50 s), the hBN/Cu served as the cathode and Pt as the anode in 1 M NaOH at 5 V, releasing hBN/PMMA. After multiple deionized-water baths, the film was placed on 295 nm SiO_2/Si, baked at 75 °C for 5 min, and the PMMA was removed in 60 °C acetone for 1 h.

Characterization Techniques: The Optical microscopy and AFM quantified morphology and thickness; Raman (514 nm) verified the E_2g mode (~1366–1370 cm^{-1}, FWHM cited below). XPS and TEM (with SAED) confirmed bonding and crystallinity; TEM grids used the same bubble transfer followed by Ar anneal (350 °C, 3 h).

Photoluminescence Measurements: A scanning confocal platform (continuous-wave 532 nm, 100× NA 0.9) provided maps and point spectra. Emission passed a 532 nm dichroic and long-pass filter before fiber pinholing to avalanche photodiodes in a Hanbury-Brown and Twiss configuration for $g^2(\tau)$, or to a spectrometer for ZPL/PSB analysis. All data were acquired at room temperature unless stated. Wide-field imaging was used for rapid screening and registration to pattern templates.

Density Functional Theory (DFT) Calculations: Hybrid DFT (B3LYP/6-31G with D3 dispersion; TD-DFT for excitations) was used to compute candidate defect energetics and ZPL trends. The calculated band gap (5.77 eV) aligns with literature (5.7–6.1 eV). These calculations informed assignment of CB versus C_2B–CN spectral classes.

Results

Using carbon-engineered Cu foils spanning ~160 × in carbon content (0.0005→0.082 at.%), we reproducibly tuned dominant defect species. At low carbon, spectra were CB-like with ZPLs ~600–610 nm and narrower vibronic progressions; at high carbon, spectra shifted toward C_2B–CN with ZPLs ~630–640 nm and reshaped phonon sidebands. XPS showed monotonic increases in B–C and N–C bonding with substrate carbon, consistent with substitutional incorporation and a CB→C_2B–CN transition. Site-resolved fits revealed a monotonic ZPL red-shift and systematic PSB/ZPL evolution with carbon loading. Confocal PL maps showed increased density and brightness at 0.003 at.% before redistributing at 0.082 at.% as non-radiative disorder rose consistent with an optimum near intermediate carbon fractions for single-site isolation.

Table A.1: ICP-MS results for substrate carbon concentration used to program defect classes.

	S	O	C	Al	P	Cr	Fe	Ni	Zn	Ag	Sn	Sb	Pb	Bi
Cu #1	0.0010	0.0009	0.0005	0.0001	0.0014	0.0010	0.0011	0.0002	0.0001	0.0004	0.0003	<0.0000	0.0004	0.0001
Cu #2	0.0010	0.0010	0.0030	0.0001	0.0030	<0.0000	0.0032	0.0112	0.0055	0.0027	0.0133	0.0002	0.0010	0.0001
Cu #3	0.0009	0.0008	0.0820	0.0001	0.0036	<0.0000	0.0039	0.0136	0.0066	0.0029	0.0150	0.0002	0.0012	0.0001

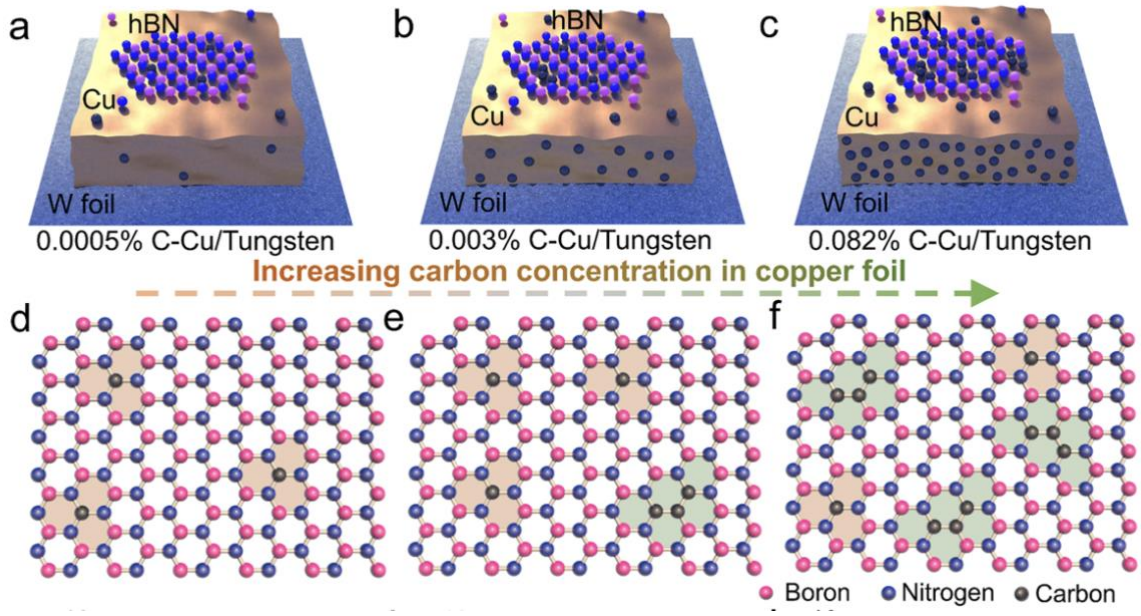

Figure A.2: Regulation of carbon-defect structures in hBN. *(a–c) Molten-Cu-mediated carbon delivery using 0.0005, 0.003, and 0.082 at.% C–Cu; (d–f) evolution from CB to C_2B–CN, consistent with XPS bonding fractions and optical shifts.*

The Micron-scale patterning constrained activation to predefined regions. Yield and uniformity improved relative to unpatterned controls, with ZPL statistics tighter within a given pattern class. The approach establishes a practical route to SPE arrays with designable pitch and emission bands, suitable for downstream photonics.

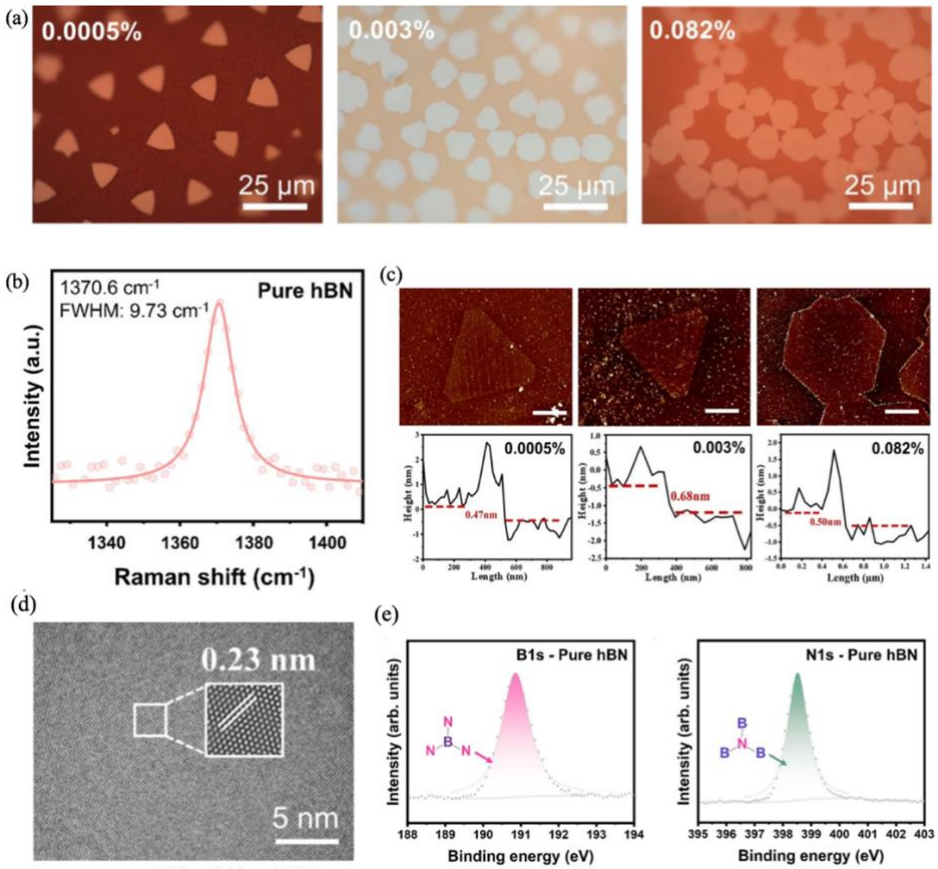

Figure A.3: Structural and morphological characterization of on 295 nm SiO_2/Si. *Optical micrograph, Raman E_2g at ~1370 cm^{-1} with narrow FWHM, AFM terraces (Rq ≈ 0.38 ± 0.06 nm), HRTEM lattice and SAED hexagonal symmetry, XPS B 1s/N 1s with minor C 1s.*

Representative $g^2(\tau)$ traces displayed clear antibunching dips; raw $g^2(0)$ occasionally did not pass below 0.5 due to background admixture from multi-site pickup at higher densities, room-temperature spectral diffusion and phonon broadening, residual substrate/wide-field fluorescence, and instrument timing limits (jitter, binning, dead time). After background correction and spectral windowing, the intrinsic values satisfy $g^2(0) < 0.5$ for single sites, consistent with single-photon emission and with the density-dependent trade-off observed in the maps.

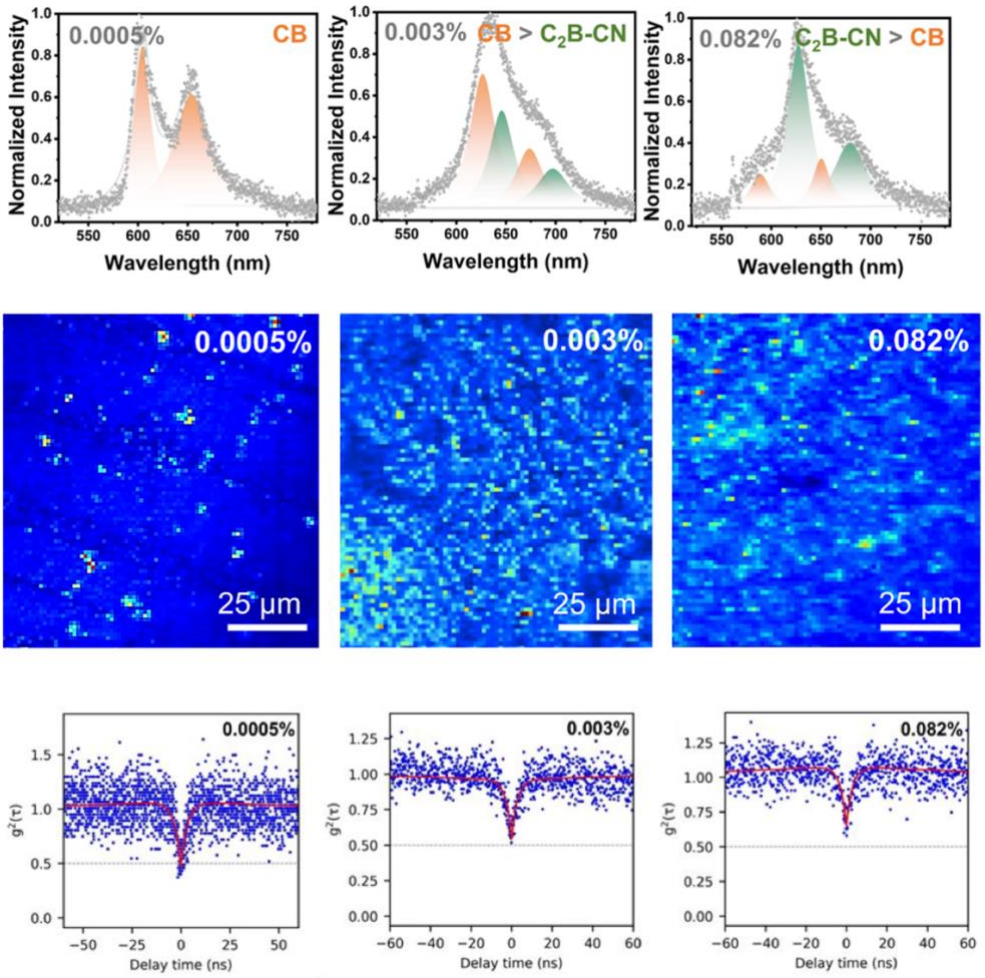

Figure A.4: Optical response versus substrate carbon. *top—room-temperature PL spectra showing ZPL shift from ~600–610 nm (CB-like) to ~630–640 nm (C_2B–CN-like) and PSB reshaping; middle—confocal PL maps (scale bars 25 μm) showing peak density and brightness increasing at 0.003 at.% and redistributing at 0.082 at.% ; bottom—representative $g^2(\tau)$ traces with antibunching dips; raw $g^2(0)$ limited by background and instrument factors, intrinsic $g^2(0) < 0.5$.*

Activation yield and optical purity are maximized at intermediate carbon loading, where bright-spot density is high enough for efficient screening but low enough to avoid multi-site pickup in a confocal spot. Clean transfer and polymer removal (warm acetone and Ar anneal) reduce background; narrow spectral windows and careful APD balancing deepen

the antibunching dip. For patterned activation, maintain consistent resist stacks and post-pattern cleans to avoid carbonaceous residues that broaden spectra.

Outlook

Room-temperature operation limits spectral purity via phonons and diffusion; encapsulation and cryogenic validation would sharpen ZPLs and improve $g^2(0)$. Atomic-scale correlation (STEM-EELS, super-resolution PL) will help unambiguously assign defect structures within a class. Integration with dielectric or plasmonic resonators near ~630 nm should increase brightness and extraction, enabling deterministic on-chip sources.

Bibliography

1. Rahmani, K., Mohammadi, S., & Danaie, M. (2021). Analytical investigation on the electro-optical characteristics of white graphene. *Journal of Computational Electronics*, *20*(5), 1860-1867.
2. Ali, T., Saadh, A. M., Biradar, R. C., Anguera, J., & Andújar, A. (2017). A miniaturized metamaterial slot antenna for wireless applications. *AEU – International Journal of Electronics and Communications, 82*, 368–382.
3. Jackman, J. A., Ferhan, A. R., & Cho, N. J. (2017). Nanoplasmonic sensors for biointerfacial science. *Chemical Society Reviews, 46*(12), 3615–3660.
4. Liu, J., & Hong, Z. (2018). Mechanically tunable dual frequency THz metamaterial filter. *Optics Communications, 426*, 598–601.
5. Nielsen, M. A., & Chuang, I. L. (2001). *Quantum computation and quantum information* (Vol. 2). Cambridge University Press.
6. Ladd, T. D., Jelezko, F., Laflamme, R., Nakamura, Y., Monroe, C., & O'Brien, J. L. (2010). Quantum computers. *Nature, 464*, 45–53.
7. Andersen, U. L., Neergaard-Nielsen, J. S., van Loock, P., & Furusawa, A. (2015). Hybrid quantum information processing. *Nature Physics, 11*, 713–719.
8. Lars, J. (2018). *The second quantum revolution: From entanglement to quantum computing and other super-technologies*. Springer International Publishing.
9. Gisin, N., Ribordy, G., Tittel, W., & Zbinden, H. (2002). Quantum cryptography. *Reviews of Modern Physics, 74*, 145–195.
10. Horodecki, R., Horodecki, P., Horodecki, M., & Horodecki, K. (2009). Quantum entanglement. *Reviews of Modern Physics, 81*, 865–942.
11. Scarani, V., Bechmann-Pasquinucci, H., Cerf, N. J., Dušek, M., Lütkenhaus, N., & Peev, M. (2009). The security of practical quantum key distribution. *Reviews of Modern Physics, 81*, 1301–1350.
12. Diamanti, E., Lo, H.-K., Qi, B., & Yuan, Z. (2016). Practical challenges in quantum key distribution. *npj Quantum Information, 2*, 16025.
13. Lehner, J., Leonhardt, U., & Paul, H. (1996). Unpolarized light: Classical and quantum states. *Physical Review A, 53*(4), 2727–2735.
14. Kolobov, M. I. (1999). The spatial behavior of nonclassical light. *Reviews of Modern Physics, 71*(5), 1539–1589.
15. Lounis, B., & Orrit, M. (2005). Single-photon sources. *Reports on Progress in Physics, 68*, 1129–1179.

16. Shields, A. J. (2007). Semiconductor quantum light sources. *Nature Photonics, 1*(4), 215–223.
17. Aharonovich, I., Englund, D., & Toth, M. (2016). Solid-state single-photon emitters. *Nature Photonics, 10*(10), 631–641.
18. Mittal, S., Goldschmidt, E. A., & Hafezi, M. (2018). A topological source of quantum light. *Nature, 561*(7724), 502–506.
19. Somaschi, N., Giesz, V., De Santis, L., Loredo, J. C., Almeida, M. P., Hornecker, G., Portalupi, S. L., Grange, T., Antón, C., Demory, J., Gómez, C., Sagnes, I., Lanzillotti-Kimura, N. D., Lemaitre, A., Auffèves, A., White, A. G., Lanco, L., & Senellart, P. (2016). Near-optimal single-photon sources in the solid state. *Nature Photonics, 10*(5), 340–345.
20. Ding, X., He, Y., Duan, Z.-C., Gregersen, N., Chen, M.-C., Unsleber, S., Maier, S., Schneider, C., Kamp, M., Höfling, S., Lu, C.-Y., & Pan, J.-W. (2016). On-demand single photons with high extraction efficiency and near-unity indistinguishability from a resonantly driven quantum dot in a micropillar. *Physical Review Letters, 116*(2), 020401.
21. Fox, A. M. (2006). *Quantum optics: An introduction* (Vol. 15). Oxford University Press.
22. FRS, D. R. (2018). *I don't understand quantum physics*.
23. Golub, R., Lamoreaux, S. K., & Lamoreaux, S. (2023). *The historical and physical foundations of quantum mechanics*. Oxford University Press.
24. Rosławska, A., Leon, C. C., Grewal, A., Merino, P., Kuhnke, K., & Kern, K. (2020). Atomic-scale dynamics probed by photon correlations. *ACS Nano, 14*(6), 6366–6375.
25. Böer, K. W., & Pohl, U. W. (2023). Excitons. In K. W. Böer & U. W. Pohl, *Semiconductor physics* (pp. 529–591).
26. Aßmann, M., & Bayer, M. (2012). Photon correlations in semiconductor nanostructures. In *Quantum optics with semiconductor nanostructures* (pp. 154–185). Woodhead Publishing.
27. Doherty, M. W., Manson, N. B., Delaney, P., Jelezko, F., Wrachtrup, J., & Hollenberg, L. C. (2013). The nitrogen-vacancy colour centre in diamond. *Physics Reports, 528*(1), 1–45.
28. Bradac, C., Gao, W., Forneris, J., Trusheim, M. E., & Aharonovich, I. (2019). Quantum nanophotonics with group IV defects in diamond. *Nature Communications, 10*, 5625.
29. Liu, X., & Hersam, M. C. (2019). 2D materials for quantum information science. *Nature Reviews Materials, 4*(10), 669–684.

30. He, X., Htoon, H., Doorn, S. K., Pernice, W. H. P., Pyatkov, F., Krupke, R., Jeantet, A., Chassagneux, Y., & Voisin, C. (2018). Carbon nanotubes as emerging quantum-light sources. *Nature Materials, 17*(8), 663–670.
31. Claudon, J., Bleuse, J., Malik, N. S., Bazin, M., Jaffrennou, P., Gregersen, N., Sauvan, C., Lalanne, P., & Gérard, J. M. (2010). A highly efficient single-photon source based on a quantum dot in a photonic nanowire. *Nature Photonics, 4*(3), 174–177.
32. Balmain, W. H. (1842). Observations on the formation of compounds of boron and silicon with nitrogen and certain metals. *The London, Edinburgh, and Dublin Philosophical Magazine and Journal of Science, 21*(138), 270–277.
33. Duan, X., et al. (2016). Review on the properties of hexagonal boron nitride matrix composite ceramics. *Journal of the European Ceramic Society, 36*(15), 3725–3737.
34. Song, L., Ci, L., Lu, H., Jin, C., Jariwala, D., Wu, D., Li, Y., Srivastava, A., Wang, Z., Storr, K., Balicas, L., Liu, F., Ajayan, P. M., & Lou, J. (2010). Large scale growth and characterization of atomic hexagonal boron nitride layers. *Nano Letters, 10*(8), 3209–3215.
35. Li, X., Wu, J., Guo, H, Wang, X., Zhang, G., & Zhang, Y. (2013). Exfoliation of hexagonal boron nitride by molten hydroxides. *Advanced Materials, 25*(15), 2200–2204.
36. Meng, Y., Liu, B., Mao, H.-K., Eng, P. J., Hu, M. Y., Chow, P., Shen, G., & Hemley, R. J. (2004). The formation of sp^3 bonding in compressed BN. *Nature Materials, 3*(2), 111–114.
37. Dai, S., Ma, Q., Andersen, T. I., McLeod, A. S., Fei, Z., Liu, M., Wagner, M., Watanabe, K., Taniguchi, T., Thiemens, M., Keilmann, F., Jarillo-Herrero, P., Fogler, M. M., & Basov, D. N. (2014). Tunable phonon polaritons in atomically thin van der Waals crystals of boron nitride. *Science, 343*(6175), 1125–1129.
38. Ci, L., Song, L., Jin, C., Jariwala, D., Wu, D., Li, Y., Srivastava, A., Wang, Z., Storr, K., Balicas, L., Liu, F., Ajayan, P. M., & Lou, J. (2010). Atomic layers of hybridized boron nitride and graphene domains. *Nature Materials, 9*(5), 430–435.
39. Zhang, X., Chen, J., Zhang, J., Wan, D., & Zhou, Y. (2015). High-temperature mechanical and thermal properties of h-BN/30 vol% Y_2SiO_5 composite. *Ceramics International, 41*(9), 10891–10896.
40. Lipp, A., Schwetz, K. A., & Hunold, K. (1989). Hexagonal boron nitride: Fabrication, properties and applications. *Journal of the European Ceramic Society, 5*(1), 3–9.
41. Constantinescu, G. C., Kuc, A., & Heine, T. (2013). Stacking in bulk and bilayer hexagonal boron nitride. *Physical Review Letters, 111*(3), 036104.

42. Liu, Z., Ma, L., Shi, G., Zhou, W., Gong, Y, Lei, S., Yang, X., Zhang, J., Yu, J., Hackenberg, K., Babakhani, A., Idrobo, J. C., Vajtai, R., & Ajayan, P. M. (2015). Direct observation of layer-stacking and oriented wrinkles in multilayer hexagonal boron nitride. *Nature Communications, 6*, 6099.
43. Pakdel, A., Bando, Y., & Golberg, D. (2014). Nano boron nitride flatland. *Chemical Society Reviews, 43*(3), 934–959.
44. Dean, C. R., Young, A. F., Meric, I., Lee, C., Wang, L., Sorgenfrei, S., Watanabe, K., Taniguchi, T., Kim, P., Shepard, K. L., & Hone, J. (2010). Boron nitride substrates for high-quality graphene electronics. *Nature Nanotechnology, 5*(10), 722–726.
45. Guo, Y., Gao, T., Xu, Z., Xu, Z., Zhao, J., Zhang, J., & Wu, J. (2022). Thermal conductivity of hexagonal boron nitride: A review. *Nano Today, 44*, 101512.
46. Geim, A. K., & Grigorieva, I. V. (2013). Van der Waals heterostructures. *Nature, 499*(7459), 419–426.
47. Han, W. Q., Wu, L., Zhu, Y., Watanabe, K., & Taniguchi, T. (2008). Exfoliation and characterization of single- and few-layer hexagonal boron nitride nanosheets. *Nano Letters, 8*(3), 902–907.
48. Watanabe, K., Taniguchi, T., & Kanda, H. (2004). Direct-bandgap properties and evidence for ultraviolet lasing of hexagonal boron nitride single crystal. *Nature Materials, 3*(6), 404–409.
49. Britnell, L., Gorbachev, R. V., Jalil, R., Belle, B. D., Schedin, F., Mishchenko, A., Georgiou, T., Katsnelson, M. I., Eaves, L., Morozov, S. V., Peres, N. M. R., Leist, J., Geim, A. K., Novoselov, K. S., & Ponomarenko, L. A. (2012). Field-effect tunneling transistor based on vertical graphene heterostructures. *Science, 335*(6071), 947–950.
50. Jo, I., Pettes, M. T., Kim, J., Watanabe, K., Taniguchi, T., Yao, Z., & Shi, L. (2013). Thermal conductivity and phonon transport in suspended few-layer hexagonal boron nitride. *Nano Letters, 13*(2), 550–554.
51. Wickramaratne, D., Weston, L. and Van de Walle, C.G., 2018. Monolayer to bulk properties of hexagonal boron nitride. *The Journal of Physical Chemistry C*, *122*(44), pp.25524-25529.
52. Cassabois, G., Valvin, P., & Gil, B. (2016). Hexagonal boron nitride is an indirect bandgap semiconductor. *Nature Photonics, 10*(4), 262–266.
53. Museur, L., Feldbach, E., & Kanaev, A. (2008). Defect-related photoluminescence of hexagonal boron nitride. *Journal of Applied Physics, 103*(10), 103520.
54. Edgar, J. H., Lin, J. Y., & Hoffman, T. (2021). Optical and excitonic properties of hexagonal boron nitride. *Comptes Rendus Physique, 22*(1–2), 69–76.

55. Arenal, R., Stephan, O., Cochon, J.-L., & Loiseau, A. (2007). Root-growth mechanism for single-walled boron nitride nanotubes in laser vaporization technique. *Journal of the American Chemical Society, 129*(51), 16183–16189.
56. Tran, T. T., Bray, K., Ford, M. J., Toth, M., & Aharonovich, I. (2016). Quantum emission from hexagonal boron nitride monolayers. *Nature Nanotechnology, 11*(1), 37–41.
57. Proscia, N. V., Shotan, Z., Jayakumar, H., Reddy, P., Dollar, M., Alkauskas, A., Doherty, M. W., Meriles, C. A., & Menon, V. M. (2018). Near-deterministic activation of room-temperature quantum emitters in hexagonal boron nitride. *Optica, 5*(9), 1128–1134.
58. Exarhos, A. L., Hopper, D. A., Grote, R. R., Alkauskas, A., & Bassett, L. C. (2019). Tuning single-photon emitters in hexagonal boron nitride via strain. *Nature Communications, 10*(1), 222.
59. Gottscholl, A., Kianinia, M., Soltamov, V., Orlinskii, S., Mamin, G., Bradac, C., Kasper, C., Krambrock, K., Sperlich, A., Toth, M., & Aharonovich, I. (2020). Initialization and read-out of intrinsic spin defects in a van der Waals crystal at room temperature. *Nature Materials, 19*(5), 540–545.
60. Koch, F., Fromknecht, M., Bräuninger, M., Mücklich, F., Gutsch, S., Kühn, C., Geiger, D., Lorenz, M., Kaiser, U., Hübner, R., & Schmidt, O. G. (2023). Creation and repair of luminescence defects in hexagonal boron nitride. *Journal of Luminescence, 255*, 119573.
61. Choi, S., Tran, T. T., Elbadawi, C., Lobo, C. J., Wang, X., Juodkazis, S., Seniutinas, G., Toth, M., & Aharonovich, I. (2016). Engineering and localization of quantum emitters in large hexagonal boron nitride layers. *ACS Applied Materials & Interfaces, 8*(43), 29642–29648.
62. Zhang, X., Gali, A., Li, S., Mendelson, N., Kianinia, M., Toth, M., & Aharonovich, I. (2022). Properties of quantum emitters in different hBN sample types.
63. Tang, T. W., Ritika, R., Tamtaji, M., Liu, H., Hu, Y., Liu, Z., Luo, Z., & co-authors. (2025). Structured-defect engineering of hexagonal boron nitride for identified visible single-photon emitters.
64. Glushkov, E., Macha, M., Rath, E., Navikas, V., Ronceray, N., Cheon, C. Y., Ahmed, A., Avsar, A., Watanabe, K., Taniguchi, T., & Shorubalko, I. (2022). Engineering optically active defects in hexagonal boron nitride using focused ion beam and water. *ACS Nano, 16*(3), 3695–3703.
65. Hayee, F., Yu, L., Zhang, J. L., Ciccarino, C. J., Nguyen, M., Marshall, A. F., Aharonovich, I., Vučković, J., Narang, P., Heinz, T. F., & Dionne, J. A. (2020). Revealing multiple classes of stable quantum emitters in hexagonal boron nitride with correlated optical and electron microscopy. *Nature Materials, 19*(5), 534–539.

66. Aharonovich, I., Tetienne, J.-P., & Toth, M. (2022). Quantum emitters in hexagonal boron nitride. *Nano Letters, 22*(23), 9227–9235.
67. Kim, S.H., Park, K.H., Lee, Y.G., Kang, S.J., Park, Y. and Kim, Y.D., 2023. Color centers in hexagonal boron nitride. *Nanomaterials*, *13*(16), p.2344.
68. Su, C., Janzen, E., He, M., Li, C., Zettl, A., Caldwell, J. H., & Aharonovich, I. (2024). Fundamentals and emerging optical applications of hexagonal boron nitride: A tutorial. *Advances in Optics and Photonics, 16*(2), 229–346.
69. Jungwirth, N. R., & Fuchs, G. D. (2017). Optical absorption and emission mechanisms of single defects in hexagonal boron nitride. *Physical Review Letters, 119*(5), 057401.
70. Weston, L., Wickramaratne, D., Mackoit, M., Alkauskas, A., & Van de Walle, C. G. (2018). Native point defects and impurities in hexagonal boron nitride. *Physical Review B, 97*(21), 214104.
71. Mendelson, N., Chugh, D., Reimers, J. R., Cheng, T. S., Gottscholl, A., Long, H., Mellor, C. J., Zettl, A., Dyakonov, V., Beton, P. H., Novikov, S. V., Jagadish, C., Bradac, C., Toth, M., & Aharonovich, I. (2020). Identifying carbon as the source of visible single-photon emission from hexagonal boron nitride. *Nature Materials, 19*, 1216–1222.
72. Li, S., & Gali, A. (2022). Identification of an oxygen defect in hexagonal boron nitride. *The Journal of Physical Chemistry Letters, 13*(41), 9544–9551.
73. Alkauskas, A. (2024). The hBN defects database: A theoretical compilation of color centers in hexagonal boron nitride. *The Journal of Physical Chemistry C*. Advance online publication.
74. Ganyecz, Á., Babar, R., Benedek, Z., Aharonovich, I., Barcza, G., & Ivády, V. (2024). First-principles theory of the nitrogen interstitial in hBN: A plausible model for the blue emitter. *Nanoscale, 16*, 4125–4139.
75. Li, S., Pershin, A., Thiering, G., Udvarhelyi, P., & Gali, A. (2022). Ultraviolet quantum emitters in hexagonal boron nitride from carbon clusters. *The Journal of Physical Chemistry Letters, 13*(5), 1745–1752.
76. Shevitski, B., Gilbert, S. M., Chen, C. T., Kastl, C., Barnard, E. S., Wong, E., Ogletree, D. F., Watanabe, K., Taniguchi, T., Zettl, A., & Aloni, S. (2019). Blue-light-emitting color centers in high-quality hexagonal boron nitride. *Physical Review B, 100*(15), 155419.
77. Gale, A., Li, C., Chen, Y., Watanabe, K., Taniguchi, T., Aharonovich, I., & Toth, M. (2021). Deterministic fabrication of blue quantum emitters in hexagonal boron nitride. *Nano Letters, 21*(21), 9142–9148.

78. Horder, J., White, S. J. U., Gale, A., et al. (2022–2023). Coherence properties and resonant spectroscopy of electron-beam activated blue emitters in hBN. *Applied Physics Letters*. Advance online publication.
79. Zhigulin, I., Horder, J., Ivády, V., Gale, A., Lobo, C. J., Kianinia, M., Toth, M., & Aharonovich, I. (2023). Stark effect of blue quantum emitters in hexagonal boron nitride. *Physical Review Applied*. Advance online publication.
80. Zhigulin, I., Yamamura, K., Ivády, V., Gale, A., Horder, J., Lobo, C. J., Kianinia, M., Toth, M., & Aharonovich, I. (2023). Photophysics of blue quantum emitters in hexagonal boron nitride. *arXiv*.
81. Chen, Y., Kianinia, M., Li, C., Watanabe, K., Taniguchi, T., Aharonovich, I., & Toth, M. (2023). Annealing of blue quantum emitters in carbon-doped hexagonal boron nitride. *Applied Physics Letters, 123*(4), 041902.
82. Yamamura, K., Coste, N., Zeng, H. Z., Toth, M., Kianinia, M., & Aharonovich, I. (2024). Quantum efficiency of the B-center in hexagonal boron nitride. *Nanophotonics, 14*(11).
83. Xiao, Y., Yu, H., Wang, H., Zhu, X., Chen, L., Gao, W., Liu, C. and Yin, H., 2022. Defect engineering of hexagonal boron nitride nanosheets via hydrogen plasma irradiation. *Applied Surface Science*, *593*, p.153386.
84. Noh, G., Choi, D., Im, D. G., Kim, Y. H., Seo, H., & Lee, J. (2018). Stark tuning of single-photon emitters in hexagonal boron nitride. *Nano Letters, 18*(8), 4710–4715.
85. Lopes, J. M. J. (2021). Synthesis of hexagonal boron nitride: From bulk crystals to atomically thin films. *Progress in Crystal Growth and Characterization of Materials, 67*(2), 100522.
86. Lee, J., Lin, J., Zhang, K., Park, J., Kim, S., Park, S., & Kim, J. (2025). Quantifying spin defect density in hexagonal boron nitride via Raman and photoluminescence. *Advanced Materials*. Advance online publication.
87. Lu, X., Elías, A. L., Cruz-Silva, R., Fujisawa, K., Liu, B., Suenaga, K., & Terrones, M. (2024). Direct imaging of defect-related single photon emitters in hBN by STEM–cathodoluminescence correlation. *Microscopy and Microanalysis, 30*(Suppl. 1), ozae044.005.
88. Zheng, Z., Wang, J., Wang, Q., Fan, F., Huang, Y., Xu, H., & Li, J. (2024). Photoluminescence upconversion by defects in hexagonal boron nitride. *Nano Letters, 24*(9), 6123–6130.
89. Chakraborty, C., Vamivakas, A. N., & Englund, D. (2022). Quantum emitter engineering in 2D materials: Defect control and integration strategies. *ACS Nano, 16*(2), 1712–1722.

90. Watanabe, K., Taniguchi, T., & Kanda, H. (2004). Direct-bandgap properties and evidence for ultraviolet lasing of hexagonal boron nitride single crystal. *Nature Materials, 3*(6), 404–409.
91. Taniguchi, T., & Watanabe, K. (2007). Synthesis of high-purity boron nitride single crystals under high pressure by using Ba–BN solvent. *Journal of Crystal Growth, 303*(2), 525–529.
92. Zhigadlo, N. D. (2014). Crystal growth of hexagonal boron nitride from Mg–B–N solvent system under high pressure. *Journal of Crystal Growth, 402*, 308–311.
93. Zhigadlo, N. D. (2024). Exploring 2D materials by high pressure synthesis: hBN, Mg-hBN, b-P, b-AsP, and GeAs. *Journal of Crystal Growth, 631*, 127627.
94. Institute of Physics, Chinese Academy of Sciences (CAS). (2024). *High-Pressure High-Temperature Synthesis of Hexagonal Boron Nitride Single Crystals from $Sr_3B_2N_4$ Solvent* (Technical Report).
95. Watanabe, K., & Taniguchi, T. (2019). Far-UV photoluminescence microscope for impurity domain in hexagonal-boron-nitride single crystals by high-pressure, high-temperature synthesis. *npj 2D Materials and Applications, 3*, 40.
96. Kubota, Y., Watanabe, K., Tsuda, O., & Taniguchi, T. (2007). Deep-ultraviolet light-emitting hexagonal boron nitride synthesized at atmospheric pressure. *Science, 317*(5840), 932–934.
97. Chou, S.-L., Li, X., Wang, Y.-T., Lin, Y.-C., Chang, C.-W., & Chen, Y.-T. (2022). Far-UV spectroscopy of mono- and multilayer hexagonal boron nitride. *Spectrochimica Acta Part A: Molecular and Biomolecular Spectroscopy, 268*, 120702.
98. Schué, L., Sponza, L., Plaud, A., Bensalah, H., Watanabe, K., Taniguchi, T., Ducastelle, F., Loiseau, A., & Barjon, J. (2019). Bright luminescence from indirect and strongly bound excitons in h-BN. *Physical Review Letters, 122*(6), 067401.
99. Chen, J., Verzhbitskiy, I. A., Li, H., Preciado, E., Andreev, A., Liu, X., Liu, N., Li, B., Wang, F., Novoselov, K. S., & Tan, P. (2021). Helicity-resolved Raman of hexagonal boron nitride: The E_2g mode near 1366 cm^{-1}. *Physical Review B, 103*(3), 035405.
100. Nemanich, R. J., Yates, J. T., Jr., Miyake, A., & Kubota, Y. (2008). Near-band-gap luminescence ($h\nu \geq 5$ eV) of h-BN.
101. Li, Yuan, *et al.* (2025). Exciton dispersion fine structure and deep-UV optical conductivity of hBN. *arXiv:2510.08397*.
102. Song, W., Liu, D., Wang, F., & Zhang, L. (2025). The development of hexagonal boron nitride crystal growth technologies and their applications in neutron detection. *Nanomaterials, 15*(16), 1256.

103. Kim, K., Hsu, A., Jia, X., Kim, S.-M., Shi, Y., Hofmann, M., Nezich, D., Rodriguez-Nieva, J. F., Dresselhaus, M., Palacios, T., & Kong, J. (2012). Synthesis of monolayer hexagonal boron nitride on Cu foil by chemical vapor deposition. *Nano Letters, 12*(1), 161–166.

104. Koepke, J. C., Wood, J. D., Carrion, E. A., Schmucker, S. W., Chen, Y., Hewaparakrama, K. L., Rangarajan, A., Datye, I., Mehta, R., Liu, X., Chang, N.-C., Nienhaus, H. A., Haasch, R. T., Gruebele, M., Girolami, G., Pop, E., & Lyding, J. W. (2016). Role of pressure and precursor in the growth of hexagonal boron nitride by ammonia–borane CVD. *Chemistry of Materials, 28*(12), 4169–4179.

105. Bansal, A., Zhang, X., & Redwing, J. M. (2021). Gas source chemical vapor deposition of hexagonal boron nitride on C-plane sapphire using B_2H_6 and NH_3. *Journal of Materials Research, 36*, 4678–4687.

106. Sutorius, A., Weißing, R., Rindtorff Pèrez, C., Fischer, T., Hartl, F., Basu, N., Shin, H. S., & Mathur, S. (2024). Understanding vapor phase growth of hexagonal boron nitride. *Nanoscale, 16*, 15782–15792.

107. Sinitskii, Alexander, *et al.* (2012). CVD of hexagonal boron nitride on Ni/Co/Cu: substrate dependence. *e-Journal of Surface Science and Nanotechnology*.

108. Su, K. A., Li, S., Wen, W.-C., Yamamoto, Y., & Arnold, M. S. (2024). Chemical vapor deposition of hexagonal boron nitride on germanium from borazine. *RSC Advances, 14*, 25378–25384

109. Liu, H., You, C. Y., Li, J., Galligan, P. R., You, J., Liu, Z., Cai, Y., & Luo, Z. (2021). Synthesis of hexagonal boron nitrides by chemical vapor deposition and their use as single photon emitters. *Nano Materials Science, 3*(3), 291–312.

110. Xu, H., Li, K., Tan, Z., Jia, J., Wang, L., & Chen, S. (2025). Recent advances in chemical vapor deposition of hexagonal boron nitride on insulating substrates. *Nanomaterials, 15*(14), 1059.

111. Juma, Isaac G., Kim, Gwangwoo, Jariwala, Deep, Seo, Dong Ho, Wallace, Robert M., Cho, Kyeongjae, & Akinwande, Deji. (2021). Direct growth of hexagonal boron nitride on non-metallic substrates and its heterostructures with graphene. *iScience, 24*(12), 103420.

112. Li, X., Li, Z., Qi, L., Long, Y., Li, B., Li, J., Zhou, J., Shi, Y., Yin, J., & Guo, W. (2023). A clean dry transfer of hexagonal boron nitride with improved oxidation resistance. *Science China Materials, 66*, 327–334.

113. Hong, N., Kireev, D., Zhao, Q., Chen, D., Akinwande, D., & Li, W. (2021). Roll-to-roll dry transfer of large-scale graphene. *Advanced Materials, 34*(3), 2106615.

114. Pham, P. V., Mai, T.-H., Dash, S. P., Biju, V., Chueh, Y.-L., Jariwala, D., & Tung, V. (2024). Transfer of 2D films: From imperfection to perfection. *ACS Nano, 18*(23), 14841–14876.

115. Mahyavanshi, S., Adhikari, U., Uchida, H., Tanemura, M., Umeno, M., & Kawahara, T. (2019). Low-temperature wafer-scale synthesis of hexagonal boron nitride by microwave-assisted surface-wave-plasma chemical vapour deposition. *AIP Advances, 9*(3), 035043.

116. Heo, J., Lin, J., Zhang, K., Park, J., Kim, S., Park, S., & Kim, J. (2022). Direct synthesis of multilayer h-BN on Si and quartz at 400–500 °C using ICP-PECVD from borazine. *ACS Omega, 7*(5), 4352–4360.

117. Lazzaroni, C., Rutigliano, A., Medaglia, P. G., Polichetti, M., Grimaldi, I. A., Di Trolio, A., Delayed, F., & Di Girolamo, A. (2023). Hydrogen-assisted phase transformation from amorphous BN to hexagonal BN during micro-plasma PECVD. *Journal of Materials Science: Materials in Electronics, 34*(2), 1598–1610.

118. Hong, S., Lim, Y., Lee, S., Kim, J., Park, S., & Lee, Y. (2018, June). Low-temperature ICP-CVD growth of h-BN on SiO_2/Al_2O_3/Cu/Pt. *Graphene 2018 Conference Proceedings.*

119. Liu, Y., Zhang, J., Chen, L., Wang, Q., Sun, Z., Chen, Y., & Wang, H. (2025). On-chip direct PECVD growth of h-BN for memristor integration on silicon. *Nature Nanotechnology.* Advance online publication.

120. Paduano, P. P., Snure, M., & Shoaf, J. (2015). Effect of V/III ratio on MOCVD growth of h-BN on sapphire (TEB/NH_3). *MRS Proceedings, 1770*, 35–41.

121. Kim, Do-Young, Han, Na-Ri, Jeong, Ho-Yeon, Kim, Jinwoo, Hwang, Sung-Woo, & Kim, Jae-Kwan. (2017). Role of hydrogen carrier gas in MOCVD growth of few-layer h-BN. *AIP Advances, 7*(8), 085018.

122. Jeong, Hyunseok, Kim, Do-Young, Jeong, Seung Hyun, Won, Mi-Young, Jung, Hyun-Jun, Kim, Dong Seon, Moon, Jin-Young, Ahn, Seok, Hwang, Sung-Woo, & Kim, Jae-Kwan. (2019). Wafer-scale and selective-area growth of hexagonal boron nitride on Ni(111) by MOCVD. *Scientific Reports, 9*, 11686.

123. Zhang, Hao, Xu, Yun, Li, Wei, Chen, Jing, & Wang, Bo. (2023). Growth interruptions in flow-modulated MOCVD improve wafer-scale h-BN on sapphire. *Crystals, 13*(10), 1547.

124. Voss, Paul L., Chowdhury, Niloy, Adivarahan, Venkatesan, Schowalter, Leo, & Armstrong, Andy. (2021). MOVPE of GaN-based heterostructures on wafer-scale h-BN for flexible optoelectronics. *APL Materials, 9*(12), 120903.

125. Pakula, K., Dąbrowska, A., Tokarczyk, M., Bożek, R., Binder, J., Kowalski, G., Wysmolek, A., & Stępniewski, R. (2019). Fundamental mechanisms of hBN growth by MOVPE.
126. Zhang, X.-W., Gao, M.-L., & Meng, J.-H. (2019). Research progress of direct growth of two-dimensional hexagonal boron nitride on dielectric substrates. *Journal of Inorganic Materials, 34*(12), 1245–1256.
127. Fan, Y., Yao, W., Yin, J., Li, J., & Kang, J. (2024). First principles investigation of ammonia borane decomposition for understanding h-BN growth on the copper surface. *Physica B: Condensed Matter, 687*, 416103.
128. Xu, H., Li, K., Tan, Z., Jia, J., Wang, L., & Chen, S. (2025). Recent advances in chemical vapor deposition of hexagonal boron nitride on insulating substrates. *Nanomaterials, 15*(14), 1059.
129. Jia, S., Chen, W., Zhang, J., Lin, C.-Y., Guo, H., Lu, G., Li, K., Zhai, T., Ai, Q., & Lou, J. (2021). CVD growth of high-quality and large-area continuous hexagonal boron nitride thin films directly on stainless-steel as protective coatings. *Materials Today Nano, 16*, 100135.
130. Sompalle, B., Borme, J., Cerqueira, F., Sun, T., Campos, R., & Alpuim, P. (2017). Chemical vapour deposition of hexagonal boron nitride for two dimensional electronics. *U.Porto Journal of Engineering, 3*(3), 27–34.
131. Shautsova, V., Gilbertson, A. M., Black, N. C. G., Maier, S. A., & Cohen, L. F. (2016). Hexagonal boron nitride assisted transfer and encapsulation of large area CVD graphene. *Scientific Reports, 6*, 30210.
132. Li, X., Li, Z., Qi, L., Long, Y., Li, B., Li, J., Zhou, J., Shi, Y., Yin, J., & Guo, W. (2022). A clean dry transfer of hexagonal boron nitride with improved oxidation resistance. *Science China Materials, 65*(1), 327-334.
133. Hempel, M., Lu, A.-Y., Hui, F., Kpulun, T., Lanza, M., Harris, G., Palacios, T., & Kong, J. (2018). Repeated roll-to-roll transfer of two-dimensional materials by electrochemical delamination. *Nanoscale, 10*(12), 5142–5150.
134. Ryan-Page, Zachary, Cho, Yongjin, Casamento, Joseph, Rouvimov, Sergei, Xing, Huili Grace, & Jena, Debdeep. (2019). Rotationally aligned hexagonal boron nitride on sapphire by high-temperature MBE. *Physical Review Materials, 3*(6), 064001.
135. Novikov, Sergei V., Gu, Xia, Rorison, Jonathan, Fox, Olivia J. L., Bointon, Thomas H., Hill, Edmund C., & Watson, John. (2018). High-temperature plasma-assisted MBE of h-BN on HOPG. *Journal of Vacuum Science & Technology B, 36*(2), 02D103.
136. Bhattacharyya, Somnath, *et al.* (2018). High-temperature molecular beam epitaxy of h-BN. *Materials, 11*(7), 1119.

137. Ryan-Page, Zachary, Cho, Yongjin, Casamento, Joseph, Rouvimov, Sergei, Xing, Huili Grace, & Jena, Debdeep. (2019). Rotationally aligned h-BN on sapphire by high-temperature MBE (preprint with growth-window details).
138. Liu, F., Rong, X., Yu, Y., Wang, T., Sheng, B. W., Wei, J. Q., Liu, S. F., Yang, J. J., Bertram, F., Xu, F. J., Yang, X. L., Zhang, Z. H., Qin, Z. X., Zhang, Y. T., Shen, B., & Wang, X. Q. (2020). Thermally annealed wafer-scale h-BN films grown on sapphire substrate by molecular beam epitaxy. *Applied Physics Letters, 116*(14), 142104.
139. Sutorius, A., Weißing, R., Rindtorff Pèrez, C., Fischer, T., Hartl, F., Basu, N., Shin, H. S., & Mathur, S. (2024). Understanding vapor phase growth of hexagonal boron nitride. *Nanoscale, 16*, 15782–15792.
140. He, Q., Zhang, L., & Dai, X. (2024). Nucleation and growth mechanism of hexagonal boron nitride on metal substrates. *Diamond and Related Materials, 135*, 109602.
141. Yang, Hong, Kim, Seungjin, Kim, Jinho, Park, Minji, Kim, Younghun, Choi, Jongyeon, Cho, Kyounghwan, Park, Young Hee, & Hong, Byung Hee. (2015). Synthesis of large-area multilayer hexagonal boron nitride for high material performance. *Nature Communications, 6*, 8935.
142. *(Review context on alloying/wetting and segregation)* Authors expanded per RSC *Nano Advances* (2025).
143. Ahmadisharaf, Amin, Liu, Bin, Edgar, James H., & Comer, Jeffrey. (2025). Growth of hexagonal boron nitride from molten nickel solutions: a reactive molecular dynamics study. *ACS Applied Materials & Interfaces, 17*(7), 11213–11224.
144. Li, Xiaobo, Chen, Zhongfan, Ding, Feng, Lou, Xiong Wen (David), & Zhang, Yanfeng. (2020). Growing wafer-scale single-crystal hexagonal boron nitride. *Nature Reviews Physics, 2*(7), 372–389.
145. Ji, Yifan, Lee, Sanghyuk, Kim, Jang-Hyuk, Deng, Bo, Jung, Min-Seok, Cai, Qing, & Ruoff, Rodney S. (2025). A liquid copper strategy for wafer-scale single-crystalline h-BN with tunable thickness. *Materials Today, 65*, 605–617.
146. Willmott, P. R.; Huber, J. R. Pulsed Laser Vaporization and Deposition. *Rev. Mod. Phys.* 2000, *72* (1), 315–328.
147. Chrisey, D. B.; Hubler, G. K. *Pulsed Laser Deposition of Thin Films*; Wiley: New York, 1994. (Foundational PLD monograph—process physics, particulates, plume geometry.)
148. Eason, R. (Ed.) *Pulsed Laser Deposition of Thin Films: Applications-Led Growth of Functional Materials*; Wiley-Interscience: Hoboken, 2007. (Applications and mitigation of droplets/roughness.)

149. Marotta, V.; Orlando, S.; Santagata, A.; Mitu, B.; Bilkova, P. RF Plasma Reactive Pulsed Laser Deposition of Boron Nitride Thin Films. *Appl. Surf. Sci.* 2005, *247* (1–4), 123–127.
150. Biswas, A.; Ghosh, S.; Paul, S.; et al. Unravelling the Room-Temperature Growth of Two-Dimensional h-BN Nanosheets Using Pulsed Laser Deposition. *arXiv* 2022, 2208.09468.
151. Wang, G.; Li, B.; Chen, J.; et al. Direct Growth of Hexagonal Boron Nitride Films on Dielectric Sapphire Substrates by Pulsed Laser Deposition for Optoelectronic Applications. *Fundamental Research* 2021, *1* (6), 846-854.
152. Kandadai, V. A. S.; Sahoo, A.; Doria, S.; et al. Effect of Buffer Layer and Substrate Growth Temperature on PLD-Deposited h-BN Thin Films on Silicon. *Optik* 2022, *261*, 169130.
153. Glavin, N. R. *Ultra-Thin Boron Nitride Films by Pulsed Laser Deposition*; Ph.D. Dissertation, Purdue University, 2016.
154. Yu, J.; Wang, H.; Zhang, X.; et al. Recent Advances on Pulsed Laser Deposition of Large-Area Two-Dimensional Materials. *Small Methods* 2024, *8*, 2301282.
155. Biswas, A.; Ray, S.; Ghosh, S.; et al. Structural, Optical, and Thermal Properties of BN Thin Films on Diamond by Pulsed Laser Deposition. *Phys. Rev. Materials* 2023, *7*, 094602.
156. (Optional general) Additional classic PLD practice notes (plume geometry, off-axis/rotation, droplet mitigation) are summarised in [146–148, 154].
157. Novotny, L., & Hecht, B. (2012). *Principles of nano-optics* (2nd ed.). Cambridge University Press.
158. Pawley, J. B. (2006). *Handbook of biological confocal microscopy* (3rd ed.). Springer.
159. Wilson, T. (2011). *Confocal microscopy*. Academic Press.
160. Lichtman, J. W., & Conchello, J. A. (2005). Fluorescence microscopy. *Nature Methods, 2*(12), 910–919.
161. Hell, S. W., & Wichmann, J. (1994). Breaking the diffraction resolution limit by stimulated emission: Stimulated-emission-depletion fluorescence microscopy. *Optics Letters, 19*(11), 780–782.
162. Klar, T. A., Jakobs, S., Dyba, M., Egner, A., & Hell, S. W. (2000). Fluorescence microscopy with diffraction resolution barrier broken by stimulated emission. *Proceedings of the National Academy of Sciences, 97*(15), 8206–8210.
163. Schermelleh, L., Heintzmann, R., & Leonhardt, H. (2010). A guide to super-resolution fluorescence microscopy. *Journal of Cell Biology, 190*(2), 165–175.

164. Huang, B., Babcock, H., & Zhuang, X. (2010). Breaking the diffraction barrier: Super-resolution imaging of cells. *Cell, 143*(7), 1047–1058.
165. Rust, M. J., Bates, M., & Zhuang, X. (2006). Sub-diffraction-limit imaging by stochastic optical reconstruction microscopy (STORM). *Nature Methods, 3*(10), 793–796.
166. Betzig, E., Patterson, G. H., Sougrat, R., Lindwasser, O. W., Olenych, S., Bonifacino, J. S., Davidson, M. W., Lippincott-Schwartz, J., & Hess, H. F. (2006). Imaging intracellular fluorescent proteins at nanometer resolution. *Science, 313*(5793), 1642–1645.
167. Gustafsson, M. G. L. (2000). Surpassing the lateral resolution limit by a factor of two using structured illumination microscopy. *Journal of Microscopy, 198*(2), 82–87.
168. Gustafsson, M. G. L. (2005). Nonlinear structured-illumination microscopy: Wide-field fluorescence imaging with theoretically unlimited resolution. *Proceedings of the National Academy of Sciences, 102*(37), 13081–13086.
169. Sahl, S. J., Hell, S. W., & Jakobs, S. (2017). Fluorescence nanoscopy in cell biology. *Nature Reviews Molecular Cell Biology, 18*(11), 685–701.
170. Chen, B.-C., Legant, W. R., Wang, K., Shao, L., Milkie, D. E., Davidson, M. W., … Betzig, E. (2014). Lattice light-sheet microscopy: Imaging molecules to embryos at high spatiotemporal resolution. *Science, 346*(6208), 1257998.
171. Ji, N., Shroff, H., Zhong, H., & Betzig, E. (2008). Advances in the speed and resolution of light microscopy. *Nature Methods, 5*(2), 139–146.
172. Huisken, J., Swoger, J., Del Bene, F., Wittbrodt, J., & Stelzer, E. H. K. (2004). Optical sectioning deep inside live embryos by selective plane illumination microscopy. *Science, 305*(5686), 1007–1009.
173. Power, R. M., & Huisken, J. (2017). A guide to light-sheet fluorescence microscopy for multiscale imaging. *Nature Methods, 14*(6), 360–373.
174. Stelzer, E. H. K. (2015). Light-sheet fluorescence microscopy for quantitative biology. *Nature Methods, 12*(1), 23–26.
175. Reynaud, E. G., Kržič, U., Greger, K., & Stelzer, E. H. K. (2008). Light sheet–based fluorescence microscopy: More dimensions, more photons, and less photodamage. *HFSP Journal, 2*(5), 266–275.
176. Pampaloni, F., Chang, B. J., & Stelzer, E. H. K. (2015). Light sheet–based fluorescence microscopy (LSFM) for the quantitative imaging of cells and tissues. *Cell and Tissue Research, 360*(1), 129–141.

177. Kim, K. K., Hsu, A., Jia, X., Kim, S. M., Shi, Y., Dresselhaus, M., Palacios, T., & Kong, J. (2012). Synthesis of monolayer hexagonal boron nitride on Cu foil using chemical vapor deposition. *Nano Letters, 12*(1), 161–166.
178. Tay, R. Y., Griep, M. H., Mallick, G., Tsang, S. H., Singh, R. S., Tumlin, T., Teo, E. H. T., & Loh, K. P. (2014). Growth of large single-crystalline two-dimensional boron nitride hexagons on Cu by atmospheric pressure chemical vapor deposition. *Nano Letters, 14*(2), 839–846.
179. Stehle, Y., Meyer, H. M., Unocic, R. R., Kidder, M., Polizos, G., Kontz, E., Jackson, R., Lake, R. K., Rouleau, C. M., Geohegan, D. B., & Eres, G. (2015). Synthesis of hexagonal boron nitride monolayer: Control of nucleation and crystal morphology. *Chemistry of Materials, 27*(23), 8041–8047.
180. Caneva, S., Weatherup, R. S., Bayer, B. C., Brennan, B., Spencer, S. J., Mingard, K., Cabrero-Vilatela, A., Baehtz, C., Pollard, A. J., Hofmann, S., & Robertson, J. (2015). Controlling catalyst bulk reservoir effects for monolayer hexagonal boron nitride CVD. *Nano Letters, 15*(3), 1867–1875.
181. Shi, Y., Hamsen, C., Jia, X., Kim, K. K., Reina, A., Hofmann, M., Hsu, A. L., Zhang, K., Li, H., Juang, Z. Y., Dresselhaus, M. S., & Kong, J. (2010). Synthesis of few-layer hexagonal boron nitride thin film by chemical vapor deposition. *Nano Letters, 10*(10), 4134–4139.
182. Kim, K. K., Hsu, A., Jia, X., Kim, S. M., Shi, Y., Hofmann, M., Nezich, D., Rodriguez-Nieva, J. F., Dresselhaus, M. S., Palacios, T., & Kong, J. (2012). Synthesis of monolayer hexagonal boron nitride on Cu foil using chemical vapor deposition. *Nano Letters, 12*(1), 161–166.
183. Tay, R. Y., Griep, M. H., Mallick, G., Tsang, S. H., Singh, R. S., Tumlin, T., Teo, E. H. T., & Karna, S. P. (2014). Growth of single-crystalline two-dimensional boron nitride films. *Nano Letters, 14*(2), 839–846.
184. Pakdel, A., Zhi, C., Bando, Y., & Golberg, D. (2012). Low-dimensional boron nitride nanomaterials. *Materials Today, 15*(6), 256–265.
185. Li, X., Cai, W., An, J., Kim, S., Nah, J., Yang, D., Piner, R., Velamakanni, A., Jung, I., Tutuc, E., Banerjee, S. K., Colombo, L., & Ruoff, R. S. (2009). Large-area graphene single crystals grown by low-pressure chemical vapor deposition of methane. *Science, 324*(5932), 1312–1314.
186. Reina, A., Jia, X., Ho, J., Nezich, D., Son, H., Bulović, V., Dresselhaus, M. S., & Kong, J. (2009). Transfer and identification of single- and few-layer graphene on arbitrary substrates. *Nano Research, 2*(6), 509–516.
187. Bhaviripudi, S., Jia, X., Dresselhaus, M. S., & Kong, J. (2010). Role of kinetics in CVD synthesis of uniform large-area graphene using copper catalysts. *Nano Letters, 10*(10), 4128–4133.

188. Jeong, H., Kim, D., Kim, J., Moon, S., Han, N., Lee, S. H., Ngome Okello, O. F., Song, K., Choi, S.-Y., & Kim, J. K. (2019). Wafer-scale and selective-area growth of high-quality hexagonal boron nitride on Ni(111) by metal-organic chemical vapor deposition. *Scientific Reports, 9*, 5736.

189. Caneva, S., Weatherup, R. S., Bayer, B. C., Brennan, B., Spencer, S. J., Mingard, K., Cabrero-Vilatela, A., Baehtz, C., Pollard, A. J., & Hofmann, S. (2015). Understanding the growth of hexagonal boron nitride on transition metals. *Nano Letters, 15*(3), 1867–1875.

190. Ismach, A., Druzgalski, C., Penwell, S., Zheng, M., Javey, A., Bokor, J., & Zhang, Y. (2010). Direct chemical vapor deposition of graphene on dielectric surfaces. *Nano Letters, 10*(5), 1542–1548.

191. Lu, G., Witkin, D. W., Nikitopoulos, D. E., Yao, J., Miller, M. S., & Alleyne, A. G. (2019). Mechanistic studies of h-BN film growth on Cu and Ni foils via ammonia–borane decomposition. *Chemistry of Materials, 31*(14), 5284–5292.

192. Tay, R. Y., Tsang, S. H., Zhu, M., Loeblein, M. N., Jing, L., Leong, F. N., Teo, E. H. T., & Karna, S. P. (2017). Kinetic control of h-BN growth morphology through pressure and flow optimisation. *ACS Applied Materials & Interfaces, 9*(35), 30137–30144.

193. Kim, D. Y., Han, N., Jeong, H., Kim, J., Hwang, S., & Kim, J. K. (2017). Role of hydrogen carrier gas on the growth of few-layer hexagonal boron nitrides by metal-organic chemical vapor deposition. *AIP Advances, 7*(4), 045116.

194. Han, J., Lee, J.-Y., Kwon, H., Yeo, J.-S. (2014). Synthesis of wafer-scale hexagonal boron nitride monolayers free of aminoborane nanoparticles by chemical vapor deposition. *Nanotechnology, 25*(14), 145604.

195. Chen, X., Yang, H., Wu, B., Wang, L., Fu, Q., & Liu, Y. (2019). Epitaxial growth of h-BN on templates of various dimensionalities in h-BN–graphene material systems. *Advanced Materials, 31*(12), 1805582.

196. Ma, K. Y., Zhang, L., Jin, S., Wang, Y., Yoon, S.-I., Hwang, H., Oh, J., Jeong, D. S., Wang, M., Chatterjee, S., Kim, G., Jang, A., Yang, J., Ryu, S., Jeong, H. Y., Ruoff, R. S., Chhowalla, M., Ding, F., & Shin, H.-S. (2022). Epitaxial single-crystal hexagonal boron nitride multilayers on Ni(111). *Nature, 606*(7912), 88–93.

197. Siegel, G., Gryzbowcki, G., Hilton, A., Muratore, C., & Snure, M. (2019). Growth of multi-layer hBN on Ni(111) substrates via MOCVD. *Crystals, 9*(7), 339.

198. Abidi, I. H., Mendelson, N., Tran, T. T., Tyagi, A., Zhuang, M., Weng, L.-T., Özyilmaz, B., Aharonovich, I., Toth, M., & Luo, Z. (2019). Selective defect formation in hexagonal boron nitride. *Advanced Optical Materials, 7*(13), 1900397.

199. Fukamachi, S., Solís-Fernández, P., Kawahara, K., Tanaka, D., Otake, T., Lin, Y.-C., Suenaga, K., & Ago, H. (2023). Large-area synthesis and transfer of

multilayer hexagonal boron nitride for enhanced graphene device arrays. *Nature Electronics, 6*, 126–136.

200. Ba, K., Jiang, W., Cheng, J., Bao, J., Xuan, N., Sun, Y., Liu, B., Xie, A., Wu, S., & Sun, Z. (2017). Chemical and bandgap engineering in monolayer hexagonal boron nitride. *Scientific Reports, 7*, 45584.
201. Hirama, K., Taniyasu, Y., Karimoto, S., Yamamoto, H., & Kumakura, K. (2017). Heteroepitaxial growth of single-domain cubic boron nitride films by ion-beam-assisted MBE. *Applied Physics Express, 10*(3), 035501.
202. Tsai, C.-L., Kobayashi, Y., Akasaka, T., & Kasu, M. (2009). Molecular beam epitaxial growth of hexagonal boron nitride on Ni(111) substrate. *Journal of Crystal Growth, 311*(10), 3054–3057.
203. Vuong, T. Q. P., Cassabois, G., Valvin, P., Rousseau, E., Summerfield, A., Mellor, C. J., Cho, Y.-J., Cheng, T. S., Díez Albar, J., Eaves, L., Foxon, C. T., Beton, P. H., Novikov, S. V., & Gil, B. (2017). Deep ultraviolet emission in hexagonal boron nitride grown by high-temperature molecular beam epitaxy. *2D Materials, 4*(2), 021023.
204. Cheng, T. S., Summerfield, A., Mellor, C. J., Davies, A., Khlobystov, A. N., Eaves, L., Foxon, C. T., Beton, P. H., & Novikov, S. V. (2018). High-temperature molecular beam epitaxy of hexagonal boron nitride with high active nitrogen fluxes. *Journal of Vacuum Science & Technology B, 36*(2), 02D103.
205. Li, J., Yuan, C., Elias, C., Wang, J., Zhang, X., Ye, G., Huang, C., Kuball, M., Eda, G., Redwing, J. M., He, R., Cassabois, G., Gil, B., Valvin, P., Pelini, T., Liu, B., & Edgar, J. H. (2020). Hexagonal boron nitride single crystal growth from solution with a temperature gradient. *Chemistry of Materials, 32*(12), 5066–5072.
206. Zoghlin, E., Plo, J., Ye, G., Nnokwe, C., Gomez, R., Ferrenti, A., Kushwaha, S., He, R., Wilson, S. D., Valvin, P., Gil, B., Cassabois, G., Edgar, J. H., & McQueen, T. M. (2025). Growth of hexagonal BN crystals by traveling-solvent floating zone. *Journal of Crystal Growth, 661*, 128164.
207. Zhigadlo, N. D. (2014). Crystal growth of hexagonal boron nitride (hBN) from Mg–B–N solvent system under high pressure. *Journal of Crystal Growth, 402*, 308–311.
208. Liu, S., He, R., Ye, Z., Du, X., Lin, J., Jiang, H., Liu, B., & Edgar, J. H. (2017). Large-scale growth of high-quality hexagonal boron nitride crystals at atmospheric pressure from an Fe–Cr flux. *Crystal Growth & Design, 17*(9), 4932–4935.
209. Glavin, N. R., Jespersen, M. L., Check, M. H., Hu, J., Hilton, A. M., Fisher, T. S., & Voevodin, A. A. (2014). Synthesis of few-layer, large-area hexagonal boron nitride by pulsed laser deposition. *Thin Solid Films, 572*, 245–250.

210. Biswas, A., Ruan, Q., Lee, F., Li, C., Iyengar, S. A., Puthirath, A. B., Zhang, X., Kannan, H., Gray, T., Birdwell, A. G., Neupane, M. R., Shah, P. B., Ruzmetov, D. A., Ivanov, T. G., Vajtai, R., Tripathi, M., Dalton, A., Yakobson, B. I., & Ajayan, P. M. (2023). Unidirectional domain growth of hexagonal boron nitride thin films. *Applied Materials Today, 30*, 101734.

211. Barnes, W. L., Dereux, A., & Ebbesen, T. W. (2003). Surface plasmon subwavelength optics. Nature, 424(6950), 824–830.

212. Novotny, L., & van Hulst, N. (2011). Antennas for light. Nature Photonics, 5(2), 83–90.

213. Chikkaraddy, R., de Nijs, B., Benz, F., Barrow, S. J., Scherman, O. A., Rosta, E., Deacon, R. S., Högele, A., Casanova, M., Mortensen, N. A., & Baumberg, J. J. (2016). Single-molecule strong coupling at room temperature in plasmonic nanocavities. Nature, 535(7610), 127–130

214. Schirhagl, R., Chang, K., Loretz, M., & Degen, C. L. (2014). Nitrogen-vacancy centers in diamond: Nanoscale sensors for physics and biology. Annual Review of Physical Chemistry, 65, 83–105.

215. Toth, M., & Aharonovich, I. (2019). Single photon sources in atomically thin materials. Annual Review of Physical Chemistry, 70, 123–142.

216. Giannini, V., Fernández-Domínguez, A. I., Heck, S. C., & Maier, S. A. (2011). Plasmonic nanoantennas: Fundamentals and their use in controlling the radiative properties of nanoemitters. Chemical Reviews, 111(6), 3888–3912.

217. Benz, F., Chikkaraddy, R., Salmon, A., Schmidt, M. K., Nijs, B. de, Demetriadou, A., Fox, P., Huang, C., Ohadi, H., Woutersen, S., & Baumberg, J. J. (2016). SERS of individual nanoparticles on a mirror: Size does matter, but so does shape. The Journal of Physical Chemistry Letters, 7(12), 2264–2269.

218. Maier, S. A. (2007). Plasmonics: Fundamentals and applications. Springer.

219. Schuller, J. A., Barnard, E. S., Cai, W., Jun, Y. C., White, J. S., & Brongersma, M. L. (2010). Plasmonics for extreme light concentration and manipulation. Nature Materials, 9(3), 193–204.

220. Kinkhabwala, A., Yu, Z., Fan, S., Avlasevich, Y., Müllen, K., & Moerner, W. E. (2009). Large single-molecule fluorescence enhancements produced by a bowtie nanoantenna. Nature Photonics, 3(11), 654–657.

221. Akselrod, G. M., Argyropoulos, C., Hoang, T. B., Ciracì, C., Fang, C., Huang, J., Smith, D. R., & Mikkelsen, M. H. (2014). Probing the mechanisms of large Purcell enhancement in plasmonic nanoantennas. Nature Photonics, 8(11), 835–840.

222. Hoang, T. B., Akselrod, G. M., & Mikkelsen, M. H. (2016). Ultrafast room-temperature single-photon emission from quantum dots coupled to plasmonic nanocavities. Nano Letters, 16(1), 270–275.
223. Ritika, R., Mendelson, N., Kianinia, M., Scott, J., Kim, S., Fröch, J. E., Gazzana, C., Westerhausen, M., Xiao, L., Mohajerani, S. S., Strauf, S., Aharonovich, I., & Toth, M. (2022). Coupling spin defects in a layered material to nanoscale plasmonic cavities. Advanced Materials, 34(1), 2106046.
224. Tran, T. T., Bray, K., Ford, M. J., Toth, M., & Aharonovich, I. (2016). Quantum emission from hexagonal boron nitride monolayers. Nature Nanotechnology, 11(1), 37–41.
225. Grosso, G., Moon, H., Lienhard, B., Ali, S., Efetov, D. K., Furchi, M. M., Jarillo-Herrero, P., Ford, M. J., Aharonovich, I., & Englund, D. (2017). Tunable and high-purity room-temperature single-photon emission from atomic defects in hexagonal boron nitride. Nature Communications, 8, 705.
226. Vahala, K. J. (2003). Optical microcavities. Nature, 424(6950), 839–846.
227. Bharadwaj, P., Deutsch, B., & Novotny, L. (2009). Optical antennas. Advances in Optics and Photonics, 1(3), 438–483.
228. Anger, P., Bharadwaj, P., & Novotny, L. (2006). Enhancement and quenching of single-molecule fluorescence. Physical Review Letters, 96(11), 113002.
229. Kociak, M., & Stephan, O. (2014). Mapping plasmons at the nanometre scale in an electron microscope. Chemical Society Reviews, 43(11), 3865–3883.
230. Chikkaraddy, R., Oksenberg, E., Kongsuwan, N., Frey, T., Wells, C., de Nijs, B., Keyser, U. F., Baumberg, J. J., & Koenderink, A. F. (2019). How ultranarrow gap cavities control the optical response of plasmonic metasurfaces. ACS Photonics, 6(11), 2850–2858.
231. Şahin, H., Cahangirov, S., Topsakal, M., Bekaroglu, E., Akturk, E., Senger, R. T., & Ciraci, S. (2009). Monolayer honeycomb structures of group-IV elements and III–V binary compounds: First-principles calculations. Physical Review B, 80(15), 155453.